INFORMATION TO USERS

This dissertation was produced from a microfilm copy of the original document. While the most advanced technological means to photograph and reproduce this document have been used, the quality is heavily dependent upon the quality of the original submitted.

The following explanation of techniques is provided to help you understand markings or patterns which may appear on this reproduction.

1. The sign or "target" for pages apparently lacking from the document photographed is "Missing Page(s)". If it was possible to obtain the missing page(s) or section, they are spliced into the film along with adjacent pages. This may have necessitated cutting thru an image and duplicating adjacent pages to insure you complete continuity.

2. When an image on the film is obliterated with a large round black mark, it is an indication that the photographer suspected that the copy may have moved during exposure and thus cause a blurred image. You will find a good image of the page in the adjacent frame.

3. When a map, drawing or chart, etc., was part of the material being photographed the photographer followed a definite method in "sectioning" the material. It is customary to begin photoing at the upper left hand corner of a large sheet and to continue photoing from left to right in equal sections with a small overlap. If necessary, sectioning is continued again — beginning below the first row and continuing on until complete.

4. The majority of users indicate that the textual content is of greatest value, however, a somewhat higher quality reproduction could be made from "photographs" if essential to the understanding of the dissertation. Silver prints of "photographs" may be ordered at additional charge by writing the Order Department, giving the catalog number, title, author and specific pages you wish reproduced.

University Microfilms

300 North Zeeb Road
Ann Arbor, Michigan 48106

A Xerox Education Company

RICE UNIVERSITY

THE INFLUENCE OF DISSOLVED HYDROGEN ON THE SUPERCONDUCTING PROPERTIES OF MOLYBDENUM

by

BRAHM DEV BHARDWAJ

A THESIS SUBMITTED IN
PARTIAL FULFILLMENT OF THE
REQUIREMENTS FOR THE DEGREE OF
DOCTOR OF PHILOSOPHY

Thesis Director's Signature:

H. E. Rorschach.

Houston, Texas

April, 1972

To my Parents

TABLE OF CONTENTS

I. INTRODUCTION

The study of hydrogen-metal systems has recently attracted the attention of scientists and engineers interested in the understanding of the nature of metalic bonding and the failure of materials attributed to the damaging effects of hydrogen. The detrimental role played by hydrogen in metals was first recognised in the metal-fabricating industries.[1] Hydrogen reacts with metals in three ways[2] forming covalent hydrides (B_2H_6 etc.), salt-like hydrides ($[Na^+][H^-]$ etc.) and alloys ($Pd\ H_{0.55}$ etc.). The alloys are of two kinds[3], exothermic and endothermic. Exothermic alloys are accompanied by hydride formation and marked lattice changes, probably due to intractions among dissolved hydrogen atoms as in palladium[3]. The hydrogen-molybdenum system is endothermic[3], so that the solubility increases with temperature. The hydrogen is dissolved interstitially as atoms or protons[4] with a negligible or very small effect on lattice parameters. The experiments of McQuillan[5] show that there is some relationship between the ability of metals at the begining of each transition period to absorb hydrogen and the electron/atom ratio e/a. Experiments of Dempsey[6], which showed the high melting point and physical strength of metals with e/a = 5.6, suggest an inherent stability for systems with this electron-atom ratio. Burch[7] has pointed out that for early transition metals the solubility of hydrogen is controlled by the strong stabilising effect of the filled sub-band, so that factors such as expansion of the lattice may not be so important. However even this is not certain.

Baldwin[8] found that molybdenum becomes brittle when hydrogen is added and exhibits ductility curves as a function of strain rate and temperature similar to other body centered

cubic metals containing hydrogen. This led him to speculate that the same mechanism might be responsible for hydrogen embrittlement of all body centered cubic metals. Hydrogen embrittlement[9] is used to describe at least four types of embrittlement phenomena:

(a). Hydrogen attack (e.g. H_2O formation in copper, methane reaction in steels).

(b). Hydride formation (e.g. hydride precipitation in niobium, titanium).

(c). Irreversible cracking (e.g. blistering of steel, cracking of Si-Fe)

(d). Reversible embrittlement (e.g. delayed failure in high strength steels).

In molybdenum, hydrogen causes reversible embrittlement, which is observed most readily with slow strain rates in a specific temperature range. The influence of strain rate and temperature are explained on the basis that for embrittlement to occur hydrogen should have enough time and mobility to diffuse to an internal defect or point of stress concentration. A fast strain rate and low temperature either decrease the time to diffuse or the mobility of hydrogen, thus minimizing embrittlement.

Among the theories proposed to explain reversible embrittlement, the following three[10] are the more popular:

(a). The pressure theory, initially presented by Zappfe[11] and modified by Tetelman[12], assumes that the hydrogen atoms in solution "precipitate" as a gas in voids and exert a pressure which is added to the applied stress, thereby decreasing the load-carrying ability of the metal.

(b). The adsorption theory was proposed originally by Petch[13], and Williams and Nelson[14]. According to this theory hydrogen

atoms are absorbed on the surfaces of voids and crack tips, thereby lowering the surface energy (and hence the fracture energy) thus facilitating crack propagation.

(c). The lattice interaction theory of Troiano[15], indicates that hydrogen in the lattice decreases the cohesive energy and thus weakens the base metal bond, lowering the fracture stress and promoting crack propagation.

Each of these theories explains some observed facts but none is general enough to account for all observations[10].

According to Cotterill[16], any general theory of hydrogen embrittlement should satisfy three conditions:

1. It must incorporate an explanation for the characteristics of each of the individual embrittlement effects observed in various metals.
2. It should be able to account for the absence of hydrogen embrittlement where such effects do not occur.
3. It must be compatible with the general aspect of
   (a). Hydrogen-metal relationships
   (b). Brittle fracture mechanisms

as they are each known at present.

Jones et al[17] have studied the relation between the magnetic susceptibility χ, the hydrogen affinity and the superconducting transition temperature T_c for various body centered cubic binary alloys of niobium, molybdenum and rhenium. They found that hydrogen solubility decreases continously as e/a increases and disappears for e/a = 5.6. Also, the density of states goes through a minimum at e/a = 5.6 suggesting that the hydrogen solubility and the superconducting transition temperature are both related to the energy-band structure of the alloys. The hydrogen ion in the lattice is screened by conduction electrons. The electronic structure of the alloy changes as e/a increases.

Investigation of the superconducting electrodynamic parameters i.e. transition temperature T_c , critical field at absolute zero H(0) and Kappa factor etc. offers a sensitive method of studying the effect of hydrogen interstitials on the properties of the metal, because of the extreme sensitivity of these parameters to small changes in the mean-free-path of the electrons in the normal state and to internal stresses and inhomogeneities caused by dislocations, point defects or disproportionate hydrogen distributions in the metal lattice. In the case of dilute Sn-, In-, and Al based alloys[18], small solute concentrations are found to decrease T_c in almost direct proportion to the increase in normal state resistivity ρ_n . Similar decreases in transition temperatures are observed when the mean-free-path is decreased by cold work, neutron irradiation, surface scattering or quenching. Seraphim et al [19] found that the decrease in transition temperature of tantalum on the addition of oxygen, nitrogen and hydrogen correlates with resistivity, but decreasing the mean-free-path by cold work does not decrease T_c . The influence of the mean-free-path on T_c is believed to be associated with the removal of the anisotropy of the energy gap[20] . DeSorbo[21] found that in Nb, the decrease in T_c caused by interstitial nitrogen and oxygen correlates roughly with the mean-free-path decrease.

In light of the above, we undertook to investigate the change of the electrical and mechanical properties of molybdenum with dissolved hydrogen. The results of these studies may help to improve the understanding of the phenomenon of "Hydrogen Embrittlement" in body-centered-cubic metals.

II. EXPERIMENTAL

A. SAMPLE

The samples used for superconducting measurements were cylindrical rods 82 mm. long and 3 mm. in diameter. Single crystals were obtained by electron-beam float-zone refining (three passes). For similar crystals obtained from Materials Research Corporation, typical chemical analysis stated in ppm are C= 5; O= 1; N= .5; H= .3; Fe= 5 . The crystals were grown with the (110) plane normal to the cylinder axis. Sample P4 was annealed[22] for 40, 20, 40 hours at 1100^{0} C in a quartz tube (10^{-7} mm. Hg), for 40, 40 hours in a McDanel tube at $1200\ ^{0}$C (10^{-7} mm. Hg) and for 20 hours at $2200\ ^{0}$C (10^{-10} mm. Hg). Superconducting measurements were made before and after each anneal. Sample P5 was cut mechanically by a jeweller's saw, from zone refined rod along with eight "test pieces", each of which was 20 mm. long and 3 mm. in diameter. The ends of the sample and the "test pieces" were mechanically polished to better than a micron finish. The sample P5 and the "test pieces" along with the "end pieces" and the thermal gradient rods (to be described in the next section) were annealed at $1100\ ^{0}$C in a quartz tube (10^{-6} mm. Hg). Due to an accidental diffusion pump shut-off, after two days, while the sample and other pieces were at high temperature , the surfaces were probably oxidised. The surface layer of the sample and the other pieces was removed by electropolishing in 25 % sulphuric acid in Ethyl Alcohol. After electropolishing, the sample P5, the "test pieces", the "end pieces" and the thermal gradient rods all were annealed for a week at $1100\ ^{0}$C.

B. HYDROGEN DIFFUSION

Molybdenum is an endothermic occluder of hydrogen[2,3] i.e. hydrogen forms a true solid solution with molybdenum. The solubility increases exponentially with temperature at constant pressure and as the square-root of the pressure at constant temperature. The solubility can be expressed as a function of pressure and temperature[23] by

$$S = S_o \; P^{1/2} \; \text{Exp.} \left[- \frac{Q_s}{2 R_o T} \right]$$

where S_o is a constant, P the pressure, T the absolute temperature and Q_s is the heat absorbed in calories per gram-molecule of hydrogen.

The factor of 2 in the denominator of the exponential takes into account the fact that hydrogen enters the metal lattice as atoms.

The solubility of hydrogen in molybdenum powder and wire was measured by Martin[24] and by Sieverts and Bruning[25]. Their results have been summarised by Dushmann[26] and Coterill[27]. Smithells and Ransley[28], and Fraunfelder[29] have studied the permeation of hydrogen through drawn molybdenum tubes. More recently Hill[30] and Oates and McLellan[31] have studied the solution of hydrogen in molybdenum (Hill quenched in water and Oats and McLellan in ethyl alcohol after heating in hydrogen at one atmosphere pressure). Hill obtained the following relations for solubility and diffusion coefficient:

$$S(\text{cm.}^3 / 100 \text{ gm.}) = 27 \text{ Exp.} \left[- \frac{9700}{RT} \right]$$

$$D(\text{cm.}^2 / \text{Sec.}) = 0.059 \text{ Exp.} \left[- \frac{14700}{RT} \right]$$

For a cylindrical sample of radius a , the concentration of the diffusing gas as a function of distance r from the axis

and time t of diffusion at temperature T is given by[32]

$$C(r,t) = C_o \left[1 - \frac{2}{a} \sum_{n=1}^{\infty} \frac{1}{\alpha_n} \frac{J_o(r\alpha_n)}{J_1(a\alpha_n)} \text{Exp.}(-D\alpha_n^2 t) \right]$$

where C_o is the solubility and D the diffusion coefficient of the diffusing gas in the medium of the sample at a temperature of diffusion T. $J_o(r\alpha_n)$ and $J_1(a\alpha_n)$ are Bessel's functions of the first kind and α_n are the positive roots of $J_o(a\alpha_n) = 0$.

Using the values of solubility and diffusion coefficient of hydrogen in molybdenum given by Hill, it was found that only a few minutes are required to saturate our samples at temperatures above 1000°C.

Because of the low solubility of hydrogen in molybdenum, diffusion was carried out at a high temperature. To avoid contamination of the sample by impurity diffusion from the sample holders, the sample was held in "end pieces" machined out of four-pass electron-beam float-zone refined molybdenum rod 6 mm. in diameter. The end pieces, four in number, were shaped in the form of an "H". They were thin walled (~1 mm.) and the holes on two sides were such that the sample, "test pieces" and thermal gradient rods fitted tightly. All the pieces were put together as shown in Fig. 1.

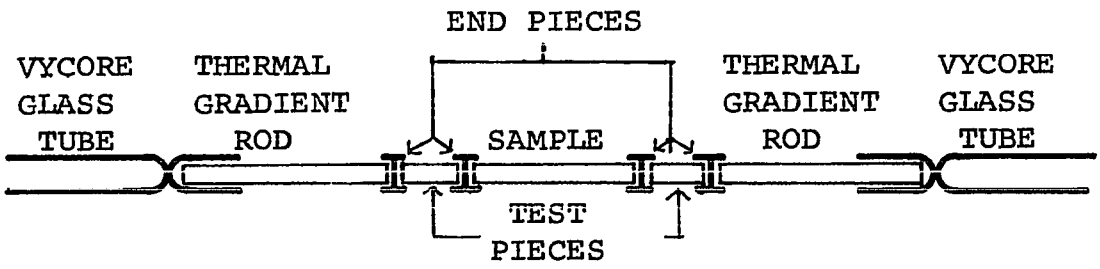

Fig. 1

Thermal gradient rods, also three mm. in diameter, were electron-beam float-zone refined single crystals and were annealed along with the sample, the "test pieces" and the "end pieces".

Diffusion was carried out by letting pure hydrogen, obtained by the palladium diffusion process, flow around the sample which was heated to the desired temperature in a RF furnance. The arrangement shown in Fig. 2 was used. The assembly shown in Fig. 1 was enclosed in a 12.7 mm. I.D. quartz tube. The ends of the quartz tube were sealed by brass pieces with center holes for passage of the Vycore tubes. To get a vacuum tight seal with both the quartz tube and the Vycore tube, two O-ring seals were used at each end as shown in Fig. 2.

The procedure followed for hydrogen diffusion was as follows:

(i). Start the water flow through the RF coil. Switch on the power supply for the RF furnance and let it warm up for about 30 minutes.

(ii). Close the inlet and vent valves of the palladium hydrogen purifier and switch on the heater to let it warm up.

(iii). Close V1, open V2 and V3. Switch on the mechanical pump, evacuate the quartz glass tube and watch the pressure on the manometer.

(iv). Open the inlet valve on the hydrogen purifier and close V3. Watch the pressure on the manometer. When the pressure in the quartz tube is equal to atmospheric pressure, open V1 and let hydrogen bubble through the oil bubbler for about five minutes.

(v). Close V1, and then open V3 for about two minutes. Close V3 again. Open the vent valve on the hydrogen purifier for a minute, to let out the impurities in the hydrogen gas which are concentrated in that region. Close the vent valve .

(vi). When the pressure inside the quartz tube is again equal to atmospheric pressure, close V2 and open V1 to let hydrogen bubble through the oil bubbler. Switch off the mechanical pump.

(vii). After letting hydrogen bubble for about two minutes the power in the RF coil is switched on and increased slowly until the sample reaches the desired temperature. The temperature was measured by a disappearing filament type optical pyrometer (Leeds & Northrop). Hydrogen was flowed by the sample during diffusion to sweep away other gases from the neighborhood of the sample.

(viii). After diffusion has proceeded for the desired length of time, the sample was quenched by cutting power to the RF coil. The power supply to the RF furnace was switched off, and the water supply to the RF coil cut off after five minutes. The heater on the palladium hydrogen purifier was switched off and the inlet valve closed.

The RF coil was wound from 6.3 mm. I. D. copper tubing and had nine turns. The coil was about 127 mm. long and its I. D. was slightly larger than the O. D. of the quartz tube. As shown in Fig. 2, the coil was arranged so that the sample was at the center of the coil.

Hydrogen was diffused in sample P5, after studying its superconducting properties, at 1553 K and again at 1823 K for two hours each. Superconducting measurements were made before and after each diffusion. The temperature was uniform within $\pm 100\ ^{\circ}C$ over the whole length of the sample, being maximum at the center.

The sample was called P5H1 after the first hydrogen diffusion at 1553 K and P5H2 after the second hydrogen diffusion at 1823 K.

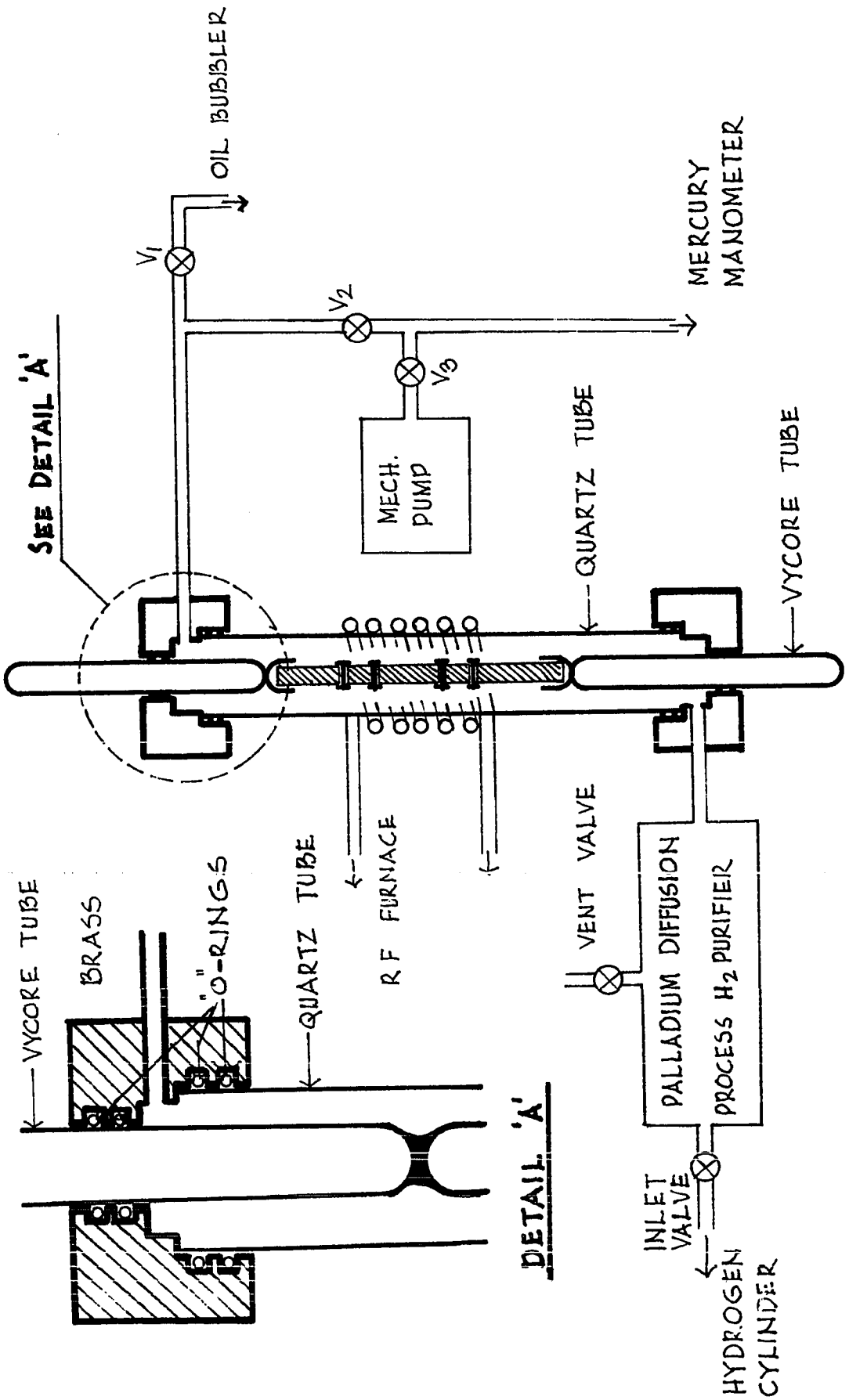
OIL BUBBLER
V1
V2
V3
MERCURY MANOMETER
MECH. PUMP
SEE DETAIL 'A'
QUARTZ TUBE
VYCORE TUBE
RF FURNACE
VENT VALVE
PALLADIUM DIFFUSION
PROCESS H2 PURIFIER
INLET VALVE
HYDROGEN CYLINDER
VYCORE TUBE
BRASS
"O"-RINGS
QUARTZ TUBE
DETAIL 'A'

Fig. 2

C. HYDROGEN ANALYSIS

To determine the amount of hydrogen dissolved in the sample P5 and P5H1, 13 mm. long pieces were cut mechanically by a jeweller's saw from the 20 mm. long "test pieces", two before hydrogen diffusion and two used with the sample for hydrogen diffusion. Hydrogen concentration in P5H2 was determined using two pieces each 13 mm. long cut from the ends of the sample after studying its superconducting properties. The samples used for hydrogen analysis were handled with tweezers, and care was exercised to avoid contamination by oils and grease[33]. Prior to hydrogen analysis the sample was cleaned with benzene, carbon tetrachloride and acetone in order, and weighed on a microbalance.

Hydrogen analysis was carried out with a Leco Hydrogen Analyser.

The principle of operation of the hydrogen analyser is as follows:

The sample is placed in a vaccum system of known volume, whose initial pressure P_1 is measured by a McLeod Gauge. The sample is heated in a RF furnace to about 1473 K. The gases evolved, because of the combination of high temperature and vaccum conditions, are collected and the new pressure P_2 is read on the McLeod Gauge. The gases collected are circulated through special copper oxide and anhydrone by means of a mercury diffusion pump. The copper oxide converts hydrogen to water which is absorbed by the anhydrone, leaving a pressure P_3 due to carbon monoxide, nitrogen etc. Thus (P_2-P_3) gives the pressure due to hydrogen alone. A simple calculation gives ppm by weight of hydrogen in the sample:

$$\text{ppm} = 0.0219 \quad \frac{(P_2 - P_3)}{\text{Sample mass in gm.}}$$

where 0.0219 is the calibration constant.

D. MECHANICAL MEASUREMENTS

The effect of dissolved hydrogen on the mechanical properties of molybdenum was determined from measurements of microhardness and Ultimate Tensile Strength (UTS).

Microhardness is a measure of the strain-hardening of a material. Microhardness tests were performed on the remaining 7 mm. long pieces out of the"test pieces" for P5 and P5H1. For P5H2 two 7 mm. long pieces were cut from the sample itself after its superconducting properties had been studied. The 7 mm. long pieces were mounted in "Silicone" mounts, polished to better than a micron finish, and tested on a Tukon Tester for Knoop Hardness Number (KHN).

The Knoop Indenter is pyramidal in form giving a diamond shaped (rhomb.) indentation, of which the diagonals have an approximate relation of 7 to 1 . The longitudinal angle is $172^{\circ}30'$ and the transverse angle is $130^{\circ}\ 0'$. The Tukon Tester applies loads upwards from 25 gm. Elastic recovery of the indentation produced by the Knoop Indenter takes place chiefly in a transverse direction rather than in a longitudinal direction, and consequently from the measured length of the long diagonal and the constants of the indenter, the dimensions of an indentation are closely related to the unrecovered length. The result of the test is expressed as the Knoop Hardness Number, which relates the applied load in Kilograms to the unrecovered (approximate) projected area in square mm. The Knoop Hardness Number I is expressed by the following formula

$$I = \frac{L}{Ap} = \frac{L}{l^2 cp}$$

where L is the load (in Kgm.) applied to the indenter

Ap the unrecovered projected area of indentation (in square mm.)

l the measured length of long diagonal of the indentation (in mm.)

and cp is a constant relating l to the projected area

For a perfect Indenter of $172^{\circ}\ 30'$ longitudinal angle and $130^{\circ}\ 0'$ transverse angle, $cp = 7.028 \cdot 10^{-2}$.

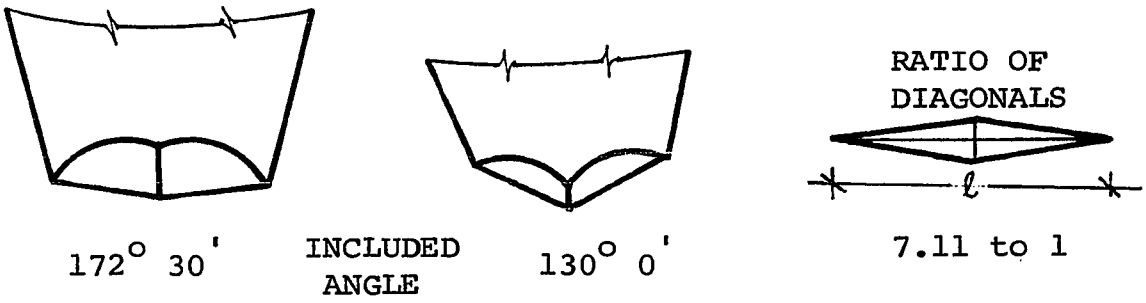

Fig. 3

In our measurements we used a 1.0 Kgm. load and 20X magnification. The Knoop Hardness Number (KHN) was then read from the Hardness Number Calculater.

The Ultimate Tensile Strength (UTS) was measured from the Stress-Strain curves of the sample obtained by pulling the sample on an Instron Machine. Stress-Strain curves were obtained by pulling a "test piece" representative of sample P5 and a part of sample P5H2, after superconducting measurements had been made. These measurements were done at Liquid Nitrogen temperature. The UTS of P5H2 was found to be almost twice that of P5. To further investigate this interesting result, measurements were made on two samples annealed for 7 hours at $1100^{\circ}C$ and another two after similar annealing treatment and charging with hydrogen for 5 min. at $1200^{\circ}C$. The Stress-Strain curves were obtained at room temperature.

E. SUPERCONDUCTING MEASUREMENTS

To study the effect of hydrogen solution on superconducting properties, measurements were first made on the well-annealed sample P4, which were taken as representative of pure strain free molybdenum. Then P5, P5H1 and P5H2 were investigated.

Superconducting measurements were made in a He-3 cryostat described in detail by Mallon[34]. It is a standard "Single Condensation" design (i.e. He-3 is alternately condensed and evaporated), capable of reaching temperatures above 0.35 K. The low temperature part of the cryostat is shown in Fig. 4. The He-3 condenses along the inside of the transfer line, which is surrounded by liquid He-4 at 1 K. Liquid He-3 condenses at 1 K, runs down the transfer line and accumulates in the reservoir. When condensation is complete, the He-3 vapor is pumped to reduce the temperature of the liquid He-3 bath and the sample. The molybdenum sample is held in a silver tube. The sample and the bottom of the sample tube are immersed in liquid He-3. The liquid reservoir is above the sample. For temperature stablisation, particularly in the neighborhood of the critical temperature, a manganin wire heater (room temperature resistance $\sim$200 Ohms) was wound just under the He-3 reservoir . A temperature regulator, copied after that of C. Blake and C. E. Chase[35], was used in conjunction with the heater and a 0.1 Watt resistor (room temperature resistance 10 Ohms), to maintain the temperature constant to 0.1 millidegree for any length of time. Temperature was determined by measuring the resistance of a 0.5 Watt carbon resistor (room temperature resistance 2.7 Ohms) by a Wheatstone Bridge. The resistor had been

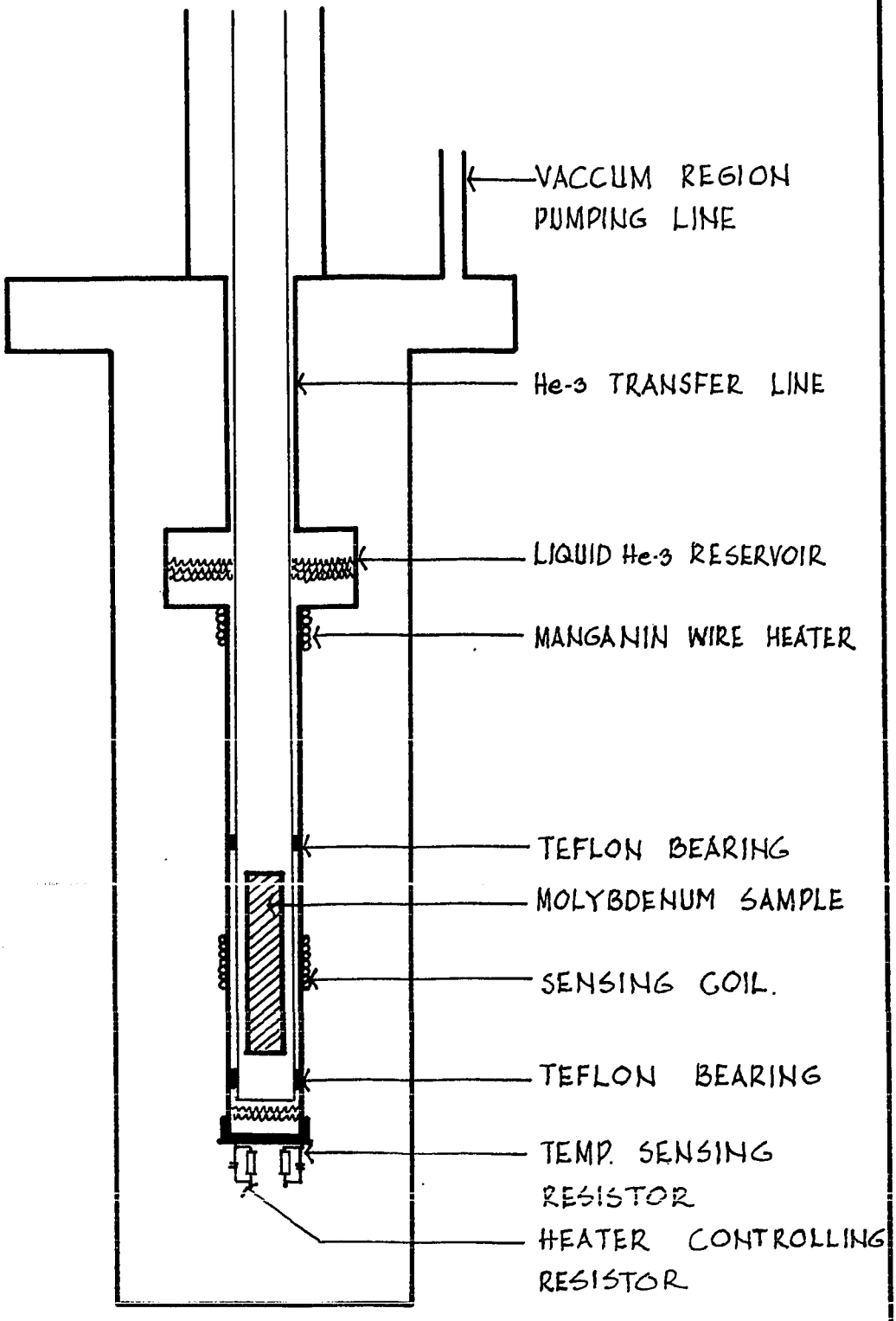
VACCUM REGION
PUMPING LINE
He-3 TRANSFER LINE
LIQUID He-3 RESERVOIR
MANGANIN WIRE HEATER
TEFLON BEARING
MOLYBDENUM SAMPLE
SENSING COIL.
TEFLON BEARING
TEMP. SENSING
RESISTOR
HEATER CONTROLLING
RESISTOR

FIG. 4.

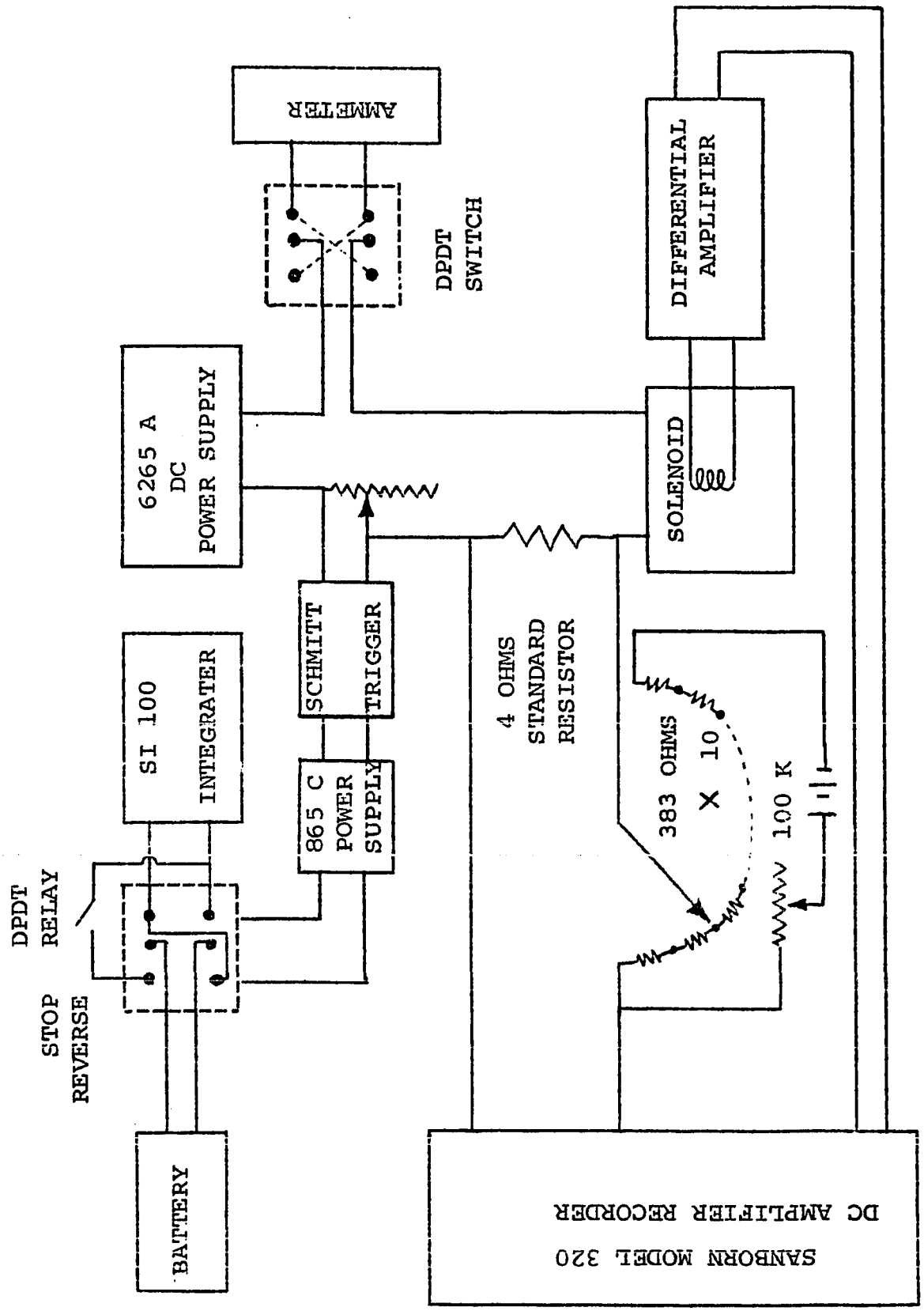
AMMETER
DPDT SWITCH
DIFFERENTIAL AMPLIFIER
6265 A DC POWER SUPPLY
SOLENOID
SCHMITT TRIGGER
SI 100 INTEGRATER
865 C POWER SUPPLY
4 OHMS STANDARD RESISTOR
383 OHMS X 10
100 K
DPDT RELAY
STOP
REVERSE
BATTERY
SANBORN MODEL 320
DC AMPLIFIER RECORDER

calibrated against He-3 vapor pressure measurements from 0.6 to 1.08 K using the T 62 temperature scale. The resolution of the temperature measurements was 10^{-4} K.

The magnetic field was produced by a liquid nitrogen cooled, end compensated solenoid. The magnetic field was uniform to ± 0.5 % over the sample volume. The current for the solenoid was supplied by a Regulated Power Supply (H. P. Model 6265 A) operated in constant current mode (Remote Voltage Programming), driven by an Integrator (TRE Model SI 100). The magnetic field was calculated from the voltage across a standard 4 Ohm. resistor in series with the solenoid. The caliberation characteristic[36] of the solenoid is 284 Gauss/Ampere. The measurement of magnetisation in the sample was provided by the voltage induced in the sensing coil (2800 turns) wound on the guide tube around the sample. The voltage induced in the sensing coil after amplification by a Differential Amplifier (Gain 1000) (Sanborn Model 8875A), and the voltage across the standard 4 Ohm. resistor in the solenoid circuit were simultaneously recorded as a function of time on a high speed Dual-Channel D C Amplifier Recorder (Sanborn Model 320). The magnetic field can be swept linearly from 10^{-3} to 20 Gauss/Sec. The field can also be stopped and held at any value.

For greater resolution of the magnetic field measurements, a zero offset step voltage was introduced in the magnetic field channel. Magnetic field changes of 0.05 Gauss and induced voltages up to 1 μV. could be resolved.

The earth's magnetic field in the region of the sample was cancelled by a pair of Helmholtz coils placed outside the cryostat. Also wrapped around the cryostat were 12 layers of "Permalloy", with Aluminum sheet pasted on the inside[37].

Before each set of measurements the "Permalloy" was demagnetised[38] by passing up to 10 ampere a c through 30 turns of copper wire wound as a toroid around the shields. The current was increased to 10 ampere and decreased to zero slowly several times.

A dynamic method[22] of measurement was used. The magnetic field is swept at the desired rate up to a value higher than the critical field H_c, and then back to zero, recording simultaneously the voltage induced in the sensing coil and the magnetic field as function of time. Transition curves similar to those shown in Fig. 5 were obtained. Such measurements were repeated at various temperatures between 0.35 K and T_c. The critical field H_c and the supercooling field H_s were read directly from these plots.

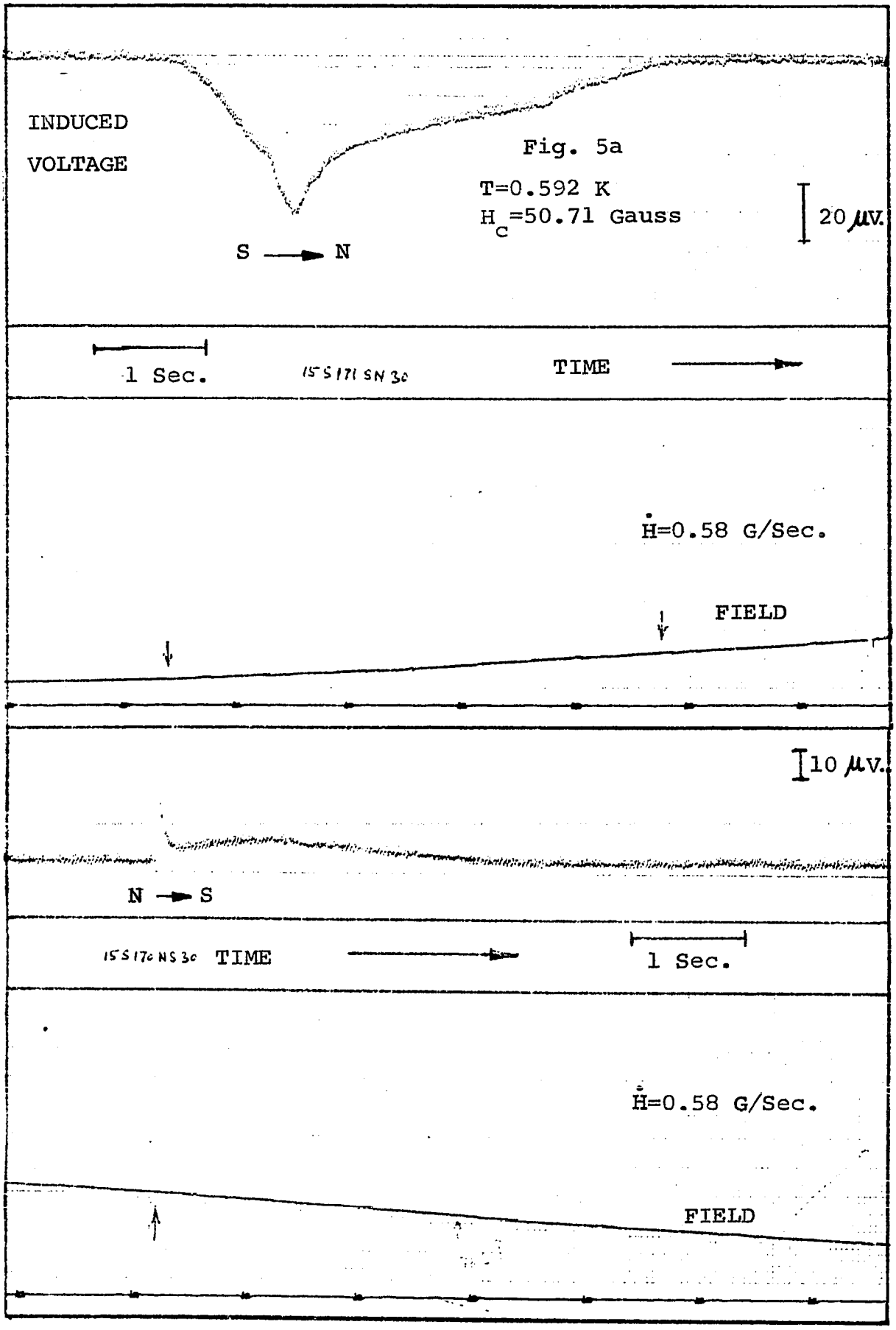
INDUCED
VOLTAGE
Fig. 5a
T=0.592 K
H_c=50.71 Gauss
20 μV.
S → N
1 Sec.
15 S 17l SN 3c
TIME
$\dot{H}$=0.58 G/Sec.
FIELD
10 μV.
N → S
15 S 17c NS 3c
TIME
1 Sec.
$\dot{H}$=0.58 G/Sec.
FIELD

III. RESULTS

A. PHASE TRANSITION AND RESISTIVITY

The external applied magnetic field is swept from zero at a fixed rate $P = \frac{dH}{dt}$. When the applied field becomes equal to the critical field at the sample temperature, the magnetic flux starts to penetrate the sample. Faber[39-43] has shown that the normal phase nucleates at a point on the surface and then propagates simultaneously along the surface and into the sample volume. Pippard[44] has given an electrodynamic theory of flux penetration for the case that an external applied magnetic field $H > H_c$ is suddenly switched on. An extesion of Pippard's theory to the case of a linearly increasing magnetic field, and a comparison with observed pulses, is given in Appendix I. Fig. 6 shows a typical induced voltage pulse as a function of time for samples P4 , P5 , P5H1 and P5H2 respectively. Pronounced changes in pulse shapes occur in the region before the peak. Clearly the surface of sample P5 is damaged, because the pulse-rise to the peak is not smooth. Such a fine structure is visible only for lower field sweep rates and temperatures well below the transition temperature. After the first hydrogen diffusion, it appears that the surface damage has been partially removed. That is why there are two peaks. Sample P5H2 shows a very smooth pulse-rise and no sign of damage. A very smooth pulse indicates there are no inhomogenities or strains in the sample which might have arisen if hydrogen had been concentrated at preferred sites.

As shown in Appendix I equation A.11 the time t_o required for the completion of the superconducting to normal

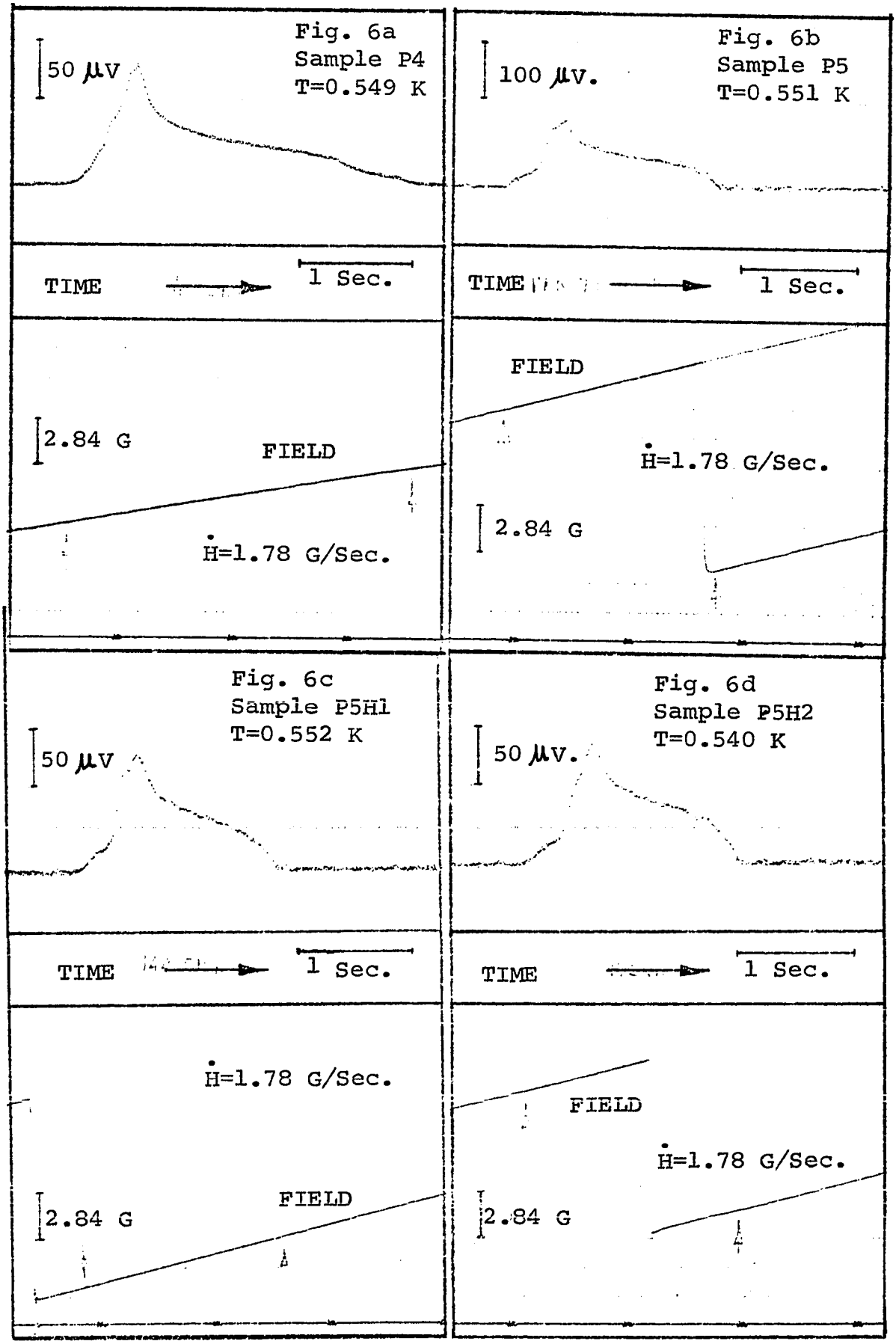
Fig. 6a
Sample P4
T=0.549 K
50 μV
TIME
1 Sec.
2.84 G
FIELD
Ḣ=1.78 G/Sec.
Fig. 6b
Sample P5
T=0.551 K
100 μV.
TIME
1 Sec.
FIELD
Ḣ=1.78 G/Sec.
2.84 G
Fig. 6c
Sample P5H1
T=0.552 K
50 μV
TIME
1 Sec.
Ḣ=1.78 G/Sec.
2.84 G
FIELD
Fig. 6d
Sample P5H2
T=0.540 K
50 μV.
TIME
1 Sec.
FIELD
Ḣ=1.78 G/Sec.
2.84 G

(S→N) transition depends, for a given magnetic field sweep rate P, on the electrical conductivity σ of the sample:

$$t_o^2 = \frac{2\pi\sigma a^2}{P C^2} H_c$$

From the observed times, therefore, one can calculate electrical conductivity. Fig. 7 shows plots of resistivity in Ohm. cm. as a function of temperature. The behaviour of resistivity is quite unexpected and is not yet clearly understood. There is, however, some doubt as to the determination of the transition time t_o . One of the assumptions made to obtain the relation connecting conductivity to transition time is that a normal ring is formed on the sample surface at time t = 0 . In the pulses obtained this corresponds to the peak, which means that we should probably count the time from the peak to the end. But then the flux entering the sample should be corrected for the flux that has already entered the sample when the peak is reached. This may be taken into account by using an effective radius for the sample, reduced by the ratio of the flux entering the sample after the peak to the total flux. Another factor which should be taken into account is the presence of a magnetic field during the phase transition. Galvanomagnetic effects will modify the conductivity, although such effects are expected to be small close to the transition temperature, because the magnetic fields involved are small. The latent heat of the phase transition has also not been considered.

In Appendix II we have calculated the contribution to the residual resistivity due to dissolved hydrogen in molybdenum. The result is in reasonable agreement with the observed value.

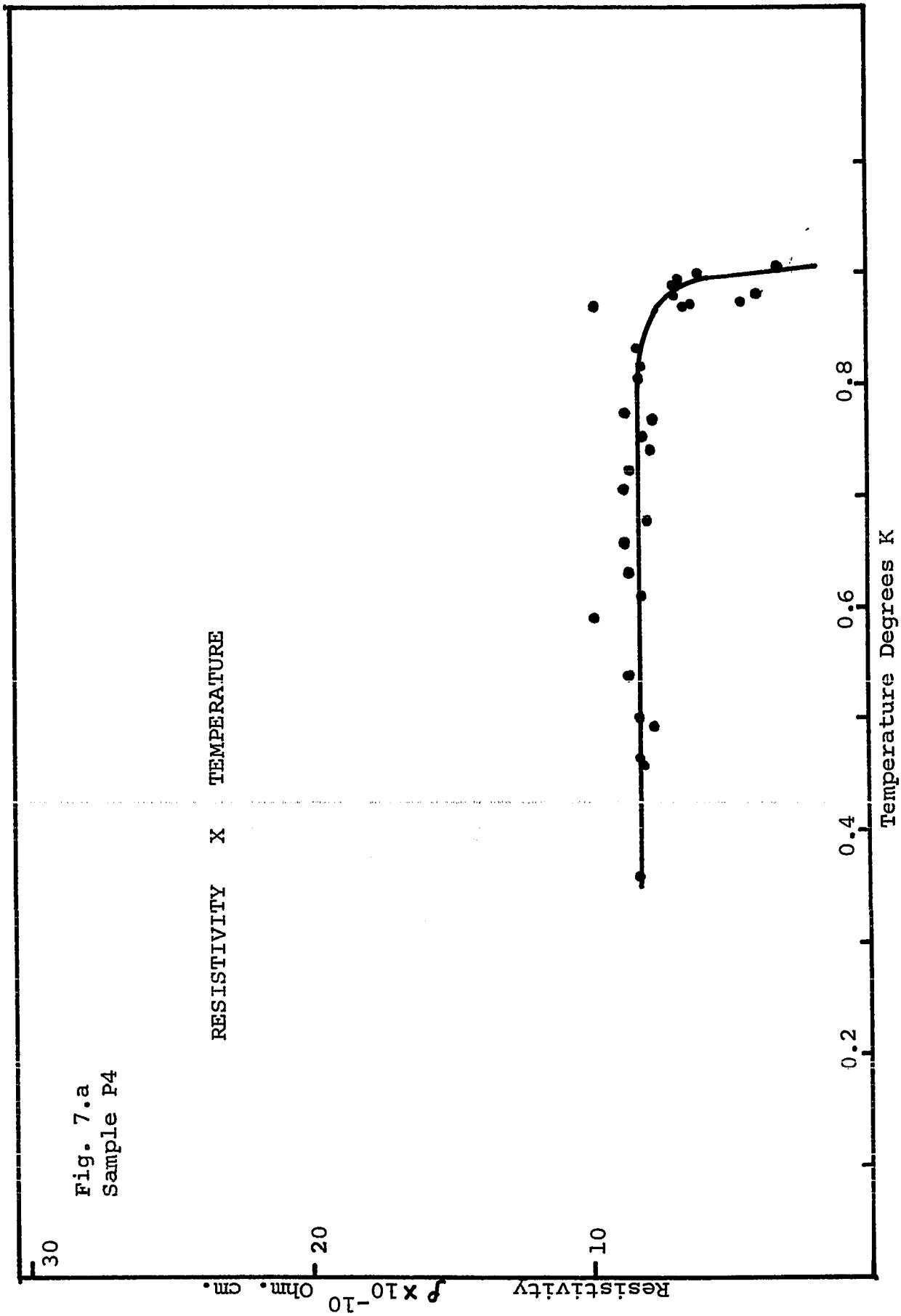

Fig. 7.a
Sample P4

RESISTIVITY X TEMPERATURE

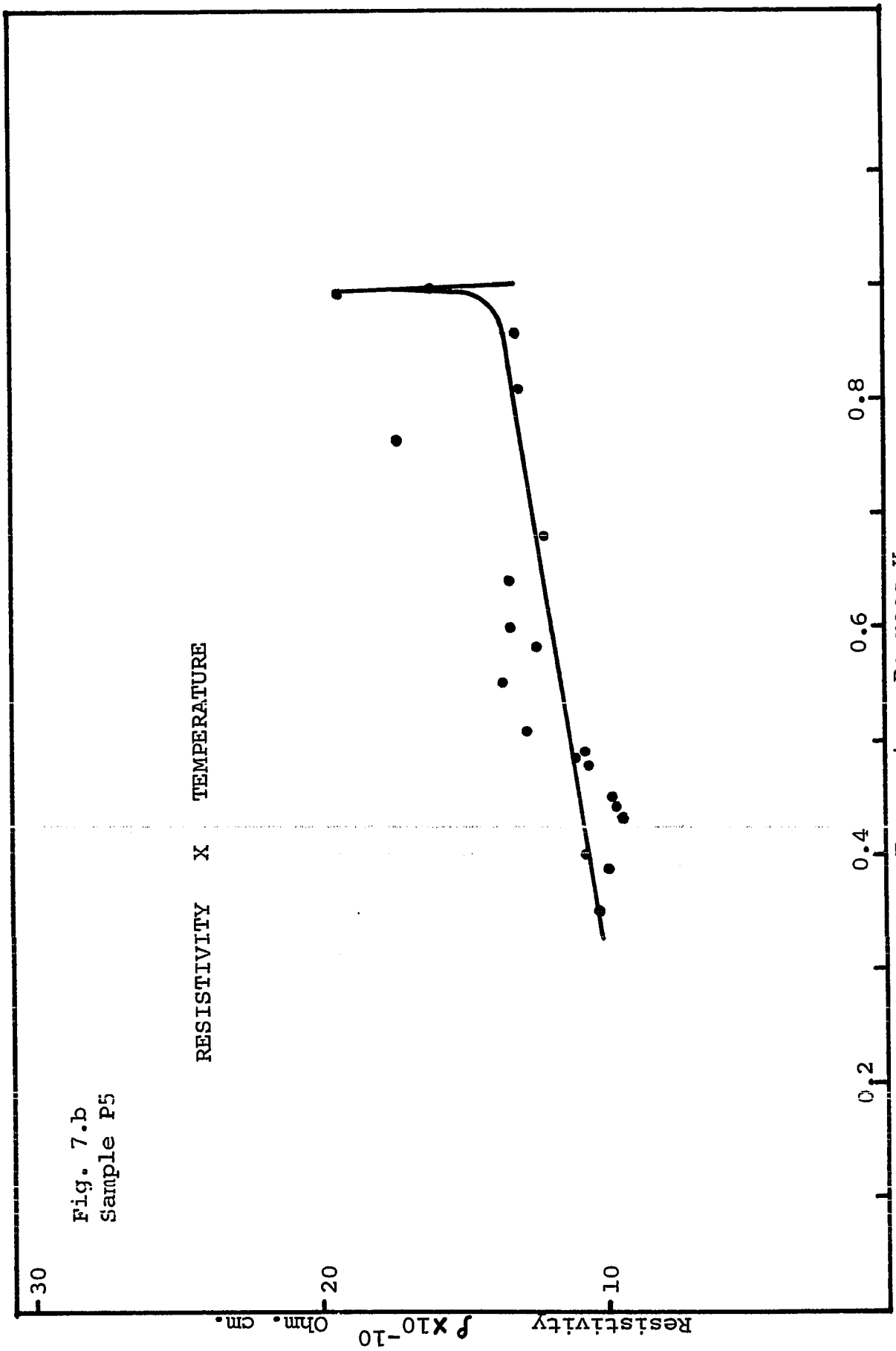

Fig. 7.b
Sample P5

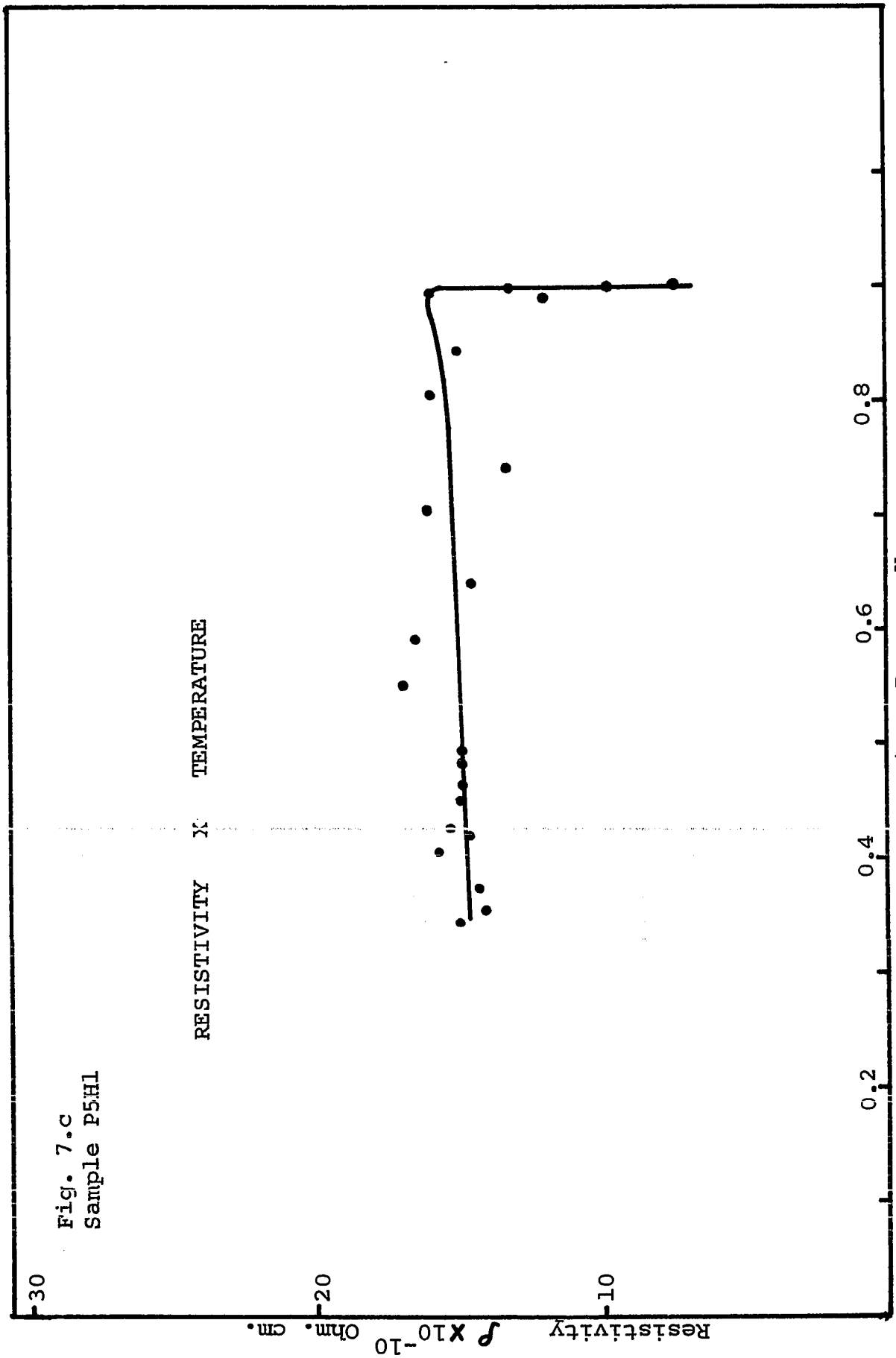

Fig. 7.c
Sample P5H1

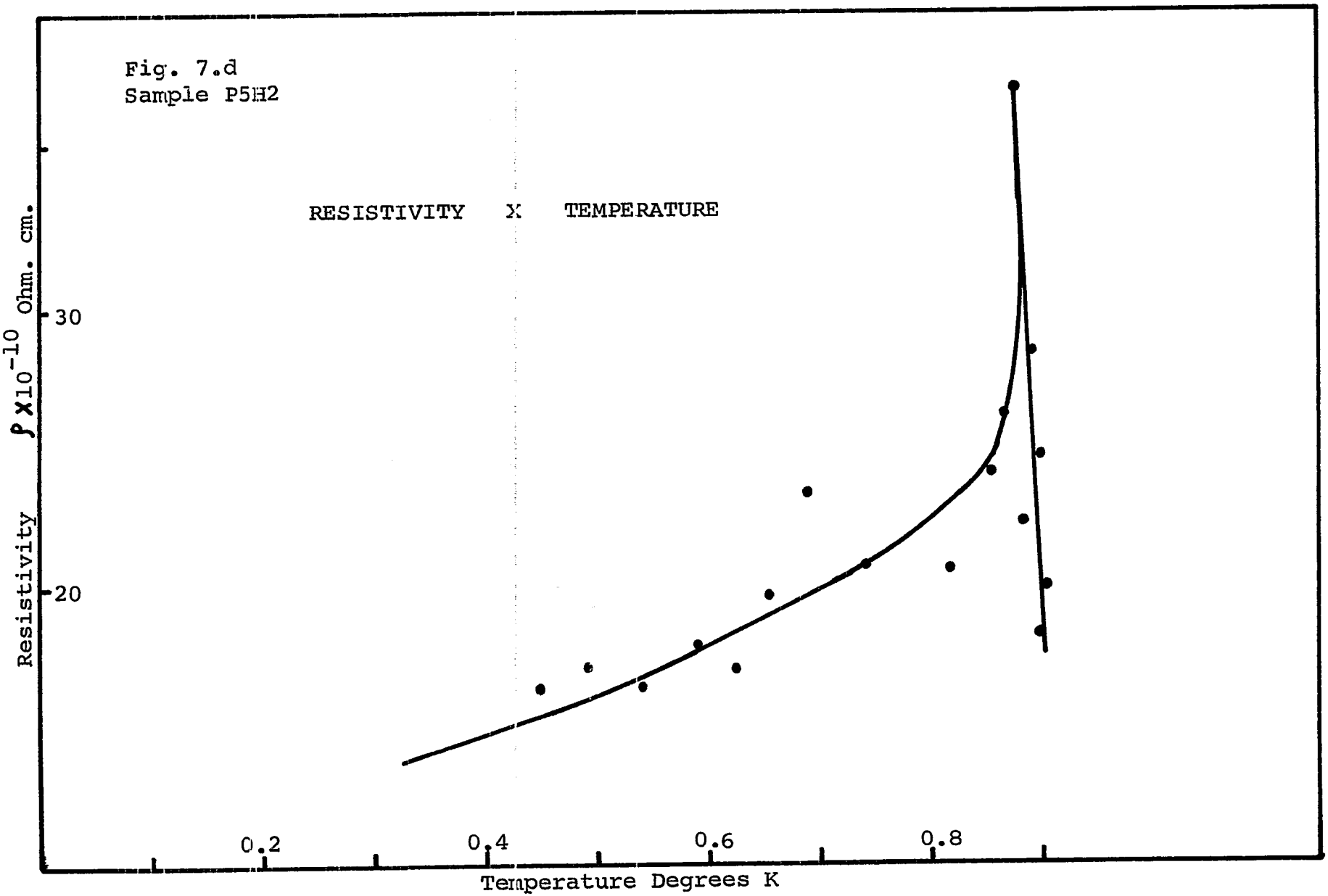
Fig. 7.d
Sample P5H2
RESISTIVITY X TEMPERATURE
Resistivity ρ X10^-10 Ohm. cm.
30
20
0.2
0.4
0.6
0.8
Temperature Degrees K

B. SUPERCONDUCTING PARAMETERS

(i) CRITICAL TEMPERATURE

Molybdenum is a weak coupling type I superconductor ($T_c / \Theta_D = 0.91/ 460$)[45]. Although molybdenum shows a reduced isotope effect[46], casting doubts about the electron-phonon coupling being the only mechanism responsible for the origin of superconductivity, in the absence of any better alternative the BCS theory[47] provides a guideline to understand the experimental results.

According to BCS theory the critical temperature is given by

$$kT_c = 1.14\, \hbar\omega \ \text{exp.} \left[- \frac{1}{N(0)\ V} \right]$$

or

$$T_c = 0.85\, \Theta_D \ \text{exp.} \left[- \frac{1}{N(0)\ V} \right]$$

where N(0) is the electronic density of states for a single spin at the Fermi surface, V is the average attractive interaction between electrons, k Boltzmann's constant and $\hbar\omega$ is the phonon energy (proportional to the Debye temperature Θ_D : $\hbar\omega_D = k\ \Theta_D$). Since V is in general unknown, T_c can not be predicted for specific materials. However this equation does indicate the dependence of T_c on Θ_D and the great importance of N(0).

When hydrogen is dissolved in molybdenum any or all of Θ_D , N(0) and V can change. Independent of these effects , a small depression of T_c occurs in very dilute alloys that is mean-free-path dependent[48] and has been associated with the removal of energy gap anisotropy

present in the pure material. In pure materials the energy gap is anisotropic, depending on the momentum direction of the electrons, and T_c is primarily dependent on the larger value of the gap. Scattering causes a mixing of plane wave states that averages over the entire Fermi surface, and T_c is determined by the overall average gap. Thus T_c decreases, the decrease being dependent on the amount of scattering (mean-free-path) and the degree of gap anisotropy in the pure material. The gap anisotropy should be essentially removed and the resulting decrease in T_c completed when the mean-free-path has been decreased to appreciably less than the initial coherence length ξ_o .

Markowitz and Kadanoff[49], and also Ginsberg[50] have estimated the change in T_c in terms of the residual resistance ratio of the material $\rho_r = R_{4.2} / (R_{273} - R_{4.2})$.

$$\Delta T_c = A \rho_r + B \rho_r \ln \rho_r \qquad \text{for} \quad 1 < \varkappa < 100$$

where $\varkappa = \alpha^i \theta \rho_r$

α^i is a constant of order unity, θ a constant dependent on the host material only and

$$A = \left(K^i + \langle a^2 \rangle T_c \left[- 0.36 + 0.078 \ln(\alpha^i \theta) \right] \right) \alpha^i \theta$$

$$B = 0.078 \langle a^2 \rangle T_c \alpha^i \theta$$

$$\langle a^2 \rangle = \left\langle (\Delta_k - \langle \Delta_k \rangle)^2 / \langle \Delta_k \rangle^2 \right\rangle .$$

where Δ_k is the energy gap, and K^i is an impurity dependent

constant. Clem[51] has shown that for small α (i.e. $\alpha < 1$)

$$\frac{\Delta T_c}{\rho_r} = \left(0.393 \langle a^2 \rangle T_c + K^i \right) \Theta \alpha^i + 0.535 \langle a^2 \rangle T_c (\Theta \alpha^i)^2 \rho_r$$

This weak coupling anisotropy theory of superconductivity has been shown to describe well the T_c and H_c behaviour of alloy systems with Sn as host[52]. However it does not explain the observed behaviour of either T_c or H_c in the Indium-Thallium alloy system[53].

In our measurements, since we did not measure the resistivity ratio, correlation with anisotropy theory can not be made. We do get an estimate of resistivity as has been described in the last section above.

When hydrogen was added to molybdenum the transition temperature was found to decrease a little from 0.910 to 0.904, which is about the error in our temperature measurements. Table I shows critical temperatures obtained by extrapolating the H_c versus T plot to $T = T_c$ (Fig. 8). For sample P5, because the surface was damaged, the H_c versus T plot up to 0.89 K was extrapolated to T_c.

Fig. 8.a
Sample P4

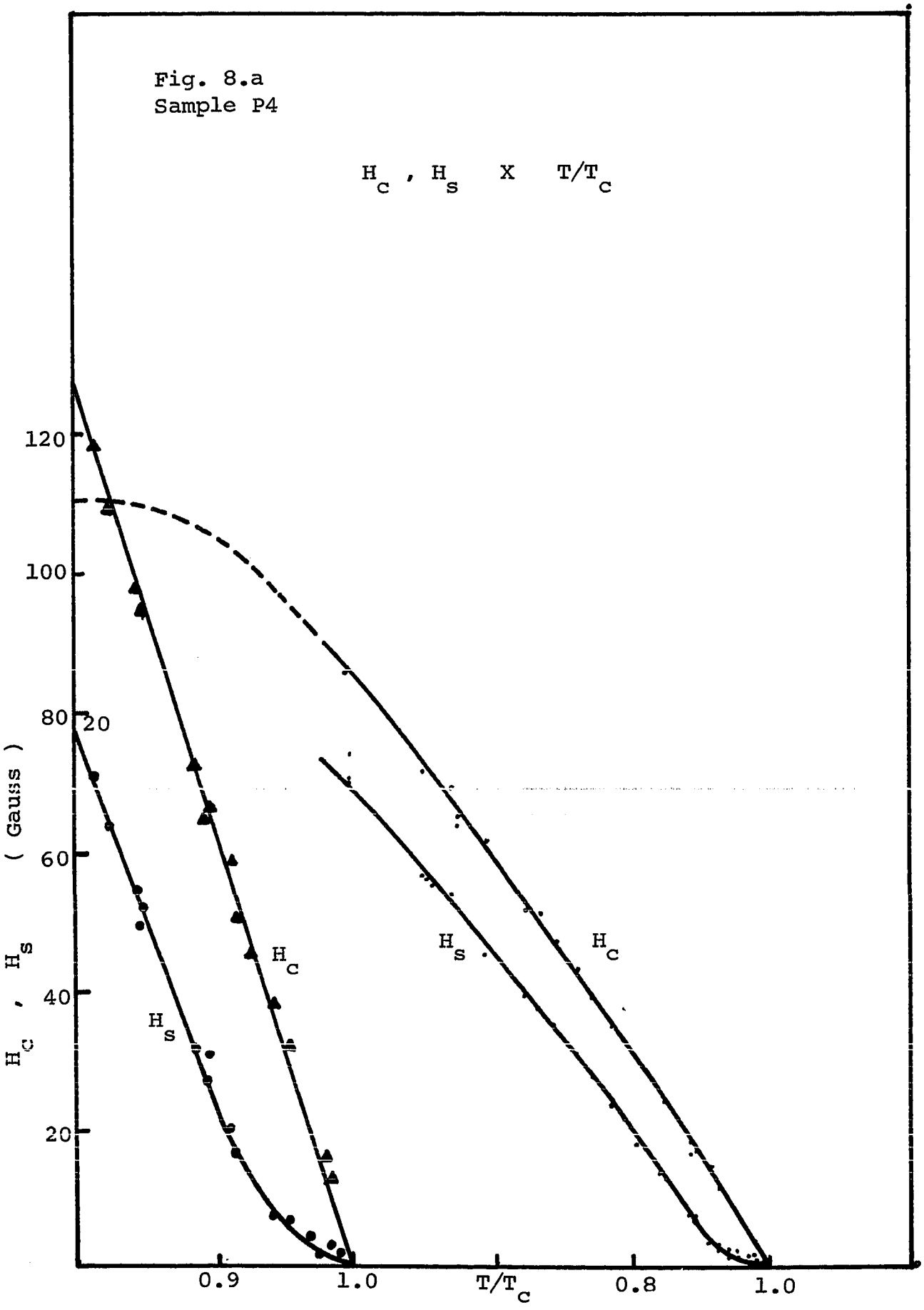

Fig. 8.b
Sample P5

H_c , H_s X T/T_c

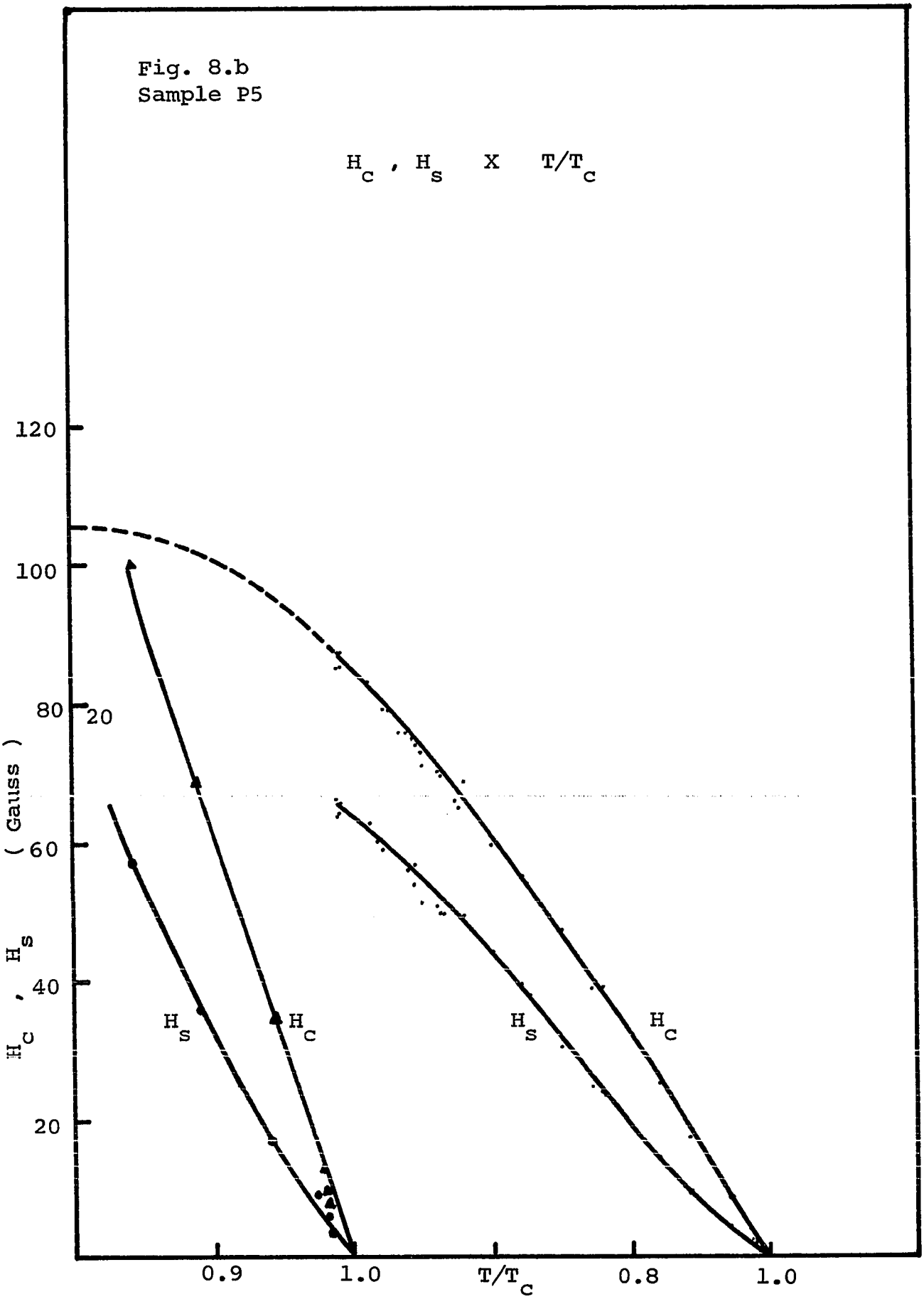

Fig. 8.c
Sample P5H1

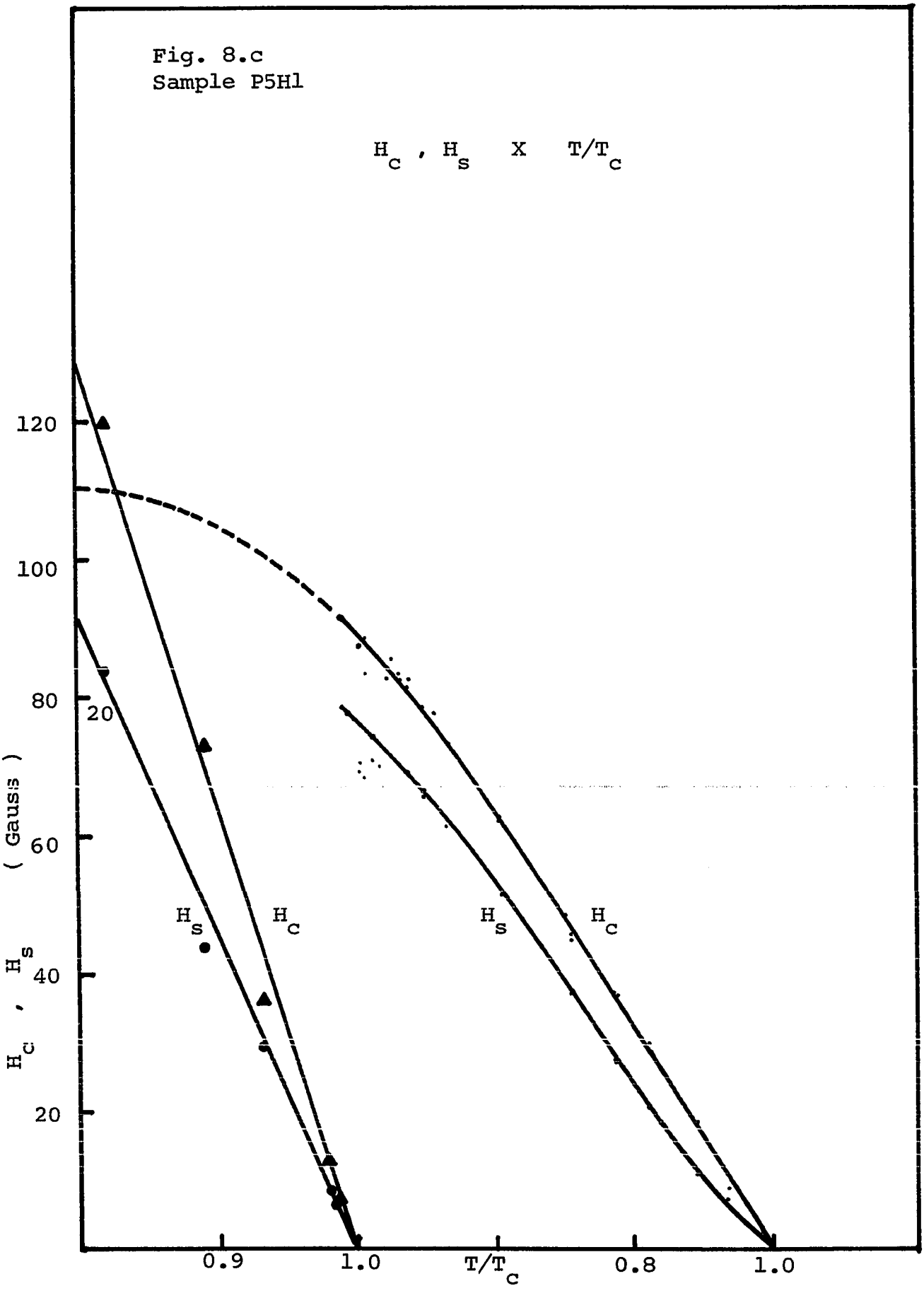

Fig. 8.d
Sample P5H2

H_c , H_s X T/T_c

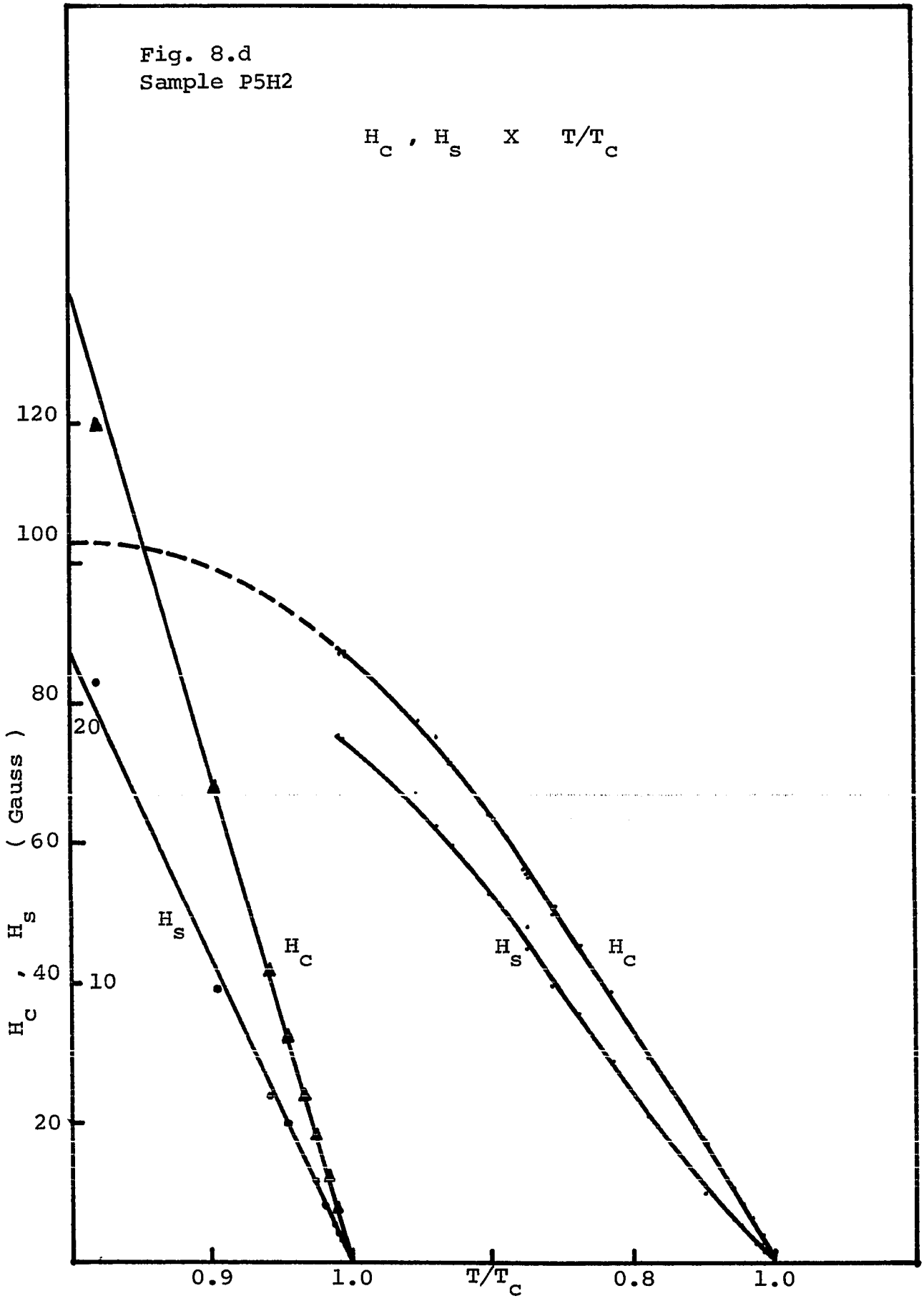

TABLE I

Results of superconducting measurements

Sample	History	Critical Temperature T_c ±.005 K	Extrapolated $H_c(0)$ ± 3 G	$-\left(\frac{dH_c}{dT}\right)_{T=T_c}$ Gauss/K	$K_o = .42 \left(\frac{H_s}{H_c}\right)_{T=T_c}$
P4	Annealed (40+40)Hrs. 1200°C (40+20+40)Hrs. 1100°C 20 Hrs. 2200°C	0.912	110.8	170.87	0.065
P5	Annealed 168 Hrs. 1100°C	0.910	105.7	175.0	0.315
P5H1	P5 after hydrogen diffusion at 1200°C H_2 conc. 0.2 ppm wt.	0.905	110.5	187.1	0.281
P5H2	P5H1 after second hydrogen diffusion at 1550°C for 2 Hrs. H_2 conc. 0.33 ppm wt.	0.904	103.6	195.3	0.265

(ii) CRITICAL FIELD

The critical field at absolute zero H(0) was obtained by extrapolating H_c versus $(T/T_c)^2$ plots to T=0 K. Figure 9 shows the plots of H_c versus $(T/T_c)^2$. Values of H(0) obtained are collected in Table I. There does not seem to exist any correlation between H(0) and T_c as would be expected according to the "Similarity Principle"[54]. This probably is due to the extrapolation, which is not accurate because our measurements do not extend to low enough temperatures, $T/T_c \geq 0.345$.

Also collected in Table I are the slopes $\frac{dH_c}{dT})_{T_c}$ obtained from the H_c versus T/T_c plots near the critical temperature T_c .

$\frac{dH_c}{dT})_{T_c}$ is related to the electronic density of states at the Fermi surface, according to BCS theory[47], by:

$$\gamma = \frac{1}{19.4} \left(\frac{dH_c}{dT}\right)^2_{T_c} \quad \text{Erg. cm.}^{-3}\text{K}^{-2}$$

$$= \frac{10^{-3}}{19.4} \left(\frac{dH_c}{dT}\right)^2_{T_c} \quad \text{mJ. Mole}^{-1}\text{ K}^{-2}$$

The coefficient γ of the normal electronic specific heat is related to the density of electronic states at the Fermi surface N(0) by[47]:

$$N(0) = \frac{3}{2} \frac{\gamma}{\pi^2 k^2} \quad \text{Erg.}^{-1}\text{ cm.}^{-3}$$

where γ is in Erg. cm.$^{-3}$ K^{-2}.

Fig. 9.a
Sample P4

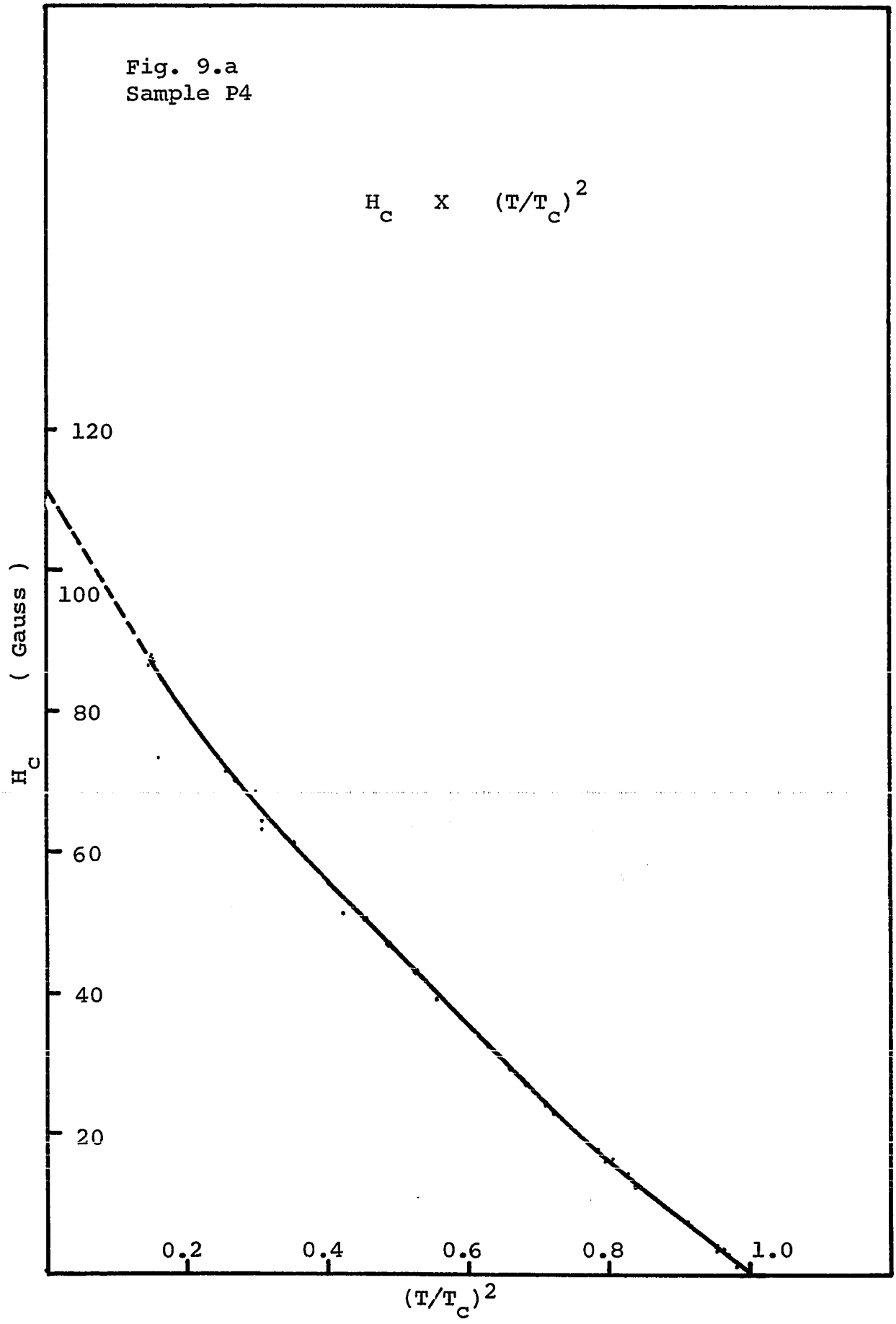

Fig. 9.b
Sample P5

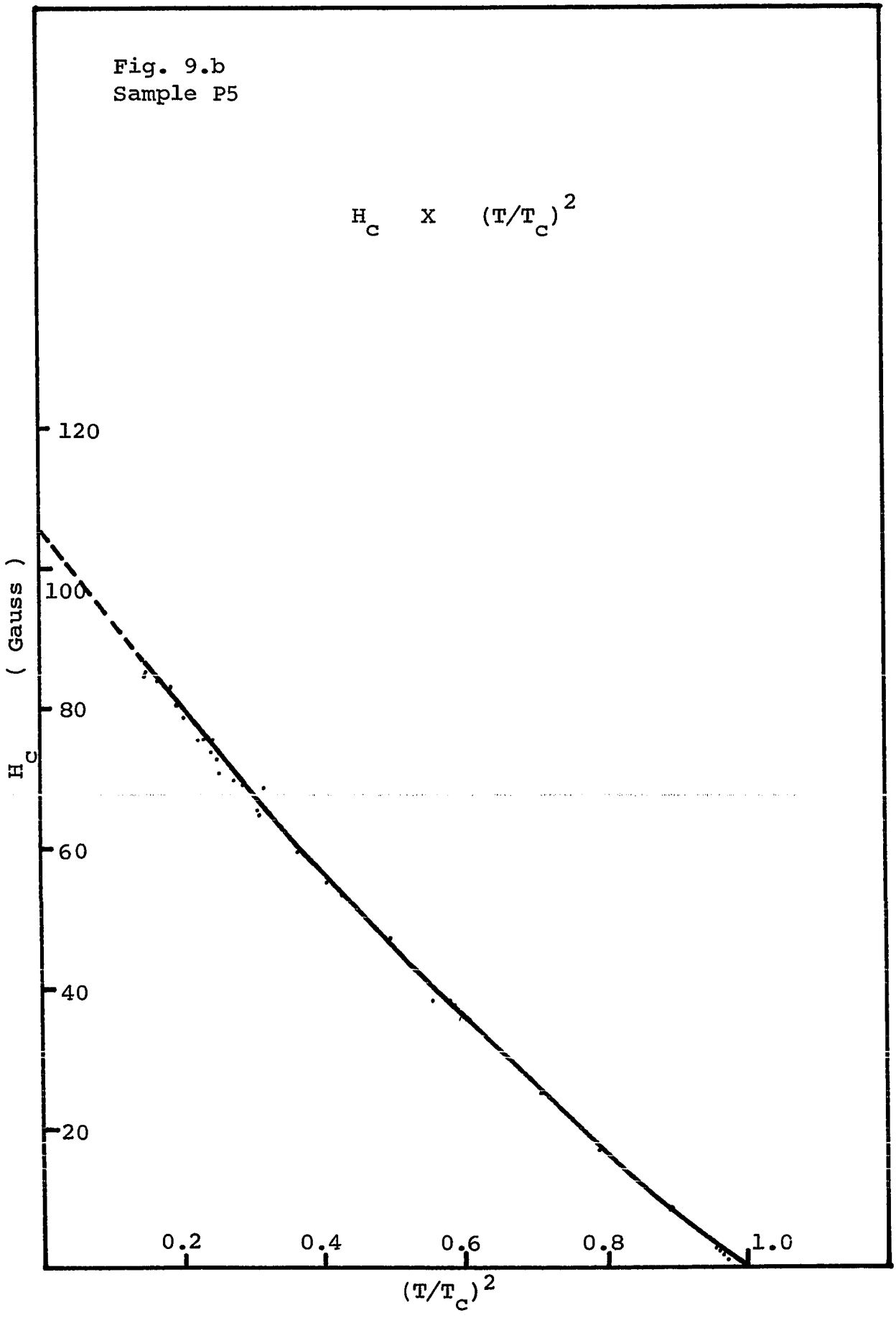

Fig. 9.c
Sample P5H1

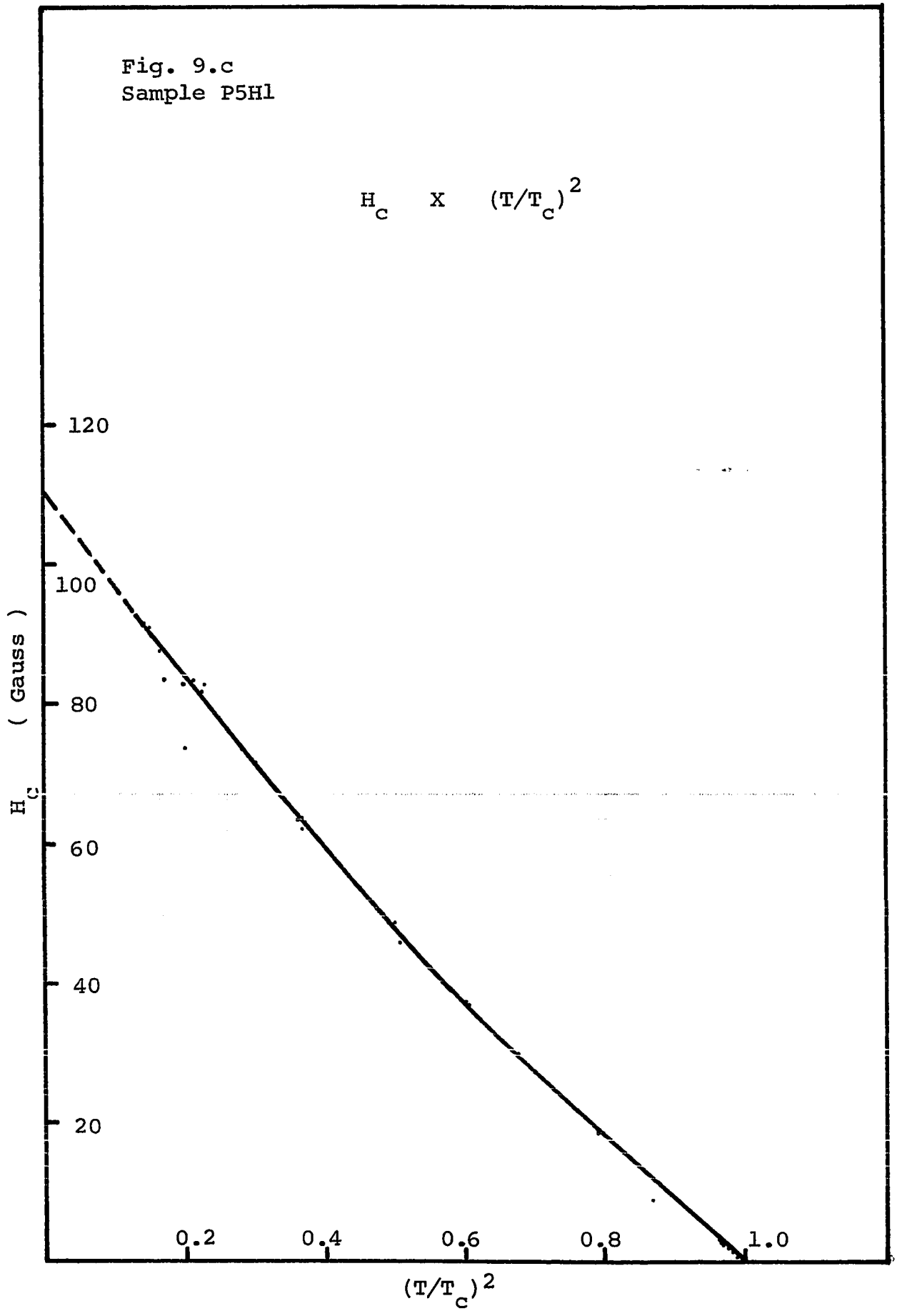

Fig. 9.d
Sample P5H2

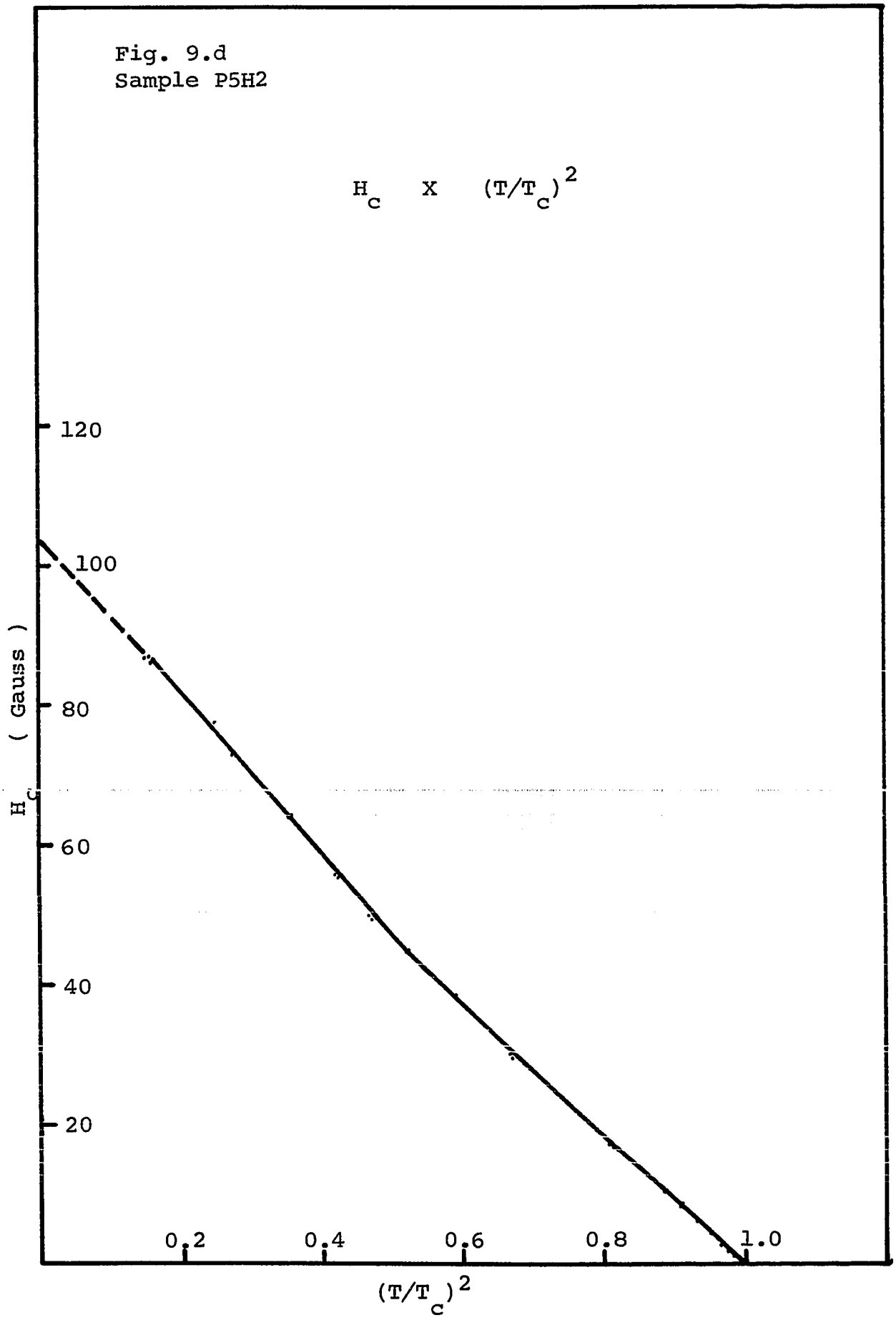

Also related in the BCS theory are the slope $\frac{dH_c}{dT})_{T_c}$ and the critical field at absolute zero :

$$\frac{dH_c}{dT})_{T_c} = -1.82 \frac{H(0)}{T_c}$$

The energy gap parameter Δ_k has been derived by Goodman[55] :

$$\frac{2\Delta_k}{kT_c} = \frac{4\pi}{\sqrt{3}} \left[\frac{H^2(0)}{8\pi\gamma T_c^2} \right]^{1/2}$$

Values of γ, N(0) and Δ_k calculated using the relations above are collected in Table II.

TABLE II

Results of calculations using BCS theory

Sample	H(0) Gauss	γ mJ. mole^{-1} K^{-2}	N(0) Erg^{-1}cm.$^{-3}$	$\frac{2\Delta_k}{kT_c}$
P4	85.6	1.505	12.04 10^{33}	4.53
P5	87.5	1.578	12.62 10^{33}	4.26
P5H1	93.03	1.804	14.43 10^{33}	4.16
P5H2	97.01	1.966	15.73 10^{33}	3.74

In superconductors, the changes in critical temperature and critical field due to impurities can be of two types. First are those independent of the kind of impurity (i.e. caused by changes in the isotropic-mean-free-path IMPF, of the electrons and the associated changes in the anisotropy of the superconducting energy gap Δ_k). Others are impurity dependent, i.e. the so called "valence effects" caused by changes in the basic parameters of the metal, such as electronic density of states. Clem[51] has shown that in the weak coupling limit the ratios

$$\frac{VH_o^2}{8\pi T_c^2 \gamma} \left(= \bar{H}_o^2 \right) \quad \text{and} \quad \frac{T_c}{H_o}\frac{dH_c}{dT}\Big)_{T_c} = \frac{dh}{dt}\Big)_{t=1}$$

where $h = \frac{H_c}{H_o}$ and $t = \frac{T}{T_c}$ are the reduced critical field and critical temperature, are free from impurity dependent effects. The anisotropy-induced changes in $\bar{H}_o^2$ and $\frac{dh}{dt})_{t=1}$ can be expressed by

$$\frac{\Delta \bar{H}_o(\lambda)}{\bar{H}_o(\lambda)} = \left(\frac{\bar{H}_o(\lambda) - \bar{H}_o(0)}{\bar{H}_o(0)} \right) = \langle a^2 \rangle \delta_H(\lambda)$$

$$\frac{\Delta\left[\frac{dh(t,\lambda)}{dt}\right]_{t=1}}{\left[\frac{dh(t,0)}{dt}\right]_{t=1}} = \left(\frac{\frac{dh(t,\lambda)}{dt} - \frac{dh(t,0)}{dt}}{\frac{dh(t,0)}{dt}} \right)_{t=1}$$

$$= \langle a^2 \rangle \delta_h(t,\lambda)_{t=1} ,$$

where $\delta_h(\lambda)$ and $\delta_h(t,\lambda)$ are mathematical expressions defined in Clem's paper. λ is related to ρ_r by $2\pi\lambda = \alpha^i \Theta \rho_r = \varkappa$ and $\langle a^2 \rangle$ is the mean-squared value of anisotropy in energy gap Δ_k .

(iii) SUPERCOOLING AND KAPPA FACTOR

The dynamical method previously described is well suited to study supercooling. At any temperature below the critical temperature, as the magnetic field is increased, the sample makes the transition from the superconducting to the normal state when $H=H_c$, where H_c is equal to the thermodynamic critical field. As the external magnetic field is decreased from above H_c , the sample undergoes a transition from the normal to the superconducting state at a field $H=H_s$ ($<H_c$), where H_s is the supercooling field. Saint James and De Gennes[56] pointed out that H_s is in fact the surface sheath nucleation field H_{c3} , because when H reaches H_{c3} it becomes possible to create weakly superconducting regions near the surface of the sample with no energy expense[57]. The normal state becomes strictly unstable when $H \leqslant H_{c3}$. The bulk nucleation field $H_{c2} = \frac{1}{1.695} H_{c3}$, and the Landau-Ginsburg parameter κ is defined by:

$$\kappa = \frac{1}{\sqrt{2}} \frac{H_{c2}}{H_c} = \frac{1}{1.695\sqrt{2}} \frac{H_{c3}}{H_c} = 0.42 \frac{H_{c3}}{H_c} = 0.42 \frac{H_s}{H_c}$$

This method of calculating κ is probably not quite correct, because the Landau-Ginsburg equations are valid only for temperatures T such that $(T_c - T) \ll T_c$, while the supercooling fields are measured usually at lower temperatures.

Figures 10 show plots of supercooling field H_s against the critical field H_c. On the lower right corner is an expanded plot for small critical fields, corresponding to temperatures close to T_c . The scales are recorder divisions, so that $\frac{H_s}{H_c}$ is independent of magnetic field

Fig. 10.a
Sample P4

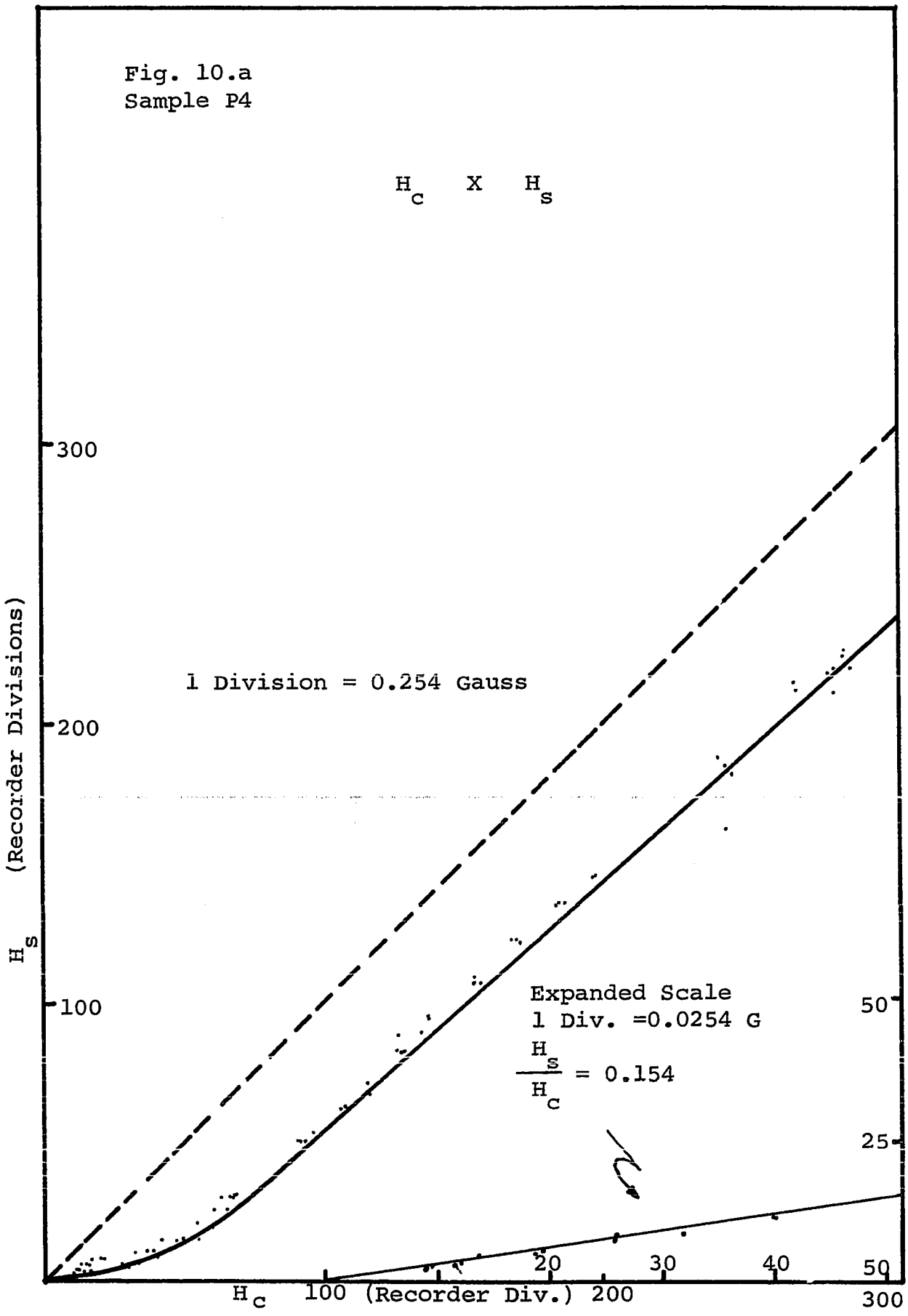

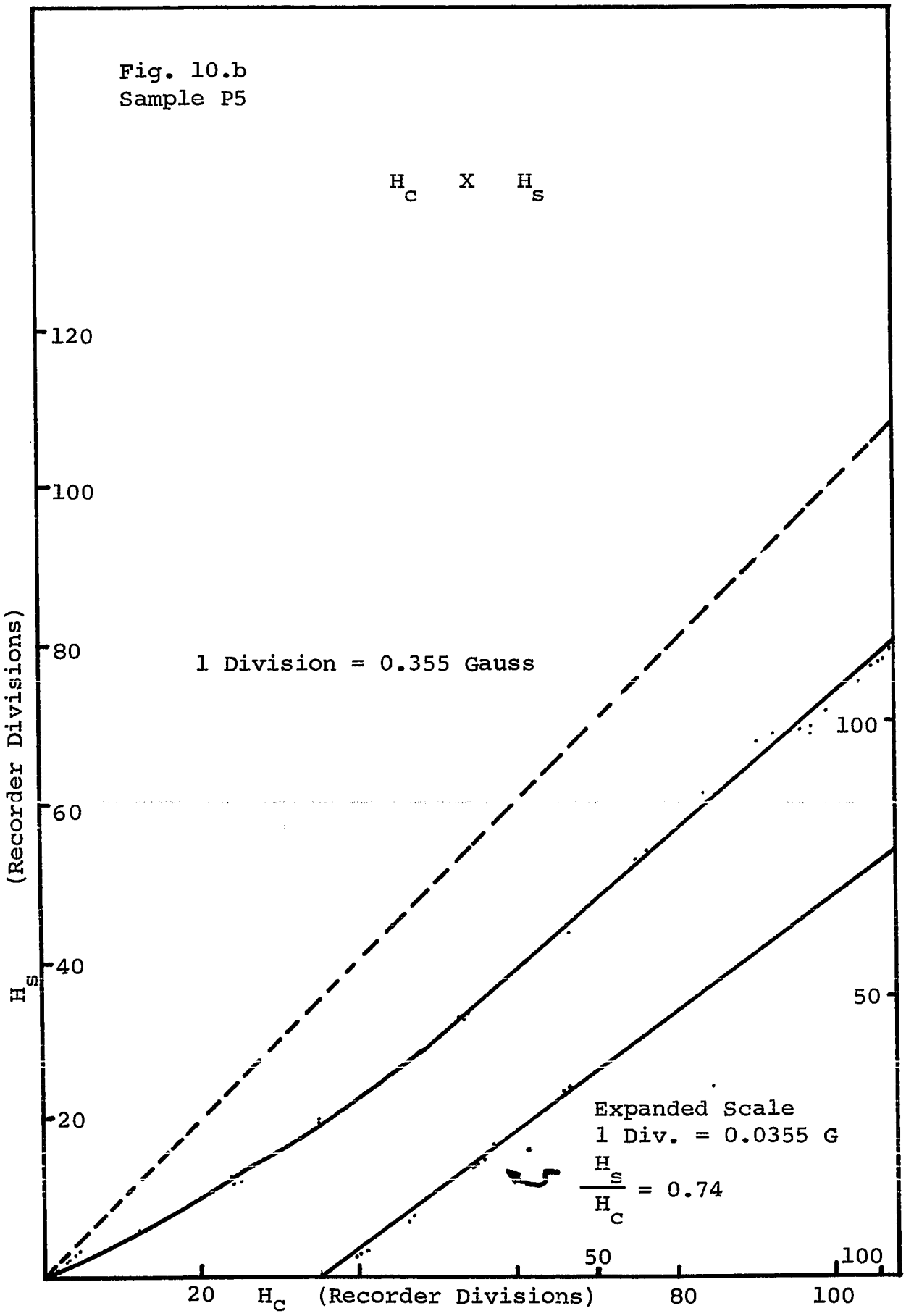
Fig. 10.b
Sample P5
H_c X H_s
120
100
80
60
40
20
H_s (Recorder Divisions)
1 Division = 0.355 Gauss
100
50
Expanded Scale
1 Div. = 0.0355 G
$\frac{H_s}{H_c} = 0.74$
50
100
20
H_c (Recorder Divisions)
80
100

Fig. 10.c
Sample P5H1

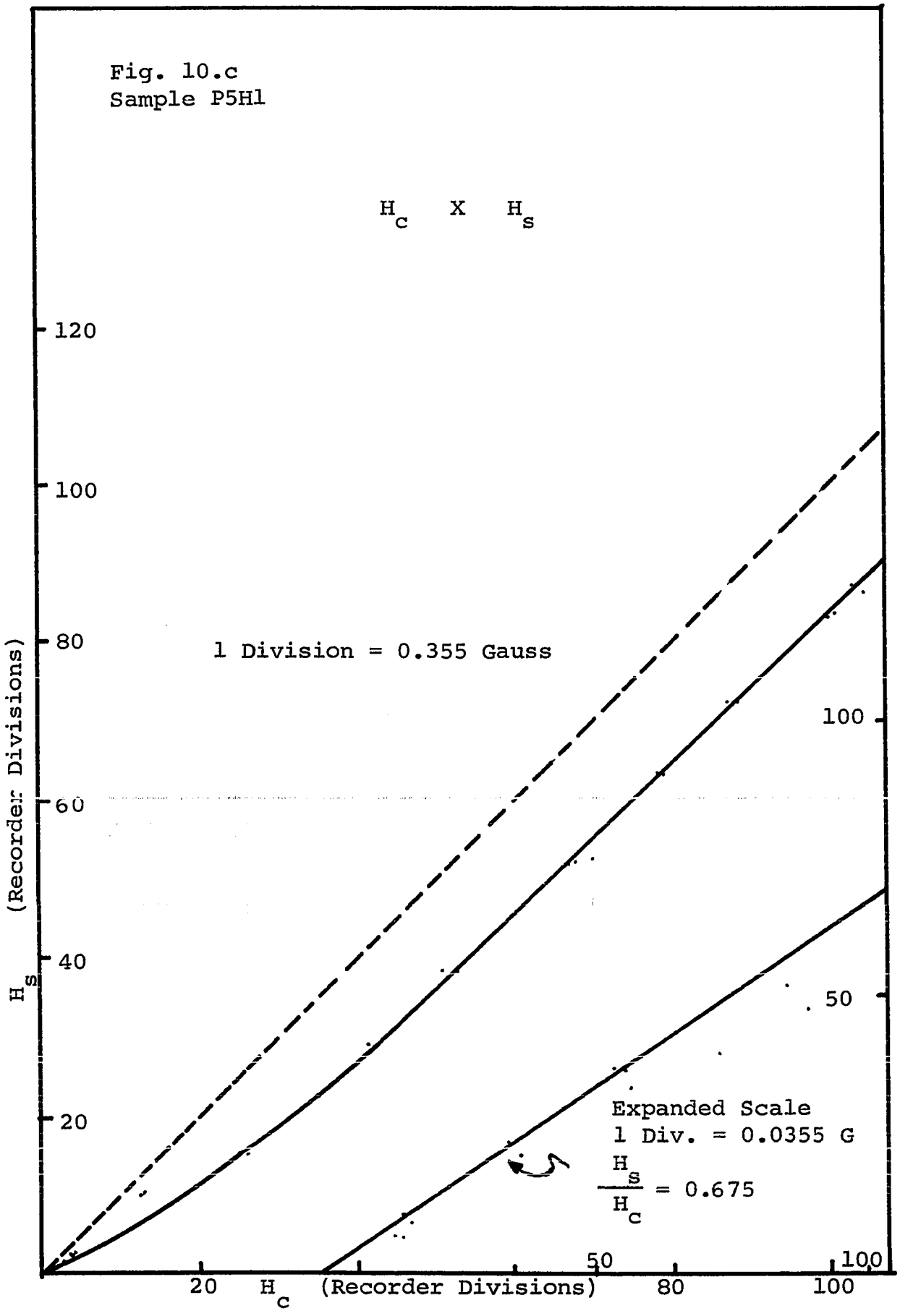

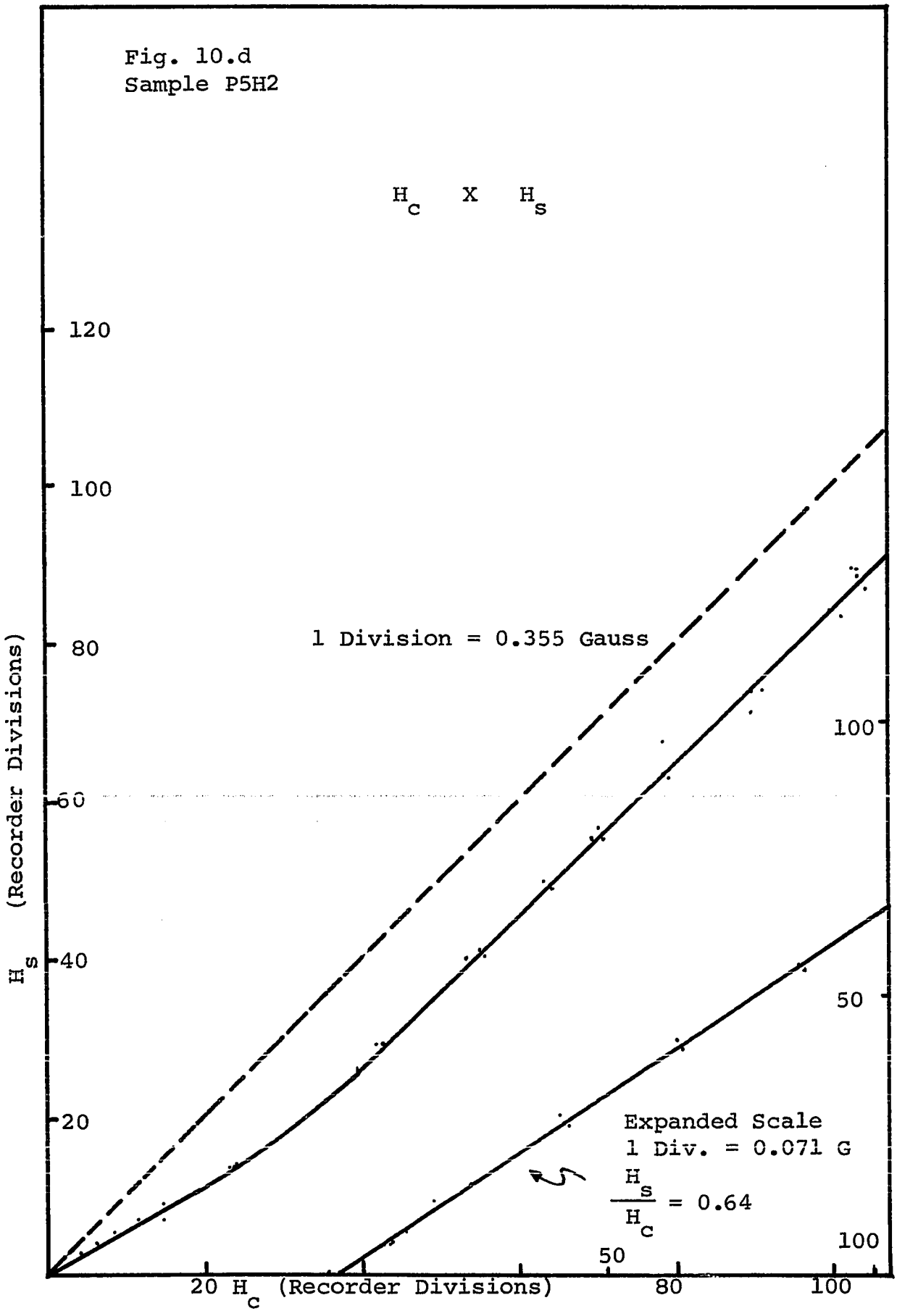
Fig. 10.d
Sample P5H2
H_c X H_s
120
100
80
60
40
20
H_s (Recorder Divisions)
1 Division = 0.355 Gauss
100
50
Expanded Scale
1 Div. = 0.071 G
$\frac{H_s}{H_c}$ = 0.64
100
50
20 H_c (Recorder Divisions)
80
100

calibration or the cancellation of stray magnetic fields. The figures 11 show $\kappa(T)=0.42\ H_s/H_c$ versus T. As mentioned above, in determining κ we have assumed that $H_s=H_{c3}=1.695\ H_{c2}$ holds for all temperatures. Recently Ostenson and Fennemore[58] found that for niobium H_{c3}/H_{c2} falls far below the Saint James-De Gennes factor of 1.695. Ebneth and Tewordt[59], and Luders[60] have found, for temperatures just below the G-L region, a correction term $1.041\ (1-t)$, where $t\equiv T/T_c$, for the ratio H_{c3}/H_{c2} for a sample with a specular surface. Hu and Korenman[61] have shown that the expansion parameter near T_c is $(1-t)^{1/2}$ and the next order term is $-0.978\ (1-t)^{3/2}$. As $T \rightarrow 0$ K, the ratio $H_{c3}/H_{c2} \rightarrow 1.925$ and the slope of dH_{c3}/dH_{c2} versus T vanishes. They have proposed the following interpolation formula for the whole temperature range below T_c :

$$H_{c3}/H_{c2} = 1.695[1+0.614(1-t)-0.577(1-t)^{3/2}-0.007(1-t)^2 +0.106(1-t)^{5/2}]$$

Maloney et. al.[62] have found an anomolous behaviour for H_{c3}/H_{c2} near T_c in Sn-In and In-Bi alloys. They explain their results (for $t \lesssim 0.98$) by a proximity effect which assumes a perturbation that decreases the critical temperature in the surface layer. For temperatures closer to T_c their results still remain unexplained. H_{c3}/H_{c2}, for thick samples, reaches a minimum at t=0.99 and at higher temperatures has a tendency to increase. The linear increase of the H_{c3}/H_{c2} ratio from 1.695 at T_c to 1.925 at 0 K can not explain the maxima we observe in $\kappa(T)$ just below the critical temperature T_c. Large amounts of hydrogen absorbed on the surface are probably responsible for this behaviour.

Fig. 11.a
Sample P4

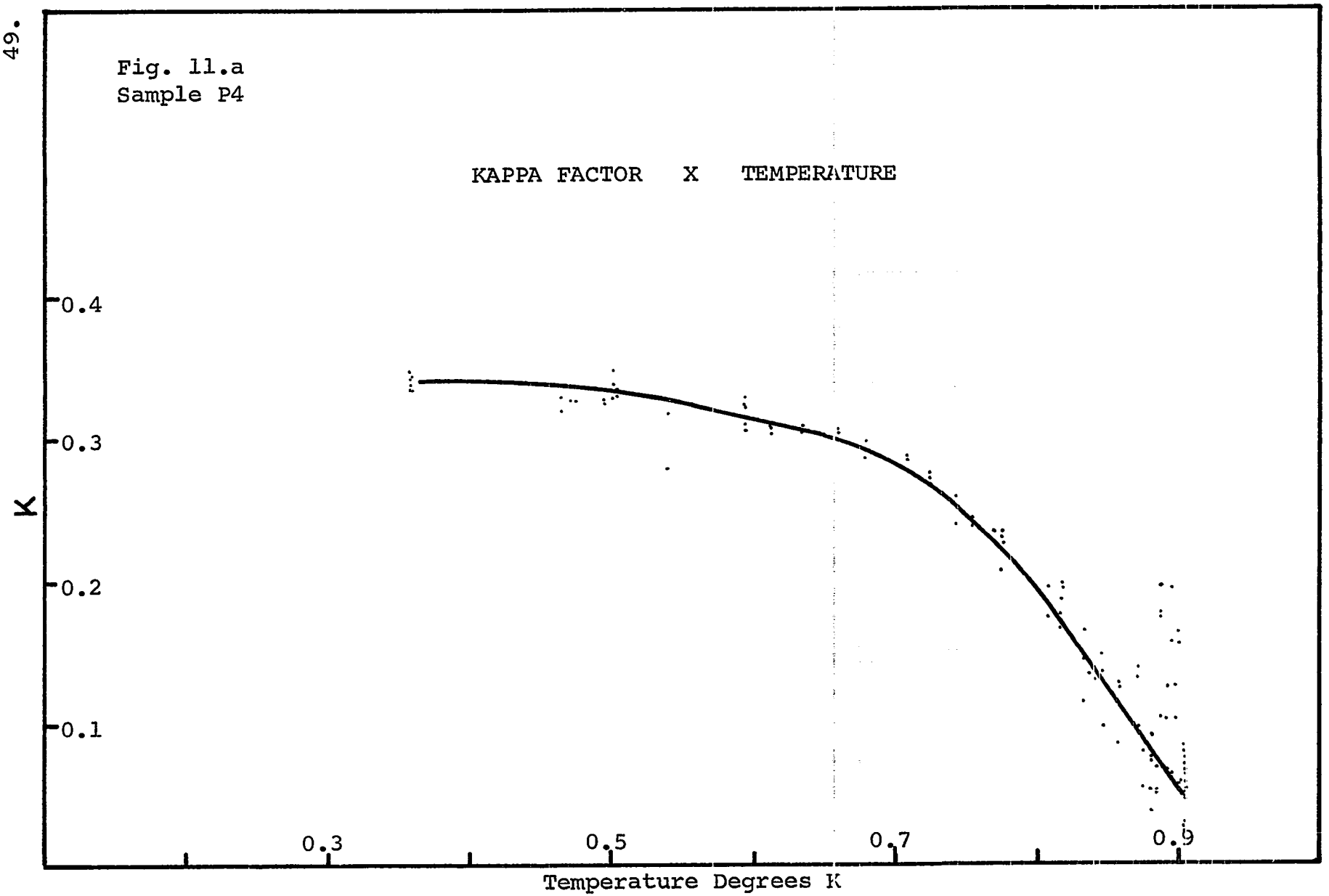

Fig. 11.b
Sample P5

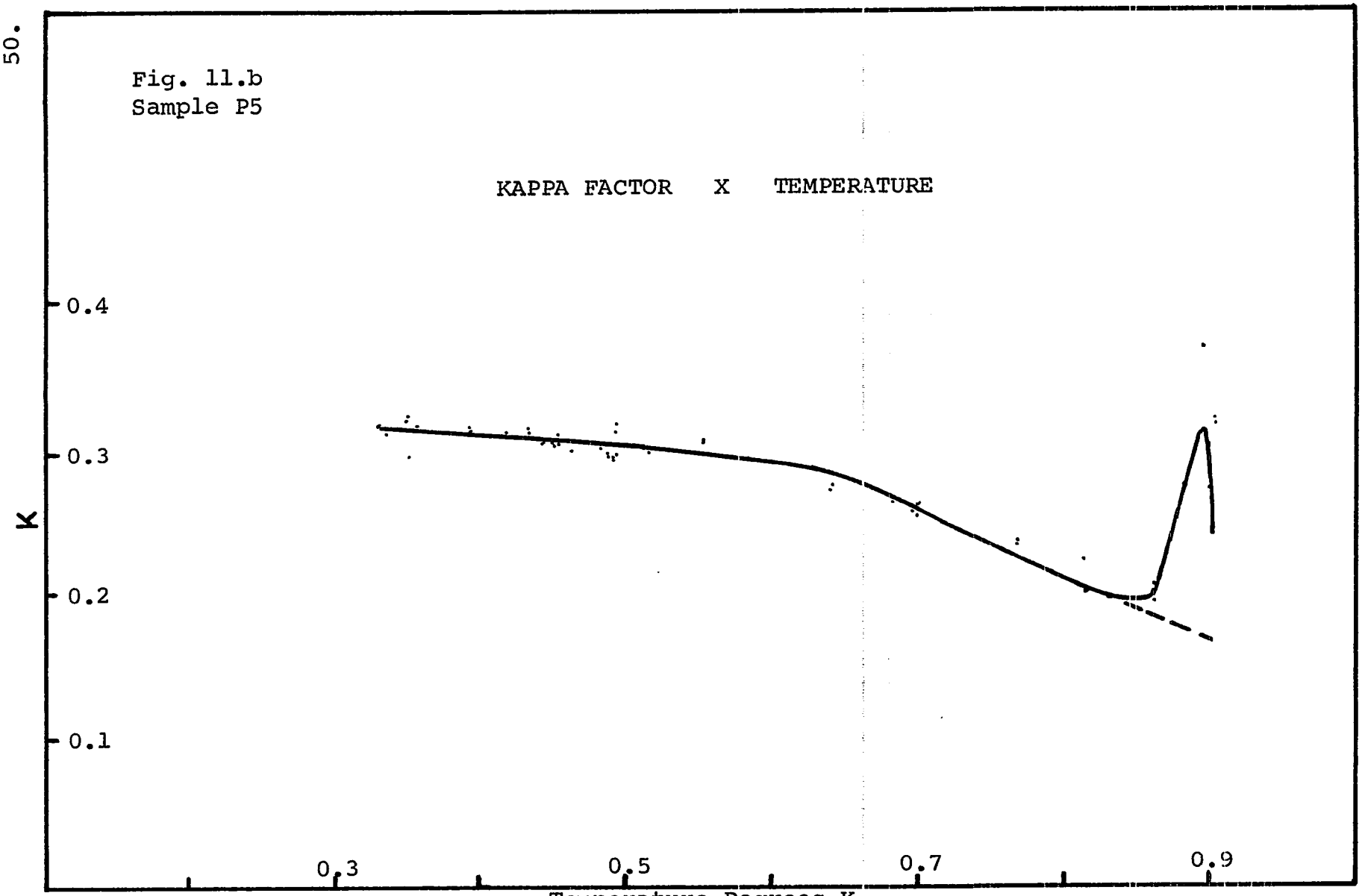

Fig. 11.c
Sample P5H1

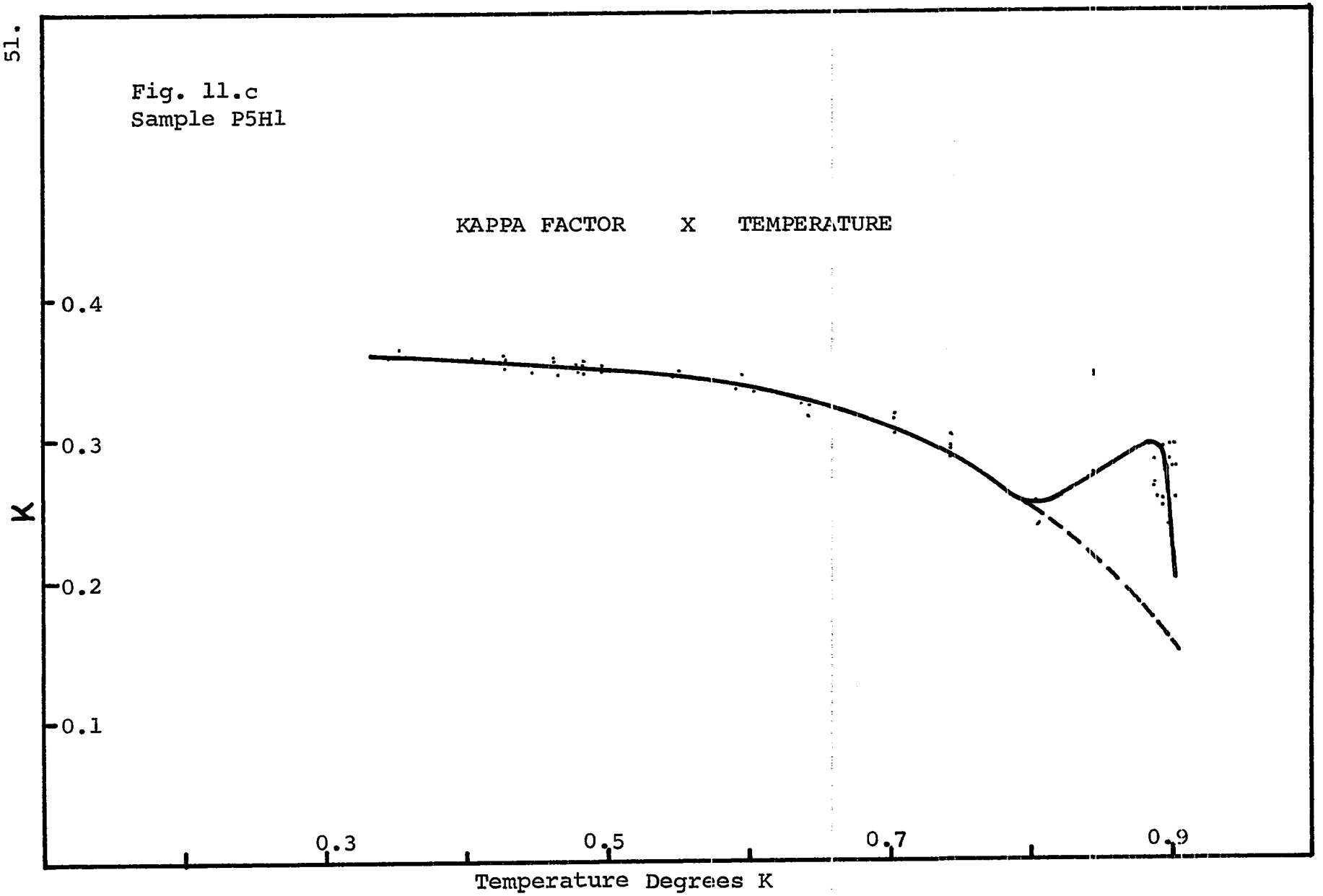

Fig. 11.d
Sample P5H2

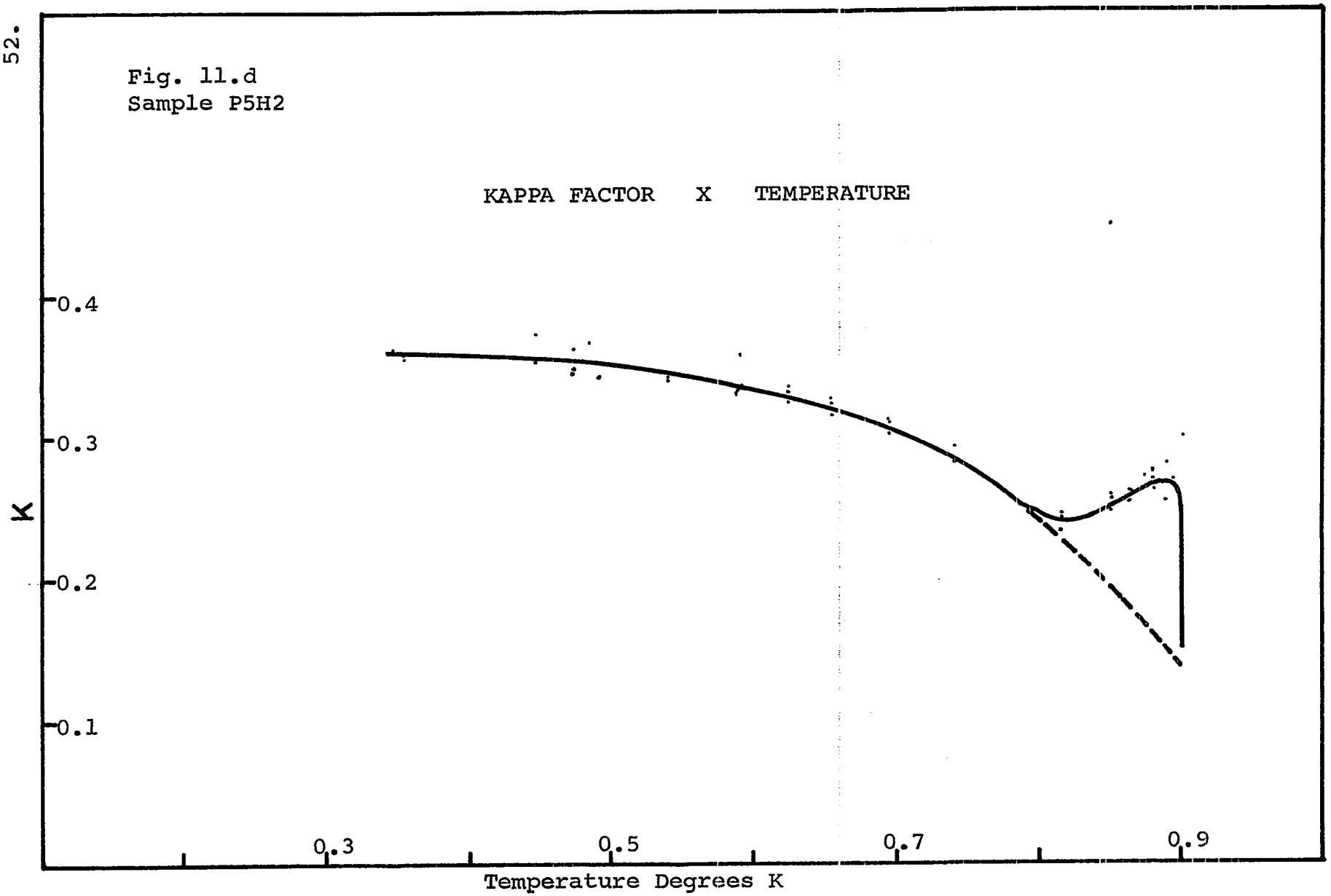

For pure material (infinite mean-free-path), the Kappa factor is determined by T_c, γ and S, the area of the Fermi surface in k-space. Goodman[63] has given expressions for the London penetration depth at absolute zero:

$\lambda_L(0) = \frac{3h}{ekS}\pi^{1/2}\gamma^{1/2}$, and the coherence length for a pure material at absolute zero : $\xi_o = \frac{0.18\ k\ S}{12\pi\gamma T_c}$. Thus

$$K_o(T=T_c) = 0.96\ \frac{\lambda_L(0)}{\xi_o} = \frac{192\pi^{3/2}h}{ek^2}\ \frac{T_c\gamma^{3/2}}{S^2}$$

In an alloy such as molybdenum-hydrogen, the penetration depth, coherence length and Kappa factor are strongly influenced by the mean-free-path l which can be determined from the normal state resistivity $\rho_n = \frac{6\pi^2 h}{e^2 S \langle l \rangle}$.

In the limit of $l \ll \xi_o$ as l decreases, λ increases as $\lambda_L(\frac{\xi_o}{l})$, ξ decreases as $(\xi_o l)^{1/2}$ and K increases as λ_L^{-1} or as $\gamma^{1/2}\rho_n$ [48,64-66].

Goodman[67] has shown that Gorkov's calculation of the general dependence of K on l can be approximated by the simple formula $K = K_o + 7.5\ 10^{-3}\ \gamma^{1/2}\rho_n$ where γ is in Erg. $cm.^{-3}$ $deg.^{-1}$ and ρ_n is in micro-ohm-cm. K_o is the Kappa value for the pure material.

C. MECHANICAL PARAMETERS

(i) HARDNESS

Figure 12 shows a plot of Knoop Hardness Number (KHN) as a function of hydrogen dissolved in ppm by weight. Small amounts of hydrogen (as little as 0.33 ppm) cause about 20 % softening. This may be due to reduced lattice strains in the molybdenum crystal caused by interstitial hydrogen atoms. Such a conclusion however runs against geometrical considerations. molybdenum crystallises as a body centered cubic crystal. Hume-Rothery and Raynor[68] have pointed out that in bcc structure the octahedral holes, being extremely distorted, can only contain spheres of radius not greater than .154 times that of the solvent atoms. The symmetrical holes in the bcc structure are of the tetrahedral type, and their size is such that they can only accomodate spheres with radius not more than 0.291 times that of the solvent atoms.

For molybdenum, the closest distance of approach, which can be taken as the atom diameter for this structure, is 2.72 A^{o} and the size of the tetrahedral interstices (0.291 times the atom diameter) is 0.79 A^{o}. The diameter of the hydrogen atom is usually taken to be of the order of 1.05 A^{o} which is considerably larger than the tetrahedral interstices. This would therefore suggest that hydrogen atoms in tetrahedral holes of an otherwise perfect bcc lattice will cause considerable internal strain. The absence of strains would therefore lead to the conclusion that hydrogen atoms in molybdenum are ionised. The proton, of

Fig. 12

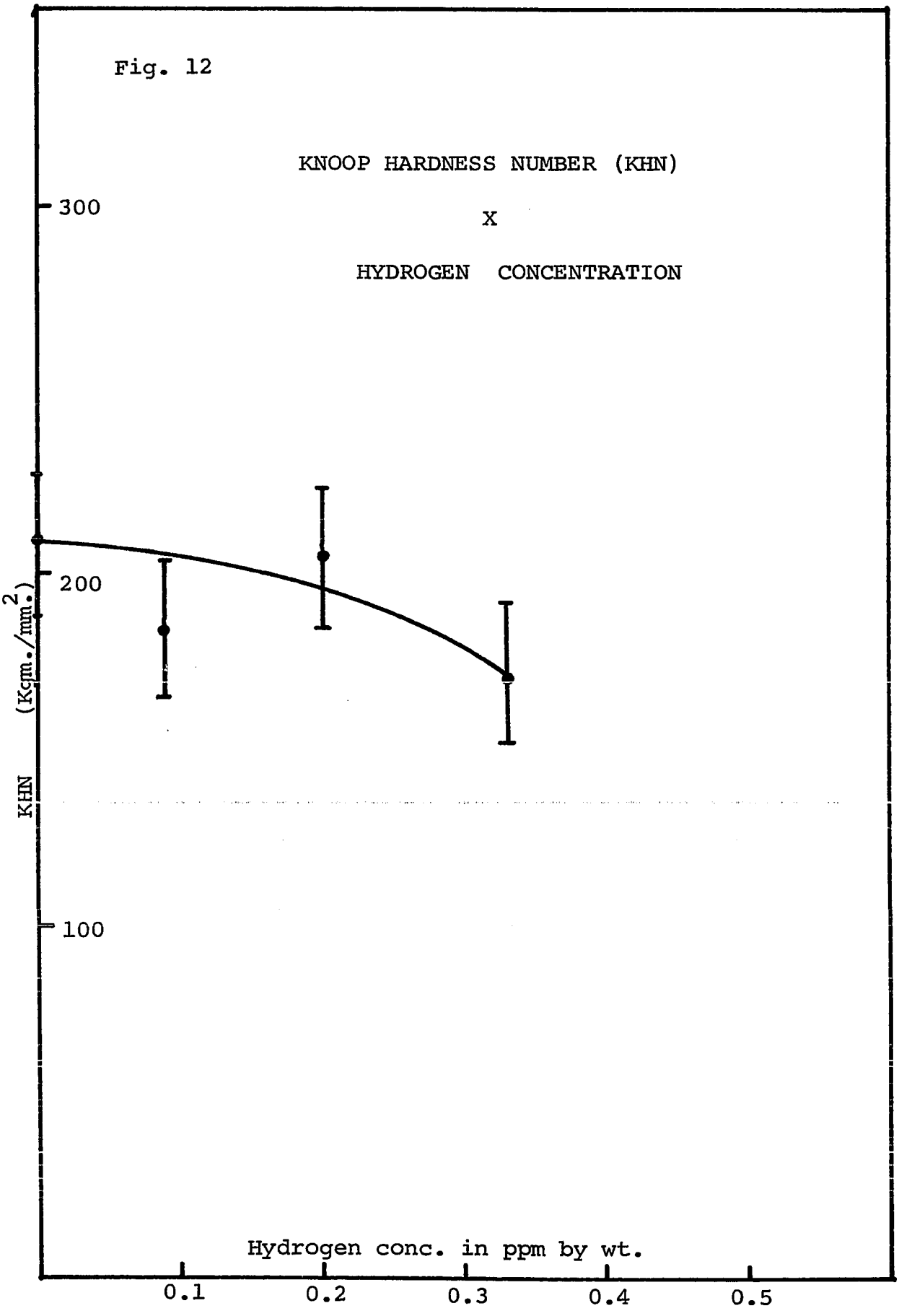
KNOOP HARDNESS NUMBER (KHN)
X
HYDROGEN CONCENTRATION
300
200
100
KHN (Kgm./mm.^{2})
Hydrogen conc. in ppm by wt.
0.1
0.2
0.3
0.4
0.5

negligible size, stays in the interstitial hole, and the free electron may contribute to the electrical properties such as the conductivity etc.

(ii) TENSILE STRENGTH AND FRACTURE

Tensile tests performed at liquid nitrogen temperature on a part of sample P5H2 and a "test piece" representative of P5 yielded fracture stresses of 23.71 Kgm. /mm.^{2} and 12.95 Kgm. /mm.^{2} at a strain rate of 50.8 mm. /min. Both samples, with and without hydrogen, underwent brittle fracture.

To study the effect of hydrogen solution on mechanical properties of molybdenum at room temperature, four samples identified as Mo X-54-1, Mo X-54-3, Mo X-54-4, and Mo X-54-5 were annealed at 1100^{o}C (10^{-6}mm. Hg) for 7 Hours. Subsequently Mo X-54-4 and Mo X-54-5 were exposed with hydrogen at 1250^{o}C for five minutes each and quenched in ethyl alcohol. The concentration of hydrogen dissolved was approximately 1 ppm by weight (48 atomic ppm).

Figures 13 show load as a function of plastic elongation for all these samples. These curves represent stress-strain curves obtained on an Instron machine, beyond the linear elastic limit.

The results of these tensile tests are collected in Table III . The elastic modulus E is estimated from the initial linear portion of the stress-strain curve. The slope of the curve just below the elastic limit was used to avoid uncertainties due to streching of the parts of the set up other than the sample. The yield strength is measured by the stress at the point where the stress-strain curve deviates from linear behaviour. Ultimate Tensile Strength (UTS) is the magnitude of stress at the onset of necking. Fracture load is the load value at fracture. The activation volume ΔV is defined such that $\Delta V.\tau$ is the total work

done by external forces during the dislocation activation event. The strain rate $\dot{\varepsilon}$ produced by an applied shear stress τ depends on temperature T and Gibbs free energy of activation ΔG as[69]

$$\dot{\varepsilon} = NAb\,\nu\,\mathrm{Exp.}(-\Delta G/kT)$$

where N is the number of points per unit volume where glide dislocations are held up by local obstacles, A is the area swept by a segment released when an obstacle is surmounted and ν is the "attempt frequency" of this segment. The equation above can be rewritten as

$$\dot{\varepsilon} = B\,\mathrm{Exp.}(\Delta S/k)\,\mathrm{Exp.}[-(\Delta U - \tau\Delta V)/kT]$$

where $B=NAb\nu$ is a "structure factor".

Since ΔG is a perfect differential we can determine ΔV from differential experiments

$$\Delta V = -\left(\frac{\partial \Delta G}{\partial \tau}\right)_T = kT\left(\frac{\partial \ln\dot{\varepsilon}}{\partial \tau}\right)_{B,T}$$

$$= kT\left(\frac{\ln\dot{\varepsilon}_2 - \ln\dot{\varepsilon}_1}{\tau_2 - \tau_1}\right) = kT\ln(\dot{\varepsilon}_2/\dot{\varepsilon}_1)\frac{1}{\Delta\tau}$$

$$\Delta V = kT\ln(\dot{\varepsilon}_2/\dot{\varepsilon}_1)\quad\frac{1}{(\Delta L/a)}$$

Thus knowing the strain rates $\dot{\varepsilon}_2$ and $\dot{\varepsilon}_1$ and the corresponding change in load ΔL and cross sectional area a, ΔV, the activation volume, which is a measure of the resistance to dislocation movement, can be found. The activation volume decreases as the plastic strain increases for all samples. Similar behaviour was observed by Youngblood[74] for pure molybdenum single crystals.

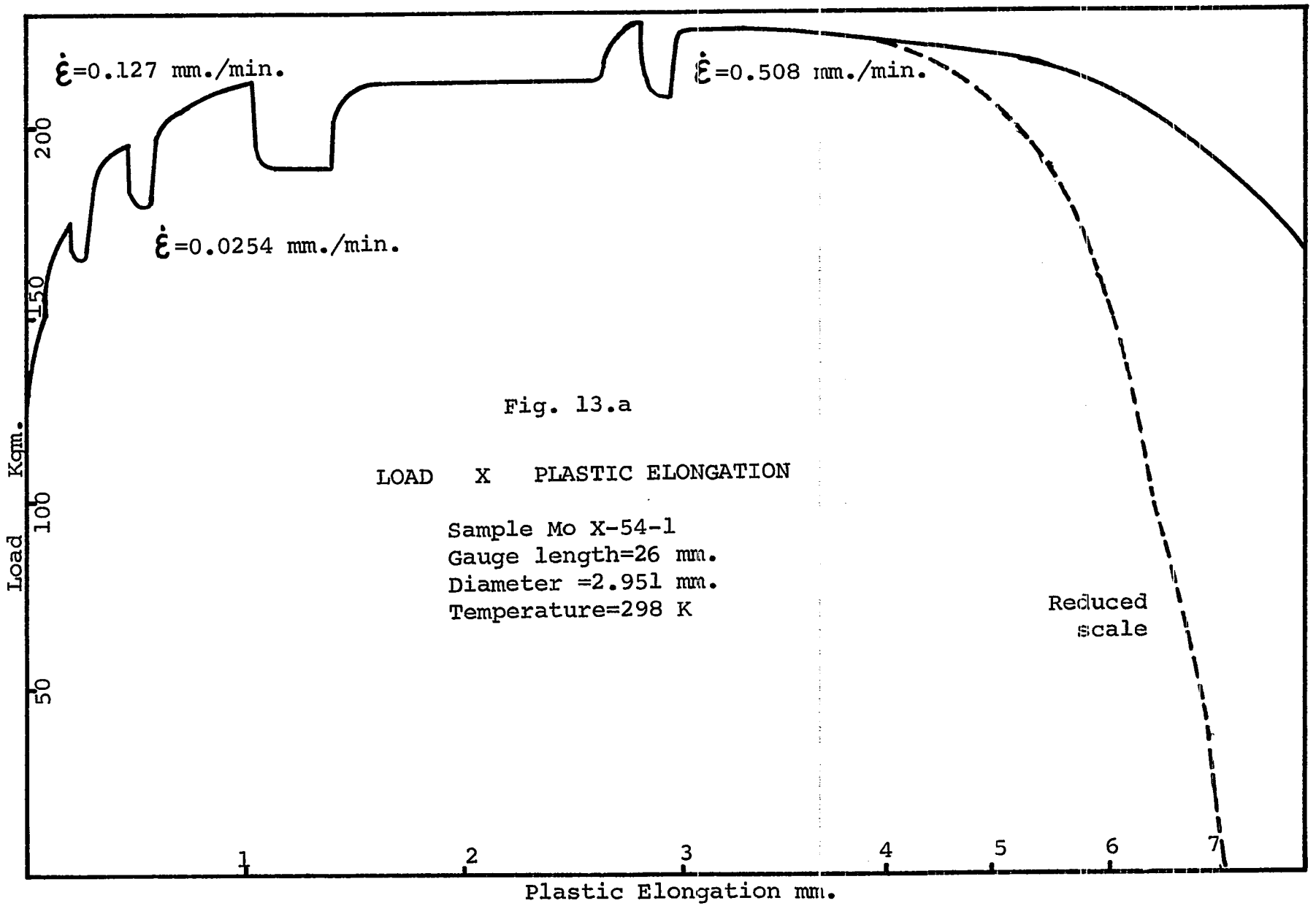

Fig. 13.a

LOAD X PLASTIC ELONGATION

Sample Mo X-54-1
Gauge length=26 mm.
Diameter =2.951 mm.
Temperature=298 K

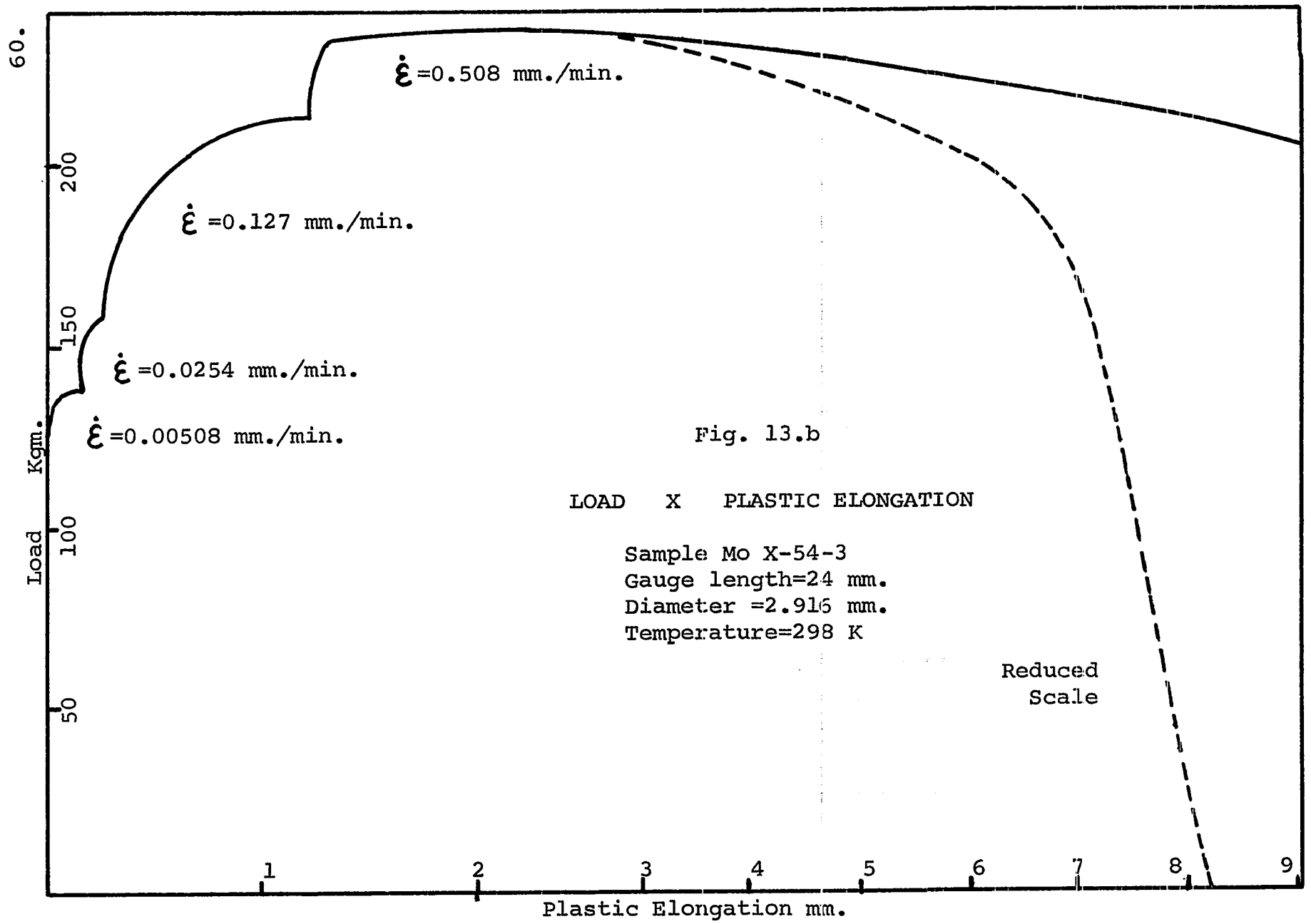

Fig. 13.b

LOAD X PLASTIC ELONGATION

Sample Mo X-54-3
Gauge length=24 mm.
Diameter =2.916 mm.
Temperature=298 K

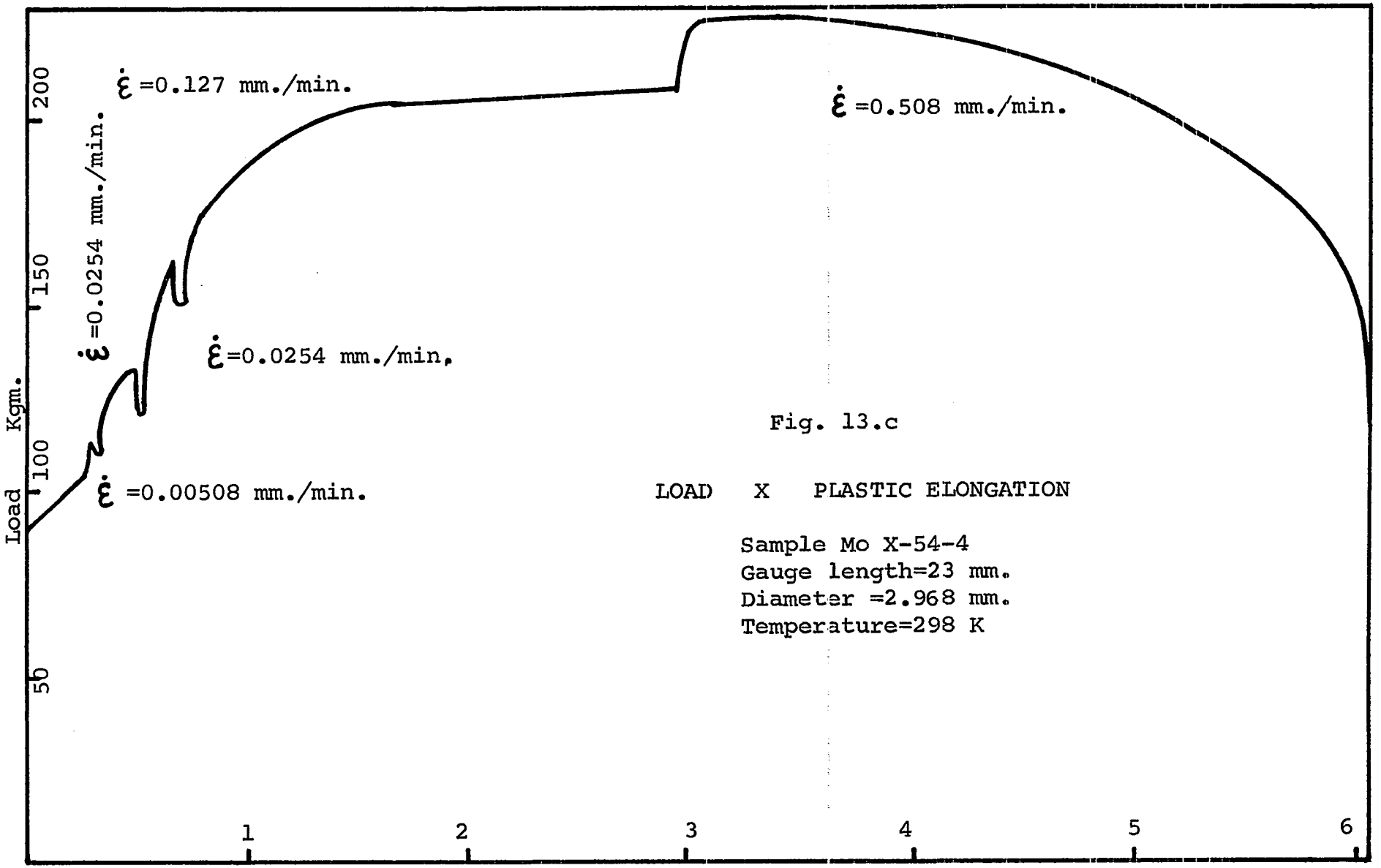

Fig. 13.c

LOAD X PLASTIC ELONGATION

Sample Mo X-54-4
Gauge length=23 mm.
Diameter =2.968 mm.
Temperature=298 K

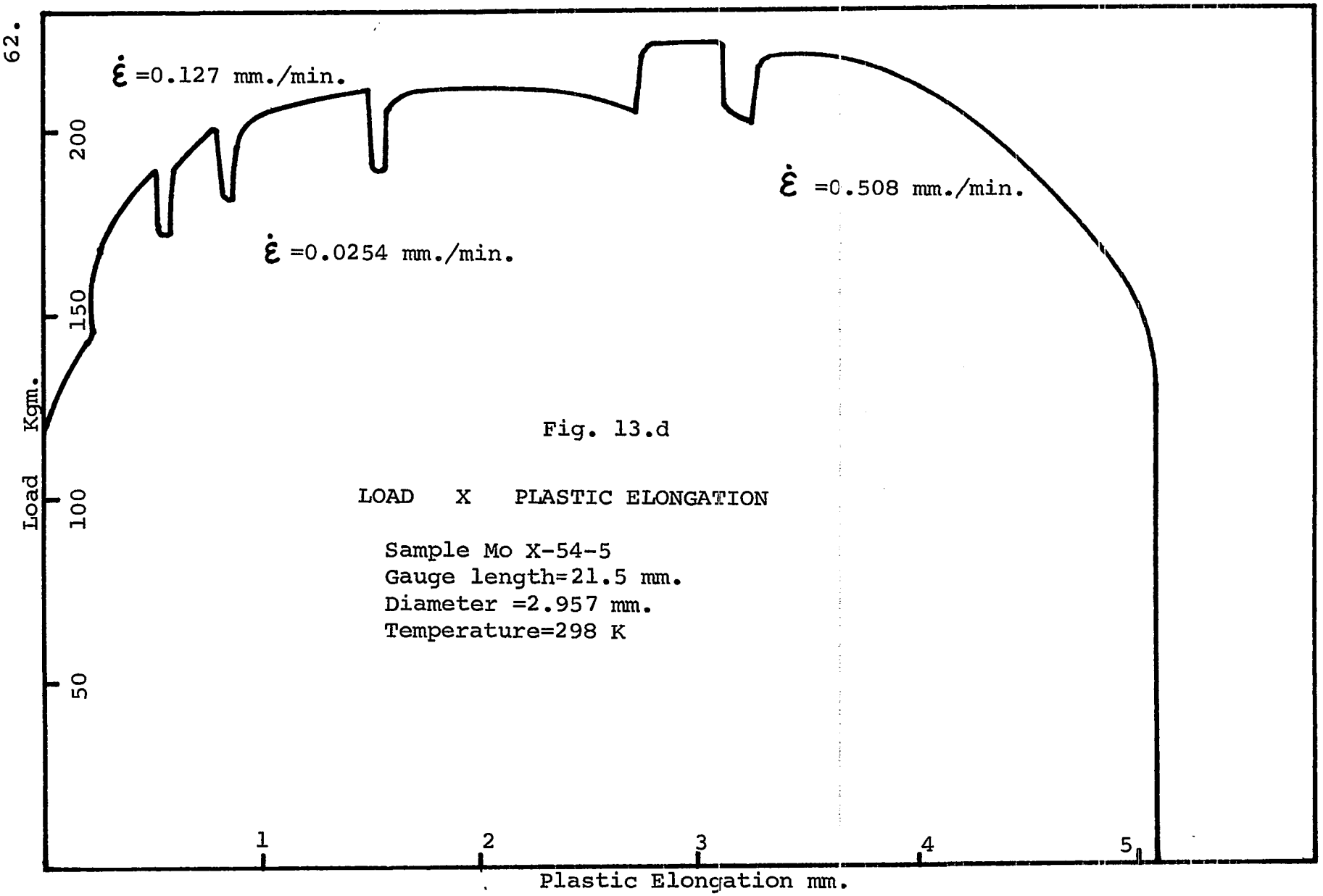

Fig. 13.d

LOAD X PLASTIC ELONGATION

Sample Mo X-54-5
Gauge length=21.5 mm.
Diameter =2.957 mm.
Temperature=298 K

TABLE III

Results of mechanical measurements

Sample	Description	Hardness KHN ± 20	Modulus of Elasticity Kgm./mm.^{2}	Yield Strength Kgm./mm.^{2}	UTS Kgm./mm.^{2}	% Reduction in area	Load at Fracture Kgm.
P5	Tensile tested at 77.3 K	209			12.95		
P5H1		205					
P5H2	Tensile tested at 77.3 K	171			23.711		
Mo X-54-1	Anneal 7 Hrs. at 1373 K Tested 298 K		$1.33\ 10^4$	18.56	33.04	97.47	0
Mo X-54-3	Same as above		$1.94\ 10^4$	16.98	35.36	98.47	0
Mo X-54-4	Anneal 7 Hrs. at 1373 K H_2 diffused at 1523 K for 5 Min. H_2 conc. 1 ppm wt. Tested 298 K		$1.62\ 10^4$	12.87	32.90	44.61	131.54
Mo X-54-5	Same as above		$1.66\ 10^4$	14.62	32.83	47.36	131.54

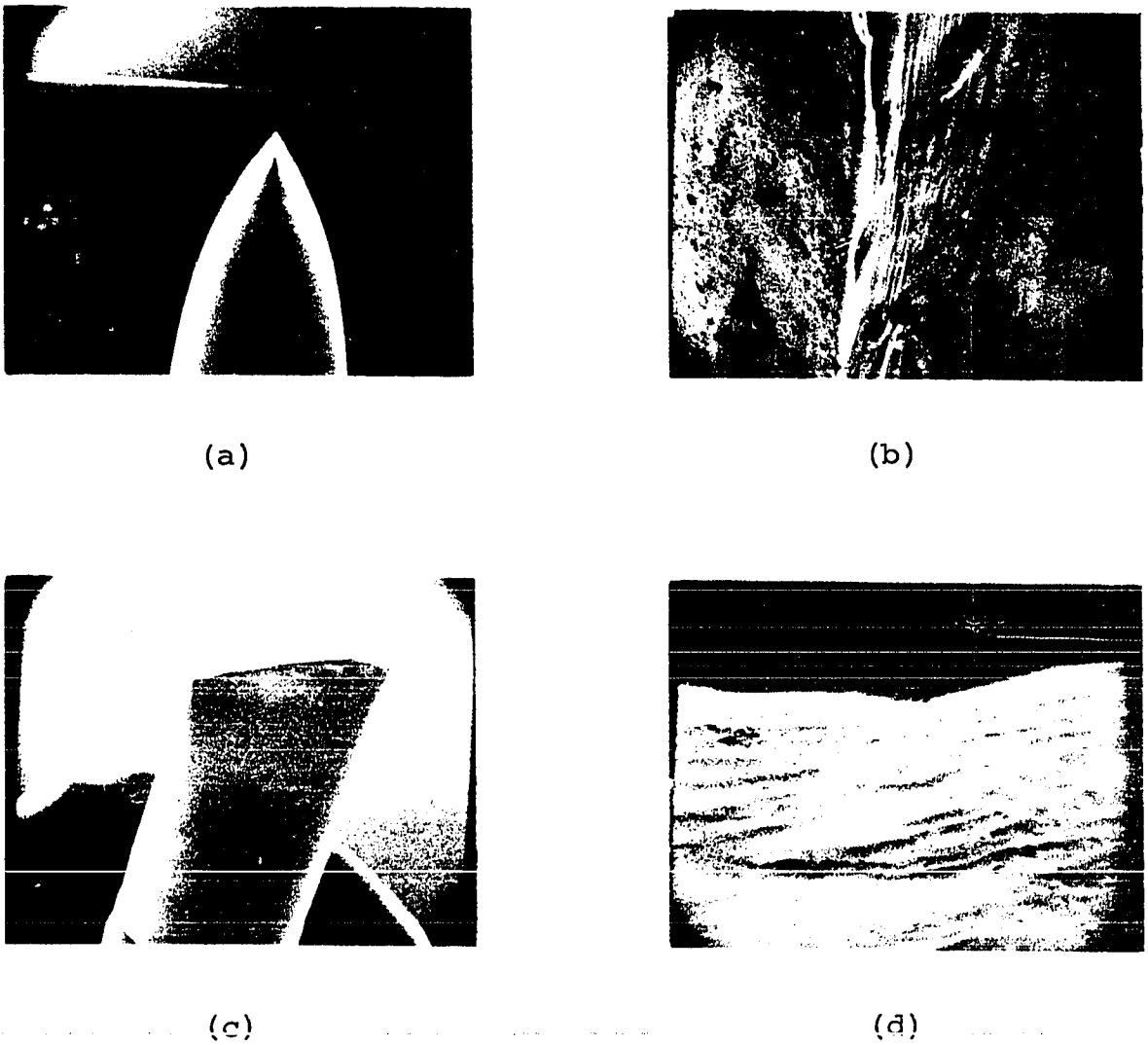

Fig. 14. Scanning electron micrographs of Molybdenum sample Mo X-54-3 after ductile fracture (98.5 % reduction in cross section) , (a) Side view, 18X ; (b) Top view, 900X ; (c) Front view, 18X and (d) Front view magnified, 960X.

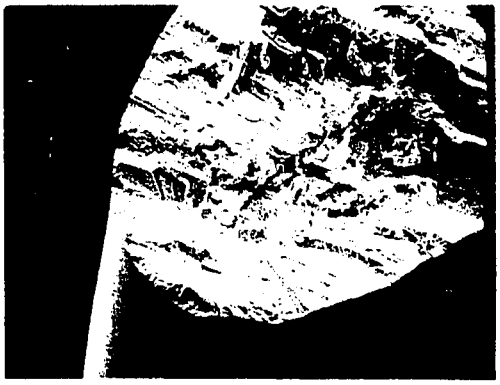

(a)

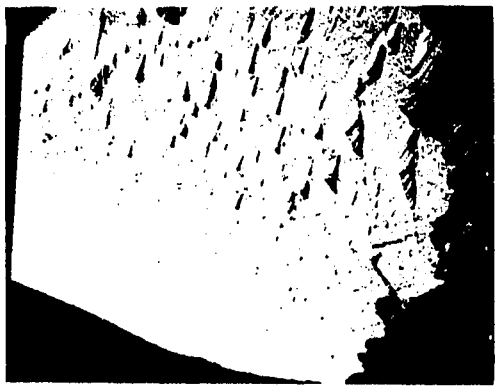

(b)

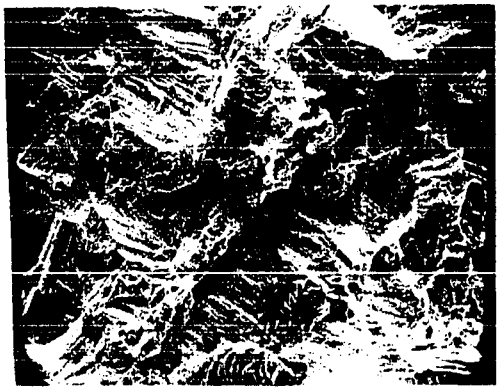

(c)

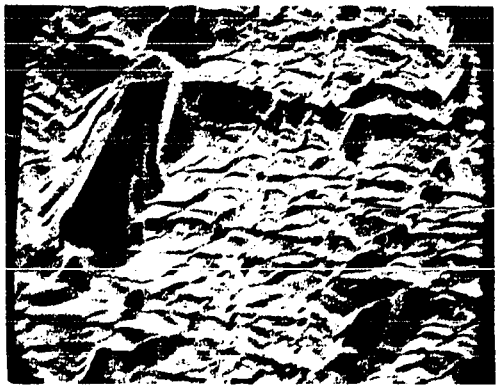

(d)

Fig. 15. Scanning electron micrographs of Molybdenum sample Mo X-54-4 (dissolved hydrogen 1 ppm by weight) after brittle fracture (44.6 % reduction in cross section), (a) Fractured surface and side cracks, 50X ; (b) Side cracks magnified, 430X ; (c) Fractured surface magnified, 200X and (d) Side cracks highly magnified, 4300X.

The only substantial change that occurs when hydrogen is added to molybdenum is in the fracture load and the mode of fracture. Figure 14 shows scanning electron micrographs of the sample Mo X-54-3 after fracture as representative of pure molybdenum. Figure 15 shows similar pictures of sample Mo X-54-4 , representative of the molybdenum with dissolved hydrogen (1 ppm by weight). Without hydrogen, fracture occurs at zero load, and the sample necks down to a chisel edge with a reduction in cross sectional area of almost 100 % . The samples with dissolved hydrogen undergo a reduction in cross section of about 45 % , and the load at fracture is 290 lbs. (131.54 Kgm.). The sample with hydrogen undergoes brittle fracture and has a whole series of cracks near the fracture surface, while the sample free of hydrogen has no noticeable cracks but has a host of slip lines almost parallel to the axis near the fracture tip.

IV. DISCUSSION AND CONCLUSIONS

Our measurements have revealed that the role of hydrogen in "Hydrogen Embrittlement" becomes visible in the mechanical measurements only after necking has started. There are no lattice strains associated with the dissolved hydrogen that can be detected with either the superconducting or mechanical tests performed. Hydrogen in molybdenum is uniformly distributed as an ionised interstitial. It contributes its electron to the conduction band but, because of the extremely low solubility, the change in electron concentration of the metal is negligible. However, impurity scattering does reduce the electron-mean-free-path causing increased resistivity, decreased coherence length and increased penetration depth, as expected. But the increase in slope $\left(\frac{dH_c}{dT}\right)_{T_c}$ on hydrogen solution, leading to an increase in γ and N(0) is quiet unexpected and unexplained.

For interstitial solid solutions of hydrogen in molybdenum, since the lattice parameter of molybdenum does not change on the addition of hydrogen, it is difficult to understand what causes an increase in N(0). The increase in N(0) should also be reflected in T_c. Since

$$\frac{\Delta T_c}{T_c} = \frac{\Delta N(0)}{N(0)} \quad \frac{1}{N(0)\ V} \quad .$$

Nevertheless no increase in T_c is observed.

According to BCS theory,

$$T_c = 1.14\ \hbar\omega\ \text{Exp.}\left[- \frac{1}{N(0)\ V} \right]$$

The impurity-induced changes in T_c could arise

from changes in the phonon spectrum, the electron-electron coupling constant or electron density of states. For the hydrogen-molybdenum alloy it appears that the lowering of T_c expected because of the removal of the anisotropy in the energy gap is compensated by the increase due to changes in N(0), ω and V.

Gayley et. al.[70] have studied the influence of alloying on ω . They find a lowering of the Debye temperature (for long wavelength phonons) on alloying. Pippard[71] has considered the effect of decreased mean-free-path on V, and concluded that V should decrease for longitudinal phonons for an isotropic metal and V should increase for transverse phonons.

Ginsberg[50] considers V as a sum of V_p , the contribution due to electron coupling via phonons, and V_c , the coupling via the coulomb interaction which is unaffected by the electron mean-free-path.

$$\therefore \quad \frac{\delta T_c}{T_c} = \frac{\delta \omega}{\omega} + \frac{1}{N(0)\ V} \frac{\delta V_p}{V_p + V_c}$$

N(0) V can be calculated from the BCS expression using T_c =0.91 K and Θ_D = 460 K.

The result is : N(0) V =0.1649

For Tin, Garland[72] has calculated $\frac{V_p}{V_c}$ =-3.9.

Using this result, and assuming the free electron approximation, Ginsberg has shown that for Tin

$$\frac{\delta T_c}{T_c} = \frac{\delta \omega}{\omega} + 0.33\ \delta \rho$$

where ρ is the change in resistivity. Unfortunately for molybdenum $\frac{V_p}{V_c}$ is not known, and the free electron

approximation is not valid[73] so we cannot calculate $\frac{\delta T_c}{T_c}$.

Our sample P4, which is well-annealed, has too small a value of $\frac{dH_c}{dT})_{T_c}$, which gives a value for from the BCS theory which is too small compared to the values reported in the literature for pure molybdenum[45]. Hence our density of states is too low, and using Θ_D=460 K we get too large a value for the electron-electron interaction parameter V. On hydrogen diffusion, however, the values of these parameters approach those reported for pure molybdenum.

In Fig. 16 we plot the function $D(t)=h-(1-t^2)$ where $h=\frac{H_c}{H_c(0)}$, $t=\frac{T}{T_c}$, as a function of t^2. Here again we find, the deviation from the BCS weak-coupling limit is maximum for P4 and minimum for P5H2. From these results it seems that dissolved hydrogen, by removing anisotropy in the energy gap, improves the agreement with the BCS weak coupling limit, since in BCS theory an isotropic energy gap is assumed. This, however, could also be accidental, since in calculating D(t) we use the value of H(0) obtained by extrapolating H_c versus $(T/T_c)^2$ plot to T=0 K. And because our H_c measurements do not extend to temperatures close enough to 0 K ($T/T_c \gtrsim 0.345$), this extrapolation is doubtful. Small changes in H(0) can have a strong influence on the agreement with the BCS weak-coupling limit. To settle the question, H_c values at lower temperatures should be measured.

As pointed out above, the role of hydrogen in causing brittle fracture begins after necking has started. At this stage the sample is deformed and is obviously inhomogenous. All our superconducting measurements have been done on homoge-

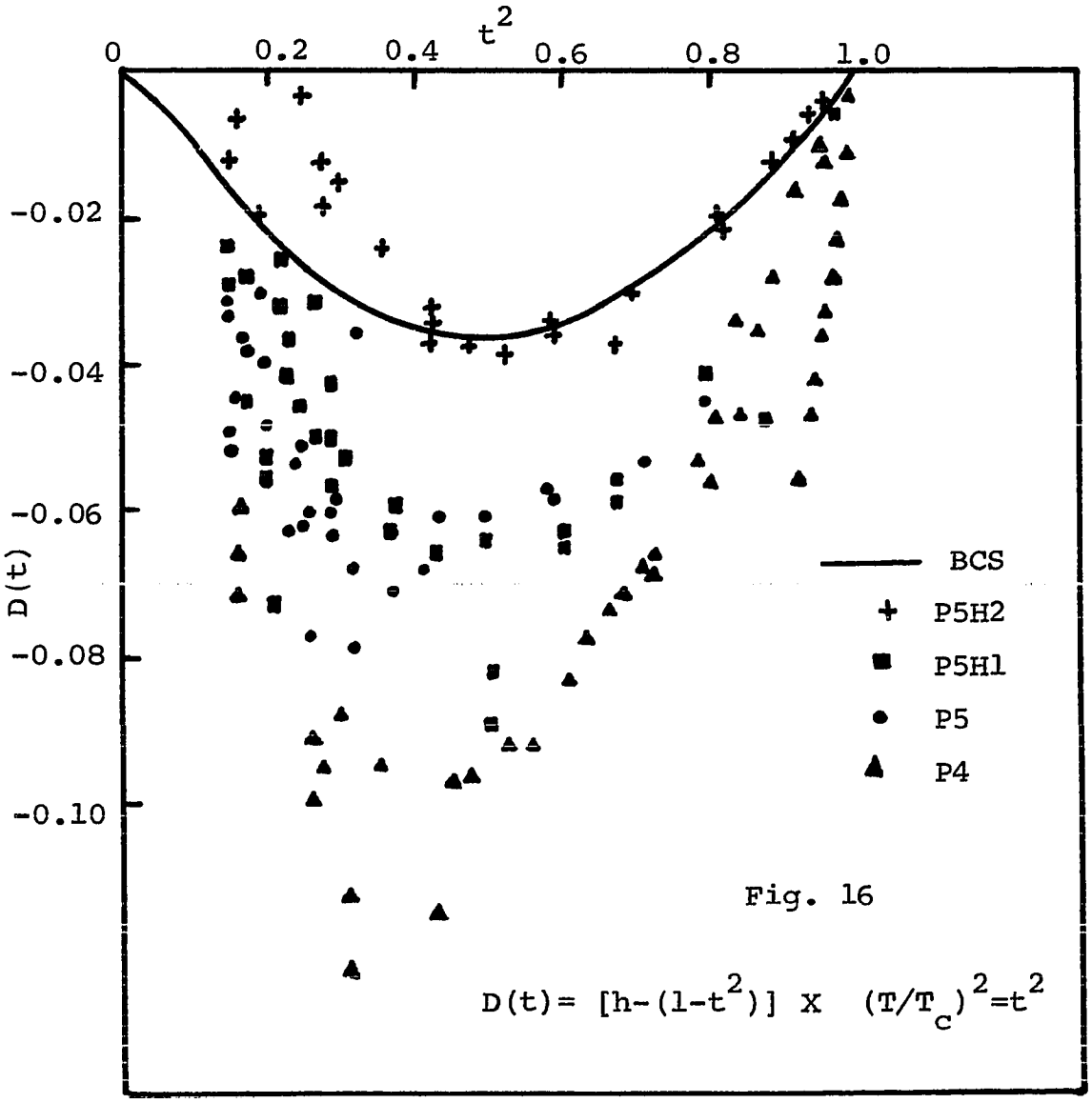

Fig. 16

$D(t) = [h-(1-t^2)] \times (T/T_c)^2 = t^2$

neous samples. So it is difficult to correlate our superconducting measurements with the role of hydrogen in the "Embrittlement" effect. The specific role of hydrogen seems to be either to help nucleate a crack or to aid the rapid propagation of existing microcracks. A rough count of the cracks on the sample with dissolved hydrogen yielded about $10^8 - 10^9$ cracks per $cm.^2$

The data we have obtained in this investigation is certainly not enough to guide us in choosing any out of the existing theories of "Hydrogen Embrittlement", much less suggest any new one. To understand this interesting phenomenon we need information about the location and the dynamics of hydrogen during plastic deformation. Superconducting measurements after various amounts of plastic deformation may give the desired information.

Superconducting measurements on a number of metals with dissolved hydrogen can give interesting clues about the electronic and geometrical factors which limit the solubilities of gases in metals.

For transition metal alloys Chao et. al.[17] have shown that electronic interactions dominate the changes of system free energy as the interstitials are formed from the atomic state to the ionised state during the dissolving process. They use a rigid band approximation and the band structure calculations of Matheiss. The exact quantum-mechanical solution of the screening problem considering the changes in local energy band structure and electronic wavefunction caused by the presence of interstitials is very involved. Our attempts in this direction have not

yet been very successful.

APPENDIX I

DYNAMICS OF PHASE TRANSITION

When a long cylinder of type I superconductor is subjected to a longitudinal magnetic field swept at a constant rate electrodynamics can be used to describe the dynamics of the phase transition from the superconducting to the normal state. If we assume that a surface sheath of normal phase is formed initially, further flux panetration induces eddy currents in the sheath sufficient to maintain the field $H = H_c$ at the phase boundary between the superconducting and normal regions. The phase transition in a magnetic field is of first order and has a finite Latent heat associated with it. For the sake of simplicity, we shall ignore the latent heat absorbed during the S→N transition, and also the Joule heat produced by the eddy currents in the normal surface sheath.

Let us consider an infinitely long cylinder (length large compared to radius so that the demagnetisation coefficient is small) of radius a . Let $r=r_o$ mark the boundary between a superconducting core of radius r_o and the normal sheath.

The flux in the normal surface sheath is then

$$\Phi = \int_{r_o}^{a} 2\pi\, rH_c.dr$$

$$= \pi H_c (a^2 - r_o^2) \quad , \qquad \text{(A.1)}$$

assuming the field $H=H_c$ in the normal region.

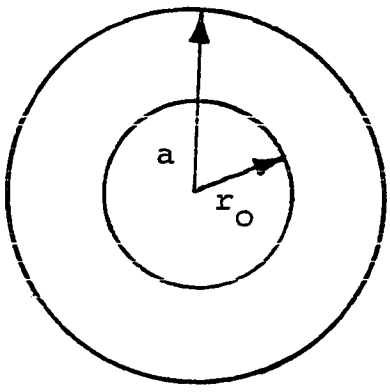

Maxwell's equations are

$$\nabla \times \vec{H} = \frac{4\pi}{C} \vec{J} \qquad (A.2)$$

$$\nabla \times \vec{E} = -\frac{1}{C} \frac{d\vec{B}}{dt} \qquad (A.3)$$

In cylindrical co-ordinates

$$\nabla \times \vec{H} = \left[\frac{1}{r} \frac{\partial H_z}{\partial \theta} - \frac{\partial H_\theta}{\partial Z} \right] \hat{r} + \left[\frac{\partial H_r}{\partial Z} - \frac{\partial H_z}{\partial r} \right] \hat{\theta} + \frac{1}{r} \left[\frac{\partial}{\partial r} (rH_\theta) - \frac{\partial H_r}{\partial \theta} \right] \hat{Z}$$

For a longitudinal external applied magnetic field and isotropic sample

$$H_r = H_\theta = 0 = \frac{dH}{dZ} = \frac{dH}{d\theta}$$

$$\therefore \quad H = H_z$$

$$\nabla \times \vec{H} = -\frac{dH}{dr} \hat{\theta}$$

using this in (A.2) above

$$\frac{d\vec{H}}{dr} = -\frac{4\pi}{C} \vec{J}$$

$$\frac{d\vec{H}}{dr} = -\frac{4\pi}{C} \sigma \vec{E} \qquad (A.4)$$

From (A.3)

$$\int (\nabla \times \vec{E}) dA = -\frac{1}{C} \int \frac{d\vec{B}}{dt} dA$$

$$= -\frac{1}{C} \frac{d}{dt} \int \vec{B} \, dA$$

$$= -\frac{1}{C} \frac{d\Phi}{dt}$$

Using Stoke's Theorem $\oint A \, dl = \iint_S (\nabla \times A) \, dS$

$$\therefore \quad \int \vec{E} . \, dS = - \frac{1}{C} \frac{d \Phi}{dt}$$

Or $$\frac{d \Phi}{dt} = - C \int \vec{E} . \, dS = - C . \, 2 \pi r \vec{E}$$

$$= - 2 \pi r C \vec{E}$$

$$\therefore \quad \vec{E} = - \frac{1}{2 \pi r C} \frac{d \Phi}{dt} \qquad (A.5)$$

Substituting for $\vec{E}$ in (A.4)

$$\frac{dH}{dr} = - \frac{4 \pi}{C} \sigma \left(- \frac{1}{2 \pi r C} \right) \frac{d \Phi}{dt}$$

$$= \frac{2 \sigma}{r C^2} \frac{d \Phi}{dt}$$

$$dH(r) = \frac{2 \sigma}{r C^2} \frac{d \Phi}{dt} \, dr \qquad (A.6)$$

$$\frac{dH}{dr} = \frac{2 \sigma}{r C^2} \frac{d \Phi}{dr_o} \frac{dr_o}{dt}$$

Substituting for Φ from (A.1)

$$\frac{dH}{dr} = \frac{2 \sigma}{r C^2} \frac{d}{dr_o} [\pi H_c (a^2 - r_o^2)] \frac{dr_o}{dt}$$

$$= \frac{2 \sigma}{r C^2} \pi H_c (- 2 r_o) \frac{dr_o}{dt}$$

$$= - \frac{4 \pi \sigma r_o}{r C^2} H_c \frac{dr_o}{dt}$$

$$dH(r) = - \frac{4 \pi \sigma H_c}{C^2} \frac{r_o}{r} \frac{dr_o}{dt} \, dr$$

$$H(r) = - \frac{4\pi\sigma H_c}{c^2} \int \frac{r_o}{r} \frac{dr_o}{dt} \, dr$$

$$= - \frac{4\pi\sigma H_c}{c^2} r_o \frac{dr_o}{dt} \ln r + \text{const.}$$

Boundary conditions

$$\left.\begin{array}{lll} \text{(i)} & H = H_c & \text{at } t=0 \\ \text{(ii)} & H = H_c + Pt & \text{at } r=a \\ \text{(iii)} & H = H_c & \text{at } r=r_o \end{array}\right) \quad \text{(A.7)}$$

$$\therefore \quad H(r) = H_c + Pt - \frac{4\pi\sigma H_c}{c^2} r_o \frac{dr_o}{dt} \ln \left(\frac{r}{a}\right) \qquad \text{(A.8)}$$

and $$H_c = - \frac{4\pi\sigma}{c^2} H_c r_o \frac{dr_o}{dt} \ln \left(\frac{r_o}{a}\right) + H_c + Pt$$

or $$Pt = \frac{4\pi\sigma}{c^2} H_c r_o \frac{dr_o}{dt} \ln \left(\frac{r_o}{a}\right) \qquad \text{(A.9)}$$

$$\int Pt \, dt = \frac{4\pi\sigma}{c^2} H_c \int r_o \ln \left(\frac{r_o}{a}\right) dr_o$$

or $$\frac{Pt^2}{2} = \frac{4\pi\sigma}{c^2} H_c \left[\frac{r_o^2}{2} \ln\left(\frac{r_o}{a}\right) - \frac{r_o^2}{4} \right] + \text{const.}$$

$$\frac{1}{2} Pt^2 = - \frac{4\pi\sigma}{c^2} H_c \frac{r_o^2}{4} \left[1 - 2 \ln \left(\frac{r_o}{a}\right) \right] + \text{const.}$$

Boundary conditions : At $t=0$ $\quad r_o=a$

$t=t_o$ $\quad r_o=0$

$$\frac{1}{2} Pt^2 = - \frac{4\pi\sigma}{c^2} H_c \frac{r_o^2}{4} \left[1 - \frac{a^2}{r_o^2} - 2 \ln \left(\frac{r_o}{a}\right) \right] \qquad \text{(A.10)}$$

$$\frac{1}{2} P t_o^2 = \frac{4\pi\sigma}{c^2} H_c \frac{a^2}{4}$$

$$t_o^2 = \frac{2\pi\sigma H_c}{P c^2} a^2 \qquad \text{(A.11)}$$

$$\Phi_I = \int_{r_o}^{a} H(r)\, 2\pi r\, dr \qquad (A.12)$$

$$= \int_{r_o}^{a} \left[H_c + Pt - \frac{4\pi\sigma}{c^2} H_c\, r_o \frac{dr_o}{dt} \ln\left(\frac{r}{a}\right) \right] 2\pi r\, dr$$

Using (A.9)

$$= \int_{r_o}^{a} \left[H_c + Pt\left(1 - \frac{\ln\left(\frac{r}{a}\right)}{\ln\left(\frac{r_o}{a}\right)}\right) \right] 2\pi r\, dr$$

$$= \left[(H_c + Pt)\, 2\pi \frac{r^2}{2} - \frac{2\pi Pt}{\ln\left(\frac{r_o}{a}\right)} \left(\frac{r^2}{2} \ln\left(\frac{r}{a}\right) - \frac{r^2}{4} \right) \right]_{r_o}^{a}$$

$$\Phi_I = \pi H_c a^2 \left[1 - \rho_o^2 + \frac{Pt}{2H_c \ln \rho_o} \left(1 - \rho_o^2 + 2 \ln \rho_o \right) \right]$$

$$\frac{d\Phi_I}{dt} = \pi H_c a^2 \left[-2\rho_o \frac{d\rho_o}{dt} + \frac{P(1-\rho_o^2)}{2H_c \ln \rho_o} - \frac{Pt(1-\rho_o^2)}{2\rho_o H_c (\ln \rho_o)^2} \frac{d\rho_o}{dt} \right.$$

$$\left. - \frac{Pt}{H_c \ln \rho_o \rho_o} \frac{d\rho_o}{dt} + \frac{P}{H_c} \right] \qquad (A.13)$$

where $\rho_o = \frac{r_o}{a}$

Eq. (A.13) can now be used to calculate the voltage induced in the pick up coil wound around the sample:

$$V = -\frac{N}{C} \frac{d\Phi_I}{dt} \qquad (A.14)$$

where N is the number of turns in the pick up coil.

To compute the induced voltage as a function of time we find ρ_o at various times t using (From (A.10) & (A.11))

$$t^2 = t_o^2 \left[1 - \rho_o^2 + 2 \rho_o^2 \ln \rho_o \right] \qquad (A.15)$$

Taking various values of ρ_o and calculating the corresponding times t. These can now be used to calculate

$\frac{d\rho_o}{dt}$ (from (A.9))

$$\frac{d\rho_o}{dt} = \frac{t}{t_o} \quad \frac{1}{2t_o \rho_o \ln \rho_o} \qquad \text{(A.16)}$$

and hence the induced voltage V (from A.13 and A.14)

$$V = -\frac{N\pi a^2}{C}\left[-2\rho_o \frac{d\rho_o}{dt}\left(H_c + \frac{Pt}{2\ln \rho_o}\right) + P\left(1 + \frac{1-\rho_o^2}{2\ln \rho_o}\left[1 - \frac{t}{\rho_o \ln \rho_o}\frac{d\rho_o}{dt}\right]\right)\right] \qquad \text{(A.17)}$$

Second Order Approximation

Substituting for $\frac{d\Phi}{dt}$ from (A.13) in (A.6)

$$dH(r) = \frac{2\pi\sigma H_c a^2}{C^2}\left[\frac{P}{H_c} + \frac{P(1-\rho_o^2)}{2H_c \ln \rho_o} - \left(2\rho_o + \frac{Pt(1-\rho_o^2)}{2\rho_o H_c (\ln\rho_o)^2} + \frac{Pt\rho_o}{H_c \ln\rho_o}\right)\frac{d\rho_o}{dt}\right]\frac{dr}{r}$$

$$H(r) = \frac{2\pi\sigma Pa^2}{C^2}\left[1 + \frac{1-\rho_o^2}{2\ln\rho_o} - \frac{H_c}{P}\left(2\rho_o + \frac{Pt(1-\rho_o^2)}{2\rho_o H_c (\ln\rho_o)^2} + \frac{Pt\rho_o}{H_c \ln\rho_o}\right)\frac{d\rho_o}{dt}\right]\ln r + \text{const.}$$

$$= \frac{2\pi\sigma Pa^2}{C^2}\left[1 + \frac{1-\rho_o^2}{2\ln\rho_o} - \left(\frac{2H_c\rho_o}{P} + \frac{t(1-\rho_o^2)}{2\rho_o(\ln\rho_o)^2} + \frac{t\rho_o}{\ln\rho_o}\right)\frac{d\rho_o}{dt}\right]\ln r + \text{const.}$$

Using the boundary conditions (A.7)

$$H(r)= H_c+ Pt+ \frac{2\pi\sigma\ Pa^2}{c^2}\Big[\ 1+\frac{1-\rho_o^2}{2\ln\rho_o} - \Big(\Big(\frac{2H_c\rho_o}{P} + \frac{t(1-\rho_o^2)}{2\rho_o(\ln\rho_o)^2} + \frac{t\rho_o}{\ln\rho_o}\Big)\frac{d\rho_o}{dt}\Big]\ln\Big(\frac{r}{a}\Big) \qquad (A.18)$$

$$Pt= -\frac{2\pi\sigma\ Pa^2}{c^2}\Big[1+\frac{1-\rho_o^2}{2\ln\rho_o} - \Big(\Big(\frac{2H_c\rho_o}{P} + \frac{t(1-\rho_o^2)}{2\rho_o(\ln\rho_o)^2} + \frac{t\rho_o}{\ln o_o}\Big)\frac{d\rho_o}{dt}\Big]\ln\Big(\frac{r_o}{a}\Big)$$

$$t = -\frac{\pi\sigma\ a^2}{c^2}\Big[1-\rho_o^2 + 2\ln\rho_o - \Big(\Big(2t\rho_o + \frac{t(1-\rho_o^2)}{\rho_o\ln\rho_o} + \frac{4H_c\rho_o\ln\rho_o}{P}\Big)\frac{d\rho_o}{dt}\Big]$$

$$(2\rho_o + \frac{1-\rho_o^2}{\rho_o\ln\rho_o})t\ \frac{d\rho_o}{dt} + \frac{4H_c\rho_o\ \ln\rho_o}{P}\ \frac{d\rho_o}{dt} - \frac{c^2\ t}{\pi\sigma\ a^2} - 1+\rho_o^2 - 2\ln\rho_o=0 \qquad (A.19)$$

$$\Phi_I = \int_{r_o}^{a} H(r)\ 2\pi r\ dr$$

$$= \int_{r_o}^{a}\Big[\ \frac{2\pi\sigma\ Pa^2}{c^2}\Big(\Big(1+\frac{1-\rho_o^2}{2\ln\rho_o} - \Big(\frac{2H_c\rho_o}{P} + \frac{t(1-\rho_o^2)}{2\rho_o(\ln\rho_o)^2} + \frac{t\rho_o}{\ln\rho_o}\Big)\frac{d\rho_o}{dt}\Big)\Big)$$

$$\ln\Big(\frac{r}{a}\Big) + Pt + H_c\ \Big]2\pi r\ dr$$

$$\Phi_I = \pi a^2 (H_c + Pt)(1 - \rho_o^2) + \frac{4\pi\sigma a^4}{c^2} \begin{pmatrix} \\ \cdots \\ \\ \end{pmatrix} \int_{r_o}^{a} r \ln\left(\frac{r}{a}\right) dr$$

$$= \pi a^2 (H_c + Pt)(1 - \rho_o^2) + \frac{\pi^2 \sigma Pa^4}{c^2} [1 - \rho_o^2 + 2\rho_o^2 \ln\rho_o] \begin{pmatrix} \\ .. \\ \\ \end{pmatrix}$$

$$= \pi a^2 (H_c + Pt)(1 - \rho_o^2) + \frac{\pi\sigma a^4}{c^2} [1 - \rho_o^4 \ln\rho_o + \frac{(1-\rho_o^2)}{2\ln\rho_o}$$

$$- \begin{pmatrix} \\ \left(\frac{2H_c\rho_o}{P} + \frac{t(1-\rho_o^2)}{2\rho_o(\ln\rho_o)^2} + \frac{t\rho_o}{\ln\rho_o}\right)(1 - \rho_o^2 + 2\rho_o \ln\rho_o)\frac{d\rho_o}{dt} \\ \\ \end{pmatrix}] \qquad (A.20)$$

$$V = -\frac{N}{C}\frac{d\Phi_I}{dt}$$

$$= -\frac{N\pi}{c^2} a^2 [-2\rho_o H_c \frac{d\rho_o}{dt} + P \begin{pmatrix} \\ (1 - \rho_o^2 - 2\rho_o P \\ \\ \end{pmatrix}$$

$$- \frac{\pi\sigma a^2}{c^2} \left([2\rho_o \begin{pmatrix} \\ (1 - \rho_o - 2\rho_o^2 + 2\ln\rho_o) \\ \\ \end{pmatrix} \right.$$

$$- \begin{pmatrix} \\ \left(1 + 3\rho_o + \frac{1-\rho_o^2}{\ln\rho_o}\right)\frac{1-\rho_o^2}{\ln\rho_o} + \begin{pmatrix} \\ (XY + W(1 - \rho_o + \ln\rho_o)) \\ \\ \end{pmatrix}\frac{d\rho_o}{dt} \\ \\ \end{pmatrix}$$

$$\left. \frac{d\rho_o}{dt} + WY \frac{d^2\rho_o}{dt^2} \right))] \qquad (A.21)$$

where

$$X = \frac{2H_c}{P} - \frac{(2 - \ln\rho_o)t}{(\ln\rho_o)^2} - \frac{(2 + \ln\rho_o)(1 - \rho_o^2)t}{2\rho_o^2 (\ln\rho_o)^3} \qquad (A.22)$$

$$W = \frac{2H_c \rho_o}{P} + \frac{(1-\rho_o^2)\, t}{2\rho_o (\ln \rho_o)^2} + \frac{\rho_o}{\ln \rho_o}\, t \qquad (A.23)$$

$$Y = 1 - \rho_o^2 + 2\rho_o \ln\rho_o \qquad (A.24)$$

$$H(r) = H_c + Pt + \frac{2\sigma}{c^2} \frac{d\Phi}{dt} \ln\left(\frac{r}{a}\right) \qquad (A.25)$$

Using the boundary conditions (A.7)

$$-\frac{P\, t\, c^2}{2\sigma \ln(\frac{r}{a})} = \frac{d\Phi}{dt}$$

$$\frac{d^2\rho_o}{dt^2} = \frac{1-\rho_o^2-\left(\frac{2\rho_o}{P}(H_c+Pt)+\frac{\pi\sigma a^2}{c^2}\left(2\rho_o\left(1-\rho_o-2\rho_o^2+2\ln\rho_o\right)\right.\right.}{\frac{\pi\sigma a^2}{c^2} W Y}$$

$$\left.\left.-\left(1+3\rho_o+\frac{1-\rho_o^2}{\rho_o\ln\rho_o}\right)\frac{1-\rho_o^2}{\ln\rho_o} + XY + W(1-\rho_o+\ln\rho_o)\right)\frac{d\rho_o}{dt}\right)$$

(A.27)

From (A.19)

$$\frac{d\rho_o}{dt} = \frac{1-\rho_o^2 + 2\ln\rho_o + \frac{c^2}{\pi\sigma a^2}\, t}{\left(2\rho_o + \frac{1-\rho_o^2}{\rho_o \ln\rho_o}\right) t + \frac{4H_c\rho_o\ln\rho_o}{P}} \qquad (A.28)$$

For the case when the magnetic field sweep is terminated at any time $t = t_1$ and the magnetic field is maintained at $H = H_1 = H_c + Pt_1$, then for $t \leq t_1$ the solution above holds.

For $t > t_1$, the new boundary conditions are

$$\left.\begin{aligned} P &= 0 && \\ H &= H_c + Pt_1 = H_1 && \text{at } r=a \\ H &= H_c && \text{at } r=r_o \end{aligned}\right\} \quad (A.29)$$

Proceeding as above

$$H(r) = H_c + Pt_1 - \frac{4\pi\sigma H_c}{c^2} r_o \frac{dr_o}{dt} \ln\left(\frac{r}{a}\right) \quad (A.30)$$

$$Pt_1 = \frac{4\pi\sigma H_c}{c^2} r_o \frac{dr_o}{dt} \ln\left(\frac{r_o}{a}\right) \quad (A.31)$$

$$Pt_1\, t = \frac{4\pi\sigma}{c^2} H_c \left[\frac{r_o^2}{2} \ln\left(\frac{r_o}{a}\right) - \frac{r_o^2}{4}\right] + \text{const.}$$

Let t_{o1} denote the new time of completion for the superconducting to normal transition i.e. $r_o = 0$ at $t = t_{o1}$

$$\therefore \quad t_{o1} = \frac{\pi\sigma a^2}{c^2 Pt_1} H_c \quad (A.32)$$

$$\Phi_I = \int_{r_o}^{a} H(r)\, 2\pi r\, dr$$

$$V = -\frac{N}{C} \frac{d\Phi_I}{dt}$$

$$V = \frac{N\pi a^2}{C}\left[\, 2\rho_o H_c + \frac{Pt_1}{2\rho_o(\ln\rho_o)^2}\left(1 - \rho_o^2(1-2\ln\rho_o)\right)\right]\frac{d\rho_o}{dt} \qquad (A.33)$$

where

$$\frac{d\rho_o}{dt} = \frac{P\,t_1}{\frac{2\pi\sigma a^2}{c^2}\rho_o \ln\rho_o\left[2H_c + \frac{P\,t_1}{(\rho_o\ln\rho_o)^2}\left(1-\rho_o^2 + \ln\rho_o(1+\rho_o^2)\right)\right]} \qquad (A.34)$$

Fig. A I shows the induced voltage as a function of time obtained using equation (A.21) along with the corresponding observed pulse. The agreement between the observed and the calculated pulses is reasonable in the part of the pulse following the peak.

Fig. A II shows pulses obtained at 0.502 K for various magnetic field sweep rates. As the magnetic field sweep rate increases, the initial rise becomes smoother, the slope $\frac{dV}{dt}$ increases, the peak is higher, and the transition time decreases.

Fig. A III shows the pulses obtained with a magnetic field sweep rate P=0.58 gauss/sec. at various temperatures. As the temperature T gets closer to the transition temperature T_c, the pulse rise becomes smoother and sharper i.e., $\frac{dV}{dt}$ increases. The peak height and total area under the pulse decreases and the transition time also decreases.

For the sake of discussion, it is convenient to divide the pulse shape into three regions: the initial peak, the

Fig. A I
Sample P4
H_c=50.71 G
$\dot{H}$ =0.58 G/Sec.
t_o=4.35 Sec.

INDUCED VOLTAGE

X

REDUCED TIME

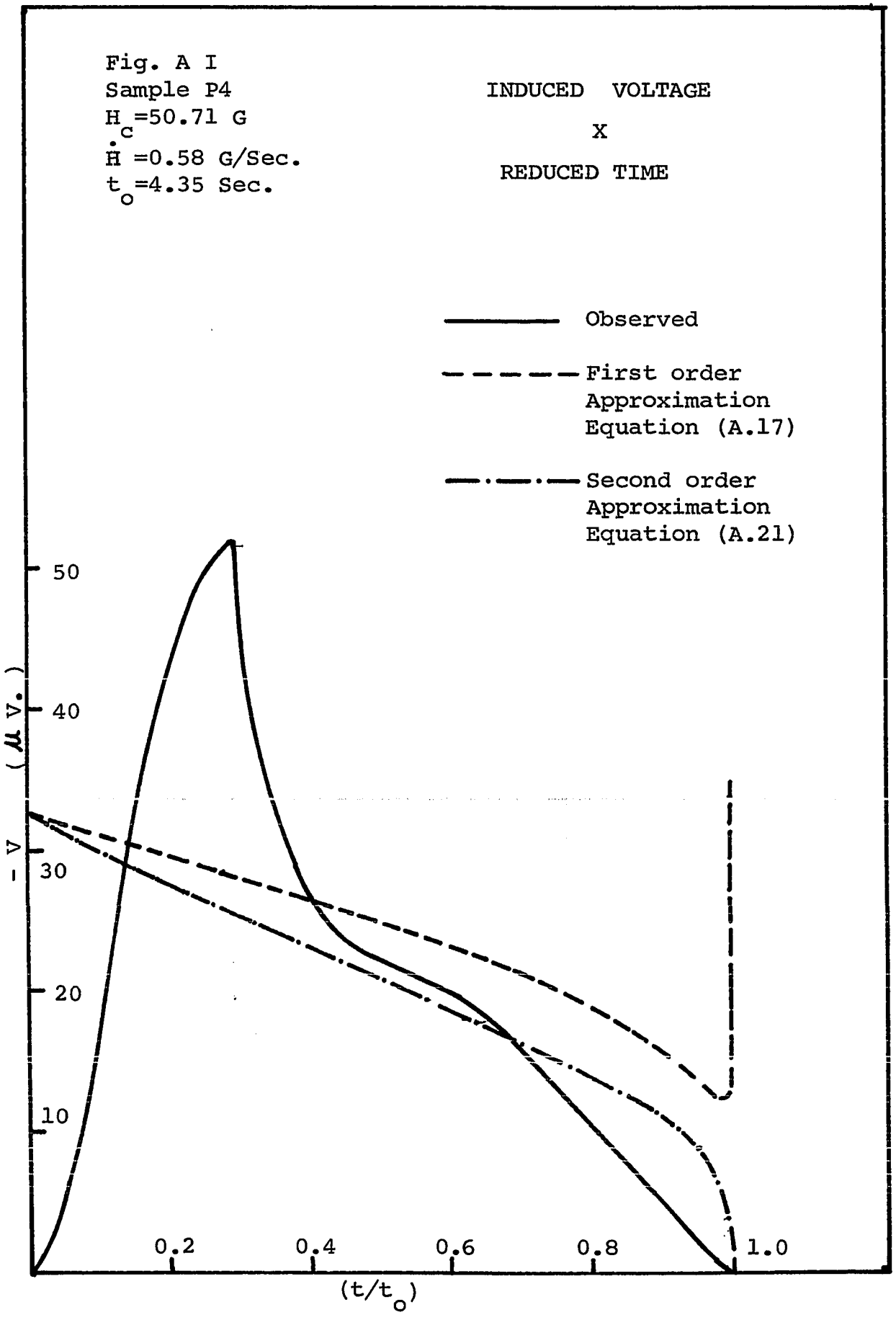

Fig. A II.a

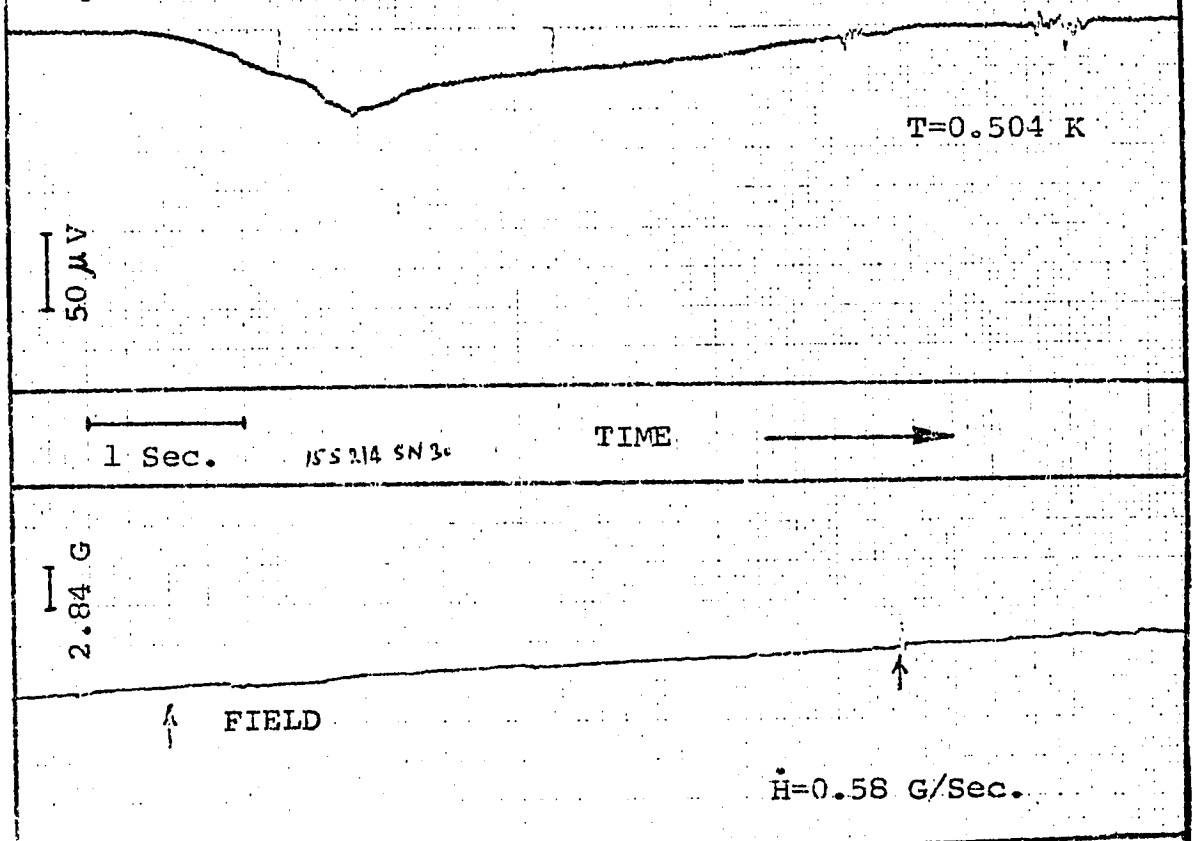

Fig. A II.b

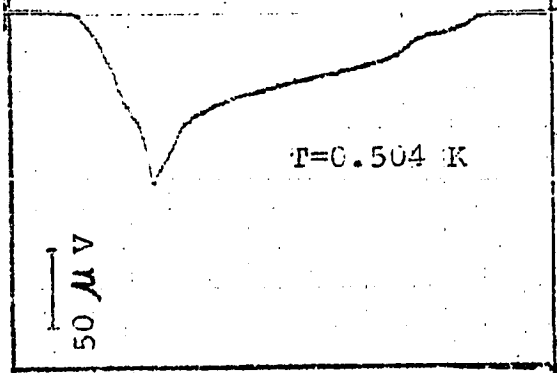

Fig. A II.c

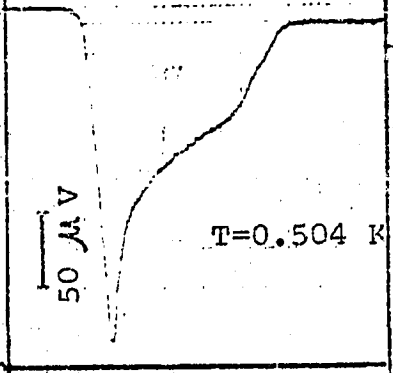

Fig. A II.d

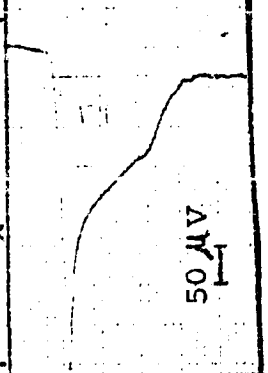

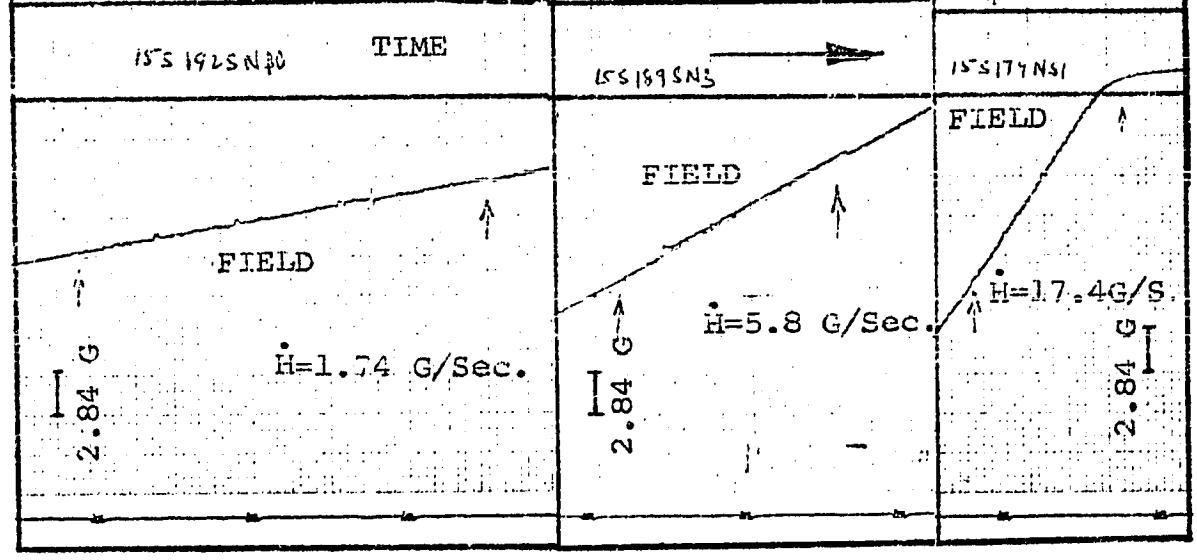

Fig. A III

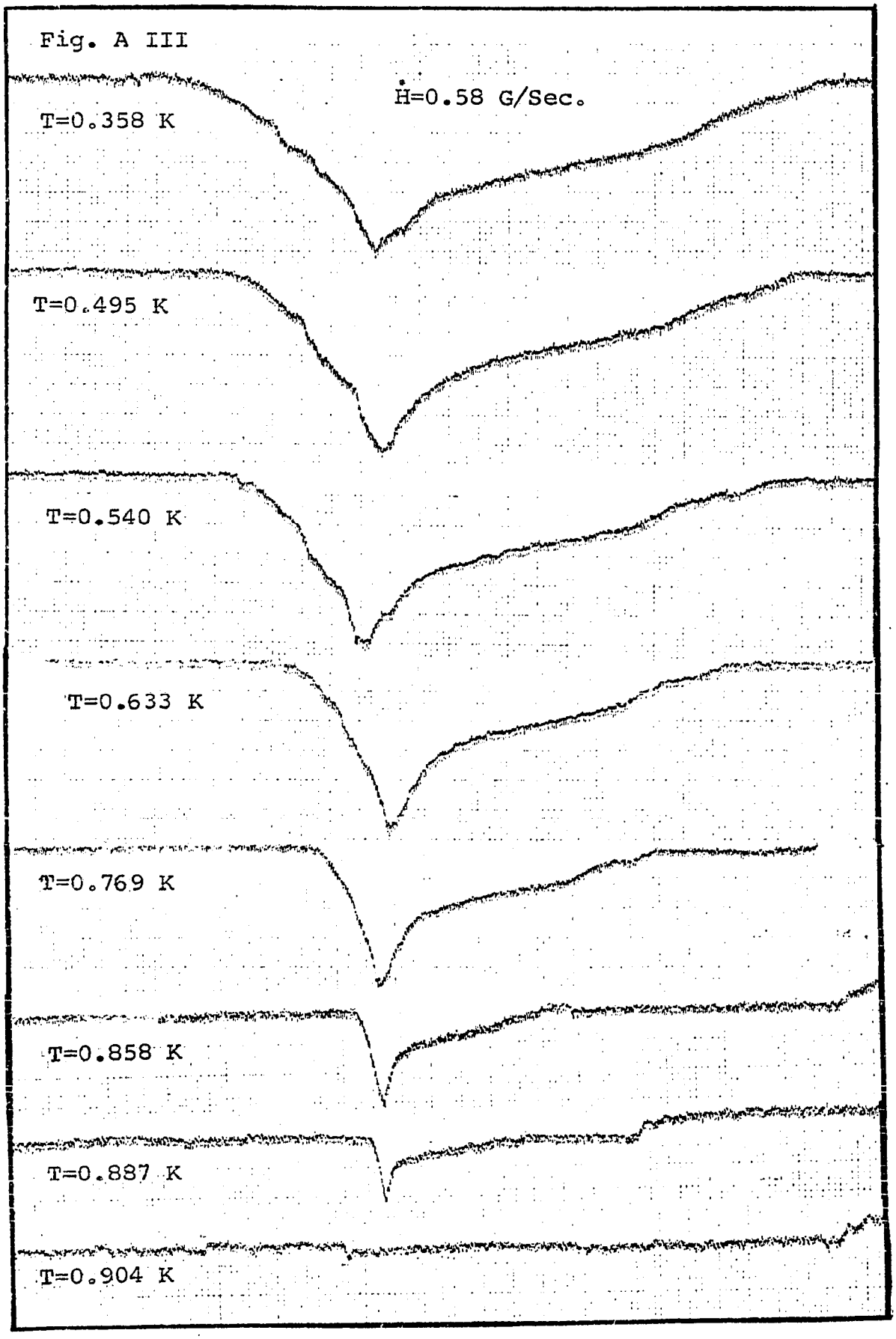
$\dot{H}$=0.58 G/Sec.
T=0.358 K
T=0.495 K
T=0.540 K
T=0.633 K
T=0.769 K
T=0.858 K
T=0.887 K
T=0.904 K

middle part and the tail. The region up to the initial peak is due to nucleation and subsequent growth of these nuclei into a normal sheath around the superconducting core. The middle part corresponds to the contraction of the superconducting core and is controlled by electrodynamic damping. The tail shape is determined mainly by defects in the sample.

Pinatti[22] studied the effect of annealing on the pulse shape. He observed significant changes in the initial peak and tail due to changes in defect structures (a more perfect surface and a reduced density of defects in the interior).

The dependence of pulse shape on magnetic field sweep rate was studied by Pinatti[22], and we have reproduced his measurements here.

As is clear from Fig. A II our assumption of a normal ring forming all at once at $H=H_c$ is not so bad for higher field sweep rates, but for lower magnetic field sweep rates the assumption is not valid. Since the experimentally observed pulse does not have an infinite peak at t=0, $H=H_c$, we are led to the conclusion reached by Faber[39-43], that the normal phase nucleates at $H=H_c$ and than grows into a ring around the sample. The slope $\frac{dV}{dt}$ of the initial peak will therefore be determined by the number of nuclei formed and their growth rate. The larger the concentration of nuclei and the larger their growth rate, the greater will be $\frac{dV}{dt}$, leading to a smoother, sharper pulse rise. Experimentally we have found $\frac{dV}{dt}$ is large for higher field sweep rates and temperatures close to the transition temperature. At higher field sweep rates, since the magnetic field gradients are larger, we would expect larger growth rates. As the temperature approaches the transition temperature the penetration depth

and the coherence length keep increasing and eventually become longer than the dimensions of the defect structures. For temperatures close to the transition temperature the defects are no longer the prefered sites for nucleation. The nucleation is closer to homogeneous. The number of nuclei formed is therefore considerably larger. As pointed out by Faber[75] the sample exhibits the ideal supercooling characteristic of the material close to the transition temperature.

The time at which the initial peak reaches its maximum value marks the completion of the formation of the normal surface sheath. What determines the height of the peak? The nuclei growth rate is proportional to the excess field $(H-H_c)$. This growth rate is so small that before equilibrium can be reached the magnetic field at the sample surface far exceeds the critical field. This effect is more pronounced when the field sweep rate is large. Thus the initial part of the pulse observed is essentially a nonequilibrium curve. The height of the peak is determined by the magnitude of the departure from equilibrium. It is a sort of superheating which results because the nuclei growth rate can not keep up with the increasing magnetic field. The larger the field sweep rate, the greater will be the departure from the equilibrium state, yielding a higher peak.

The middle region after the peak is determined by electrodynamic damping and is in reasonable agreement with theory.

The tail shape changes somewhat with field sweep rate but is independent of temperature. The slope $\frac{dV}{dt}$ at the end increases as the sweep rate increases. It changes also on annealing which lends support to the belief that it is determined by defects in the sample.

APPENDIX II

ROUGH ESTIMATE OF THE RESISTIVITY DUE TO DISSOLVED HYDROGEN

The resistance in a metal arises from the scattering of electrons. Electrons can be scattered by

(i) The thermal motion of the metal atoms

(ii) Lattice defects like vacancies, interstitials, dislocations etc.

(iii) Foreign atoms

At very low temperatures, below $\Theta_D/10$, electron-electron scattering dominates in the temperature dependent contribution to the resistivity. This gives rise to a resistivity ρ proportional to T^2.

The hydrogen atoms in molybdenum are ionised. The proton of the hydrogen atom must be accomodated in either tetrahedral or octahedral interstitial sites available in body centered cubic molybdenum lattice. This semilocalised proton can scatter conduction electrons. The proton is screened by the conduction electrons. The effective scattering potential due to the proton can be written as[76]

$$U = \frac{e^2}{r} \exp.(-qr) \qquad \text{(II.1)}$$

where $$q^2 = \frac{4 \pi n e^2}{k T_F} \qquad \text{(II.2)}$$

n = the density of electrons

k = Boltzmann's constant

and T_F = the Fermi temperature

The screening length is $1/q$.

The resistivity ρ of a metal is given by

$$\rho = \frac{m}{n e^2 \tau} \qquad \text{(II.3)}$$

where m = the free electron mass

e = the electronic charge

n = the electron density in the metal

and τ = the relaxation time

$$= 1/\overline{P} \qquad \text{(II.4)}$$

where $\overline{P}$ is the probablity per unit time that an electron suffers a collision.

Assuming perfectly free electrons, we can write the resistivity due to impurity scattering as[77]

$$\rho_I = \frac{m}{n e^2} \frac{A}{\Omega_o} v_F X \qquad \text{(II.5)}$$

where X = the proportion of foreign atoms in solution

v_F = the Fermi velocity

Ω_o = the volume per atom

and A = the effective scattering area presented by each atom,

$$A = \int_0^{\pi} (1-\cos\theta) \left| \frac{2\pi m}{h^2} \int \psi^*_{k'} U \psi_k \, d\tau \right|^2 2\pi \sin\theta \, d\theta \qquad \text{(II.6)}$$

The wave function of any state k can be written as

$$\psi_k = u_o(r) \exp.(ik.r) \qquad \text{(II.7)}$$

where $u_o(r)$ is the wave function for an electron in the lowest state in the solvent metal.

Assuming $U \ll \frac{1}{2} m v_F^2$, the problem can be solved by Born's approximation:

$$\int \psi^*_{k'} \frac{e^2}{r} \exp.(-qr)\, \psi_k \, d\tau$$

$$= \int e^{i(k-k').r} \frac{e^2}{r} \exp.(-qr)\, dr$$

$$= \frac{4\pi e^2}{|k-k'|^2 + q^2}$$

$$= \frac{4\pi e^2}{q^2} \qquad \text{for } k, k' \ll q^2$$

Substituting this in the expression for A above

$$\therefore\ A = \int_0^{\pi} (1-\cos\theta) \left| \frac{2\pi m}{h^2} \frac{4\pi e^2}{q^2} \right|^2 2\pi \sin\theta\, d\theta$$

$$= 4\pi \left(\frac{m k T_F}{2\pi n \hbar^2} \right)^2$$

Substituting the above and setting $\frac{1}{2} m v_F^2 = \frac{3}{2} k T_F$, equation (II.5) becomes:

$$\rho_I = \frac{m}{n e^2} \frac{v_F}{\Omega_o} 4\pi \left(\frac{2\pi m k T_F}{n h^2} \right)^2 X$$

For molybdenum we have[78] $v_F = 1.8.10^7$ cm./sec.

and $\Omega_o = \frac{4}{3}\pi R^3$, where R is the atomic radius of hydrogen. Using R=0.525 10^{-8} cm. (page 54) we get $\Omega_o = 6.\ 10^{-25}$ cm.^{3}.

Thus, $\rho_I = 0.0833\ 10^{-3}\ X$ Ohm. cm.

For 10 atomic ppm hydrogen in molybdenum

$$\rho_I = 0.0833\ 10^{-3} .\ 10^{-5} = 8.33\ 10^{-10} \text{ Ohm. cm.}$$

The observed contribution to the resistivity due to scattering by 9.6 atomic ppm of hydrogen atoms in molybdenum is approximately 5.0 10^{-10} ohm. cm.

Considering the assumptions made, the agreement seems to be fair.

ACKNOWLEDGMENTS

I am deeply indebted to Prof. H. E. Rorschach, Jr. for his guidance during the course of this research.

I wish to thank the faculty, students and staff of the Materials Science Department for their co-operation. In particular I must thank Prof. F. R. Brotzen for nlightening discourses on the mechanical properties of solids, Prof. J. M. Roberts for carrying out the tensile tests at room temperature and taking scanning electron micrographs at the Manned Spacecraft Centre, and Dr. G. Harkins for help with hydrogen analysis. Acknowledged also is the help provided by Dr. K. Salama during tensile testing at liquid nitrogen temperature. Hydrogen diffusion in the last two samples was carried out by Dr. Alan Oates.

I wish to express my appreciation to Prof. J. L. Margrave of the Chemistry Department for letting me use the RF Furnace and to Mr. David Bonnel for helpful suggestions.

Thanks are due to my fellow graduate students, in particular to Dr. D. O. Pederson for introducing me to the low temperature techniques, to Mr. Roland Schreiber for many interesting discussions and to Mr. Phil West for help in the early stages of hydrogen diffusion.

Financial support of Rice University, NSF and NASA through fellowship and research funds is gratefully acknowledged.

REFERENCES

1. F. N. Rhines, Trans. TMS AIME 156 , 335 (1944).
2. R. M. Barrer, Diffusion In And Through Solids, p.147. The Cambridge Series of Physical Chemistry. Cambridge, University Press (1941).
3. C. J. Smithells, Metals Refrence Book, p.570, Third Ed. Washington Butterworths (1962)
4. Y. Ebisuzaki and M. O'Keeffe, Prog. Solid State Chem. 72, 4695 (1968) ; 4, 187 (1967).
5. D. W. Jones, N. Pesall and A. D. Mc Quillan, Phil. Mag., 6, 455 (1961).
6. E. Dempsey, Phil. Mag. 8, 285 (1963).
7. R. Burch, Trans. Faraday Soc. 66, 736 (1970); 66, 749 (1970).
8. W. M. Baldwin, The Metal Molybdenum, p.279, ASM (1957).
9. C. F. Barth and E. A. Steigerwald, Met. Trans. 1, 1451 (1970).
10. D. P. Williams and H. G. Nelson, Met. Trans. 2, 1987 (1971).
11. C. Zapffe, Trans. ASM 39, 191 (1947).
12. A. S. Tetelman, Fundamental Aspects of Stress Corrosion Cracking, pp. 446-464. National Assoc. of Corrosion Engineers, Houston, 1969.
13. N. J. Petch, Phil. Mag. 1, 331 (1956).
14. D. P. Williams and H. G. Nelson, Met. Trans. 1, 63 (1970).
15. A. R. Troiano, Trans. ASM 52, 54 (1960).
16. P. Cotterill, Prog. Mat. Science 9,284 (1961).

17. D. W. Jones and A. D. Mc Quillan, J. Phys. Chem. Solids 23, 1441 (1962); D. W. Jones, Phil. Mag. 9, 709 (1964); K. A. Chao and G. S. Ansell, J. Appl. Phys. 41 417 (1970).

18. E. A. Lynton, B. Serin and M. Zucker, J. Phys. Chem. Solids 3, 165 (1957); G. Chanin, E. A. Lynton and B. Serin, Phys. Rev. 114, 719 (1959); Y. Ohtsuka, Y. Shibuya and T. Fukuroi, Sci. Rep. RITU, A15, 67 (1963).

19. D. P. Seraphim, D. T. Novick and J. I. Budnick, Acta. Met. 9, 446 (1961).

20. P. W. Anderson, J. Phys. Chem. Solids 11, 26 (1959).

21. W. De Sorbo, J. Phys. Chem. Solids 15, 7 (1960); Phys. Rev. 130, 2177 (1963).

22. D. G. Pinatti, Ph.D. Thesis, Rice University (1969).

23. S. Dushman, Scientific Foundations of Vaccum Technique, p. 519, John Wiley & Sons, Inc., New York (1962).

24. E. Martin, Arch. Eisenhuttenw. 3, 407 (1929/30).

25. A. Sieverts and K. Bruning, Arch. Eisenhuttenw. 7, 641 (1933/34).

26. S. Dushman, Scientific Foundations of Vaccum Technique, p. 537, John Wiley & Sons, Inc., New York (1962).

27. P. Cotterill, Prog. Mat. Science 9, 277 (1961).

28. C. J. Smithells and C. E. Ransley, Proc. Roy. Soc. A 150, 172 (1935).

29. R. Frauenfelder, J. Chem. Phys. 48, 3955 (1968).

30. M. L. Hill, J. Metals 12, 725 (1960).

31. W. A. Oates and R. B. McLellan, Personal Communication.

32. R. M. Barrer, Diffusion In And Through Solids, p.32. The Cambridge Series of Physical Chemistry. Cambridge, University press (1941).

33. F. J. Norton and A. L. Marshall, Trans. Am. Inst. Mining Met. Engrs. 156, 351 (1944); S. Dushman, Scientific Foundations of Vaccum Technique, p. 596. John Wiley & Sons, Inc., New York (1962).
34. R. G. Mallon, Ph.D. Thesis, Rice University (1966).
35. C. Blake and C. E. Chase, Rev. Sci. Instrum. 34, 984 (1963).
36. D. G. Pinatti, M.A. Thesis, Rice University (1968).
37. D. Cohen, Rev. De Physique Appliquee 5, 53 (1970).
38. D. Cohen, Appl. Phys. Letters 10, 67 (1967).
39. T. E. Faber, Proc. Roy. Soc. A214, 392 (1952a). (Part I).
40. T. E. Faber, Proc. Roy. Soc. A219, 75 (1953) (Part II).
41. T. E. Faber, Proc. Roy. Soc. A223, 174 (1954) (Part III).
42. T. E. Faber, Proc. Roy. Soc. B231, 353 (1955) (Part IV).
43. T. E. Faber and A. B. Pippard, Progress in Low Temperature Physics, vol. 1, 1955. North Holland Publishing Co., Amsterdam. Ed. C. J. Gorter.
44. A. B. Pippard, Phil. Mag. 41, 243 (1950a).
45. F. Heiniger, E. Bucher and J. Muller, Phys. Kondens. Materie. 5, 243 (1966).
46. B. T. Mathias, T. H. Geballe, E. Corenzwit and G. W. Hull, Jr., Phys. Rev. 129, 1025 (1963).
47. J. Bardeen, L. Cooper and J. R. Schrieffer, Phys. Rev. 108, 1175 (1957).
48. P. W. Anderson, J. Phys. Chem. Solids 11, 26 (1959); J. D. Livingston and H. W. Schadler, Progress in Materials Science 12, 3 (1964).
49. D. Markowitz and L. P. Kadanoff, Phys. Rev. 131, 563 (1963).

50. D. M. Ginsberg, Phys. Rev. 136, A1167 (1964); Phys. Rev. 138, A1409 (1965).

51. J. R. Clem, Phys. Rev. 153, 449 (1967).

52. F. V. Burckbuchler, D. Markowitz and C. A. Reynolds, Phys. Rev. 175, 543 (1968).

53. D. U. Gubser, D. E. Mapother and D. L. Connelly, Phys. Rev. B 2, 2547 (1970).

54. N. L. Muench, Phys. Rev. 99, 1814 (1955).

55. B. B. Goodman, Comptes. rendus. 28, 3031 (1958).

56. D. Saint-James and P. G. De Gennes, Phys. Letters 7, 306 (1963).

57. P. G. De Gennes, Superconductivity of Metals and Alloys, Translated by P. A. Pincus, W. A. Benjamin, Inc., New York, 1966.

58. J. E. Ostenson and D. K. Finnemore, Phys. Rev. Letters 22, 188 (1969).

59. G. Ebneth and L. Tewordt, Z. Physik 185, 421 (1965).

60. G. Luders, Z. Physik 202, 8 (1967); G. Luders and K. D. Usadel, Z. Physik 222, 355 (1969); K. D. Usadel and M. Schmidt, Z. Physik 221, 135 (1969).

61. C. R. Hu and V. Korenman, Phys. Rev. 178, 684 (1969); Phys. Rev. 185, 672 (1969); C. R. Hu, Phys. Rev. 187, 574 (1969).

62. M. D. Maloney, F. de la Cruz and M. Cardona, Phys. Rev. B, 2, 2512 (1970).

63. B. B. Goodman, Phys. Letters 1, 215 (1962).

64. L. P. Gorkov, J. Exptl. Theoret. Phys. (U. S. S. R.), 37, 1407 (1959); Sov. Phys. JETP, 10, 998 (1960).

65. C. Caroli, P. G. De Gennes and J. Matricon, Phys. Kondens. Mater. 1, 176 (1963).

66. A. M. Toxen, Phys. Rev. 133, A1218 (1964).

67. B. B. Goodman, IBM J. Res. Dev. 6, 63 (1962).

68. W. Hume-Rothery and G. V. Raynor, The Structure of Metals and Alloys, Inst. Metals, 1954, pp. 216-218.

69. G. B. Gibbs, Phys. Stat. Sol. 10, 507 (1965).

70. R. I. Galey, Jr., E. A. Lynton and B. Serin, Phys. Rev. 126, 43 (1962).

71. A. B. Pippard, J. Phys. Chem. Solids 3, 175 (1957); Phil. Mag. 46, 1104 (1955).

72. J. W. Garland, Jr., Phys. Rev. Letters 11, 111 (1963). In the notation of Garland $V_p/V_c = K_{ph}/K_c^* = -1-$ $^{-1/2}$.

73. E. Fawcett, Phys. Rev. 128, 154 (1962).

74. J. L. Youngblood, Ph.D. Thesis, Rice University (1963).

75. T. E. Faber, Proc. Roy. Soc. A241, 531 (1957); Proc. Roy. Soc. A248, 460 (1958).

76. J. M. Ziman, Electrons and Phonons, Oxford University Press, 1960, p. 170.

77. N. F. Motts and H. Jones, The Theory of the Properties of Metals and Alloys, Oxford University Press, 1936, p. 263.

78. R. A. French, Phys. Stat. Sol. 21, K35 (1967).